

Resonant Switch Receivers

Qitong Jin

Electrical Engineering and Computer Sciences
University of California, Berkeley

Technical Report No. UCB/EECS-2025-47

<http://www2.eecs.berkeley.edu/Pubs/TechRpts/2025/EECS-2025-47.html>

May 12, 2025



Copyright © 2025, by the author(s).
All rights reserved.

Permission to make digital or hard copies of all or part of this work for personal or classroom use is granted without fee provided that copies are not made or distributed for profit or commercial advantage and that copies bear this notice and the full citation on the first page. To copy otherwise, to republish, to post on servers or to redistribute to lists, requires prior specific permission.

Resonant Switch Receivers

By

Qitong Jin

A dissertation submitted in partial satisfaction of the
requirements for the degree of

Doctor of Philosophy

In

Engineering — Electrical Engineering and Computer Sciences

in the

Graduate Division

of the

University of California, Berkeley

Committee in charge:

Professor Clark Nguyen, Chair

Professor Liwei Lin

Professor Ming-Chiang Wu

Spring 2025

Abstract

Resonant Switch Receivers

by

Qitong Jin

Doctor of Philosophy in Engineering — Electrical Engineering and Computer Sciences

University of California, Berkeley

Professor Clark Nguyen, Chair

This thesis presents the design, fabrication, testing, and performance analysis of micromechanical resonant switches, or "resoswitches," as an innovative alternative to traditional transistor-based components in ultra-low-power wireless communication systems. By harnessing mechanical resonance, resoswitches introduce a novel paradigm for energy-efficient receivers with promising applications in remote sensing, RFID, environmental monitoring, and other domains where power conservation is crucial. Unlike conventional electronic components, resoswitches consume no standby power, allowing for continuous "listening" without the power-intensive sleep-wake cycling typically required in traditional receivers.

A central contribution of this work is the development of a bit rate-adapting resoswitch, capable of adjusting to varying input bit rates by utilizing stored resonant energy, which enhances its adaptability in low-power communication channels. By leveraging resonance energy during non-driven intervals, the resoswitch efficiently supports a broader range of data rates, demonstrating stable communication up to 8 kbit/s, even under limited power and bandwidth conditions. This adaptability unveils the potential of resoswitches for reliable communication in energy-sensitive applications.

Another major focus is the integration of ferrite-rod antennas to drive wireless communication in resoswitch-based receivers, addressing key challenges such as impedance matching, frequency tuning, and bandwidth limitations of antenna-receiver systems. Experimental results confirm the feasibility of resoswitches in achieving low-bit-rate wireless data reception despite high impedance mismatches and frequency constraints, enabling successful signal demodulation over short ranges.

Additionally, this work introduces a push-pull resoswitch communication receiver, which enhances bit rate adaptability and eliminates frequency instability to improve data transmission reliability in low-power communication environments.

The findings of this research underscore both the advantages and current limitations of resoswitch technology when compared to high-speed electronic components. While current resoswitches cannot yet achieve the high data rates typical of transistor-based devices, their energy efficiency and passive operation offer significant benefits in applications where power savings are paramount. This work establishes a foundational understanding of resoswitch performance, paving the way for further advancements in areas like antenna optimization, impedance matching, and innovative resoswitch designs optimized for robust, long-range, and scalable wireless applications in energy-constrained environments.

Dedicated to my parents and my cat, Baobao Jin.

Table of Contents

Contents	ii
List of Figures	iv
List of Tables	xii
Chapter 1 Introduction	1
1.1 Wireless Receiver Front-End	2
1.2 Review of Resoswitches & Previous Work	6
1.3 Dissertation Overview	10
Chapter 2 Design and Fabrication of Resoswitches	11
2.1 Comb-Driven Resoswitch Structure and Operation	11
2.1.1 Resoswitch Versus Conventional MEMS Switch	
2.1.2 Practical Receiver Operation	
2.2 Micromechanical Resoswitch Designs	15
2.2.1 Design Process	
2.2.2 Example Resoswitch Receiver Designs	
2.3 Gold-Electroplated Comb-Driven Resoswitches	25
2.3.1 Fabrication Process: Electroplating Mold	
2.3.2 Fabrication Process: Gold Electroplating	
2.3.3 Experimental Results	
2.4 Ruthenium-Electroplated Comb-Driven Resoswitches	38
2.4.1 Fabrication Process: Ru Electroplating	
2.4.2 Fabrication Process: Electroplating Mold	
Chapter 3 Bit Rate-Adapting Resoswitches	42
3.1 Device Structure and Operation	44
3.2 Time to Impact and Maximum Bit Rate	45
3.2.1 Bit Rate and Sensitivity Tradeoff	
3.2.2 Pre-energizing Theory	
3.2.3 Maximum Bit Rate	
3.2.4 What About Long Trains of 0's	
3.3 Fabrication Process	51
3.4 Experimental Results	52
3.5 Conclusion	55
Chapter 4 Ferrite-Rod Antenna Driven Wireless Resoswitch Receiver	57
4.1 Introduction	57

4.2	Device Structure and Operation	58
4.3	Antenna Resoswitch Co-Design	60
	4.3.1 Ferrite-Rod Antenna	
	4.3.2 Impedance Matching	
4.4	Experimental Results	62
4.5	Conclusion	66
Chapter 5 Push-Pull Resoswitch Communication Receiver		68
5.1	Resoswitch Impact Dynamics – Squegging	70
5.2	Push-Pull Receiver Structure and Operation	74
5.3	Experimental Results	77
5.4	Challenges Encountered During Measurements	80
5.5	Conclusion	81
Chapter 6 Conclusions		83
6.1	Future Research Directions	84
6.2	Possible New Design: Ru CC Beam Resoswitch	85
6.3	Concluding Remarks	90
Bibliography		92
Appendix A: Gold-Electroplated Resoswitch Process Traveler		97
Appendix B: Ruthenium-Electroplated Resoswitch Process Traveler		104

List of Figures

Fig. 1.1: (a) A schematic overview of a conventional receiver front end, highlighting the critical role of the low noise amplifier (LNA) in ensuring proper functionality. (b) The spectrum input to the LNA in a conventional receiver front end after the band-select filter, showing nearby interferers that can overshadow the desired signal after amplification by the LNA. (c) The spectrum input to the LNA after a channel-select filter, where interferers are significantly attenuated, reducing the likelihood of spurious signals. (d) An ideal receiver front end concept achievable through the use of a resoswitch.2

Fig. 1.2: (a) Schematic of a CMOS inverter amplifier. (b) The I - V curve of the inverter amplifier illustrates that maximum linearity (Point A) corresponds to the highest power consumption. To reduce power consumption, Point B is preferred, but it results in minimal linear gain, which is undesirable. (c) The issue can be resolved if an amplifier with infinite gain is realized.....3

Fig. 1.3: (a) Input FSK waveform applied to a conventional LNA. (b) Expected output waveform, where the output toggles between low and high voltages in response to the valid input sinusoidal wave crests at the amplifier's operating frequency (f_0). When the input signal falls outside the amplifier's working frequency range, the output remains zero.....4

Fig. 1.4: (a) Schematic of a comparator-diode-capacitor circuit capable of demodulating an OOK (ASK-modulated) input signal to reproduce the input bitstream at the output load under ideal component conditions. (b) By incorporating a channel select filter, the circuit can also demodulate an FSK-modulated input signal, restoring the input bitstream at the output load (d).....4

Fig. 1.5: (a) SEM of the polysilicon resoswitch demonstration vehicle used in [10], which comprises a wine-glass disk resonator with properly spaced and positioned input/ output electrodes; and (b) zoom-in view of the electrode-to-resonator gap of the device along the switch axis.....7

Fig. 1.6: SEM of a 25-MHz wine-glass mode electroplated-nickel disk resonant switch, with a zoom in view of an anchor and the electrode-to-disk gap [13]8

Fig. 1.7: Very-Low-Frequency (VLF) and Low-Frequency (LF) communication systems enable long-distance and cross-continent signal transmission.....9

Fig. 1.8: SEM of an electroplated gold comb-drive based resoswitch in [11]9

Fig. 2.1: Mechanical implementation of a receiver front end (a) utilizing a resoswitch receiver (b). For FSK-modulated input signals (c) and (d), the movable shuttle of the resoswitch

displaces and impacts the output electrodes (e), reproducing the input bitstream at the output (f). Similarly, the resoswitch receiver can process ASK-modulated input signals (g) and (h), yielding the corresponding output bitstream (j), with analogous shuttle displacements illustrated in (i).12

Fig. 2.2: Schematic of a low-frequency comb-driven resoswitch receiver.14

Fig. 2.3: Equivalent circuits of (a) the resoswitch receiver when it processes (b) an input “1” (charging the output load R_L and C_L) and (c) an input “0” (discharging the load)18

Fig. 2.4: Input power drives the resoswitch shuttle to move laterally, overcoming the gap spacing g_{switch} , making contact with the output electrode to transmit signals. The sensitivity threshold represents the minimum input power required to achieve this impact.....19

Fig. 2.5: Frequency mask of the device in design C (Table II) with V_P 25V.....23

Fig. 2.6: Process flow of electroplated gold resoswitch using oxide mold.....28

Fig. 2.7: SEM image showing that the Al_2O_3 protective layer and the gold seed layer, which is critical for future electroplating, have been completely etched away in large open areas during the oxide mold etching process. This issue must be resolved to successfully fabricate functional electroplated devices.....28

Fig. 2.8: (a) Larger features are etched at a faster rate than smaller ones. Prolonged oxide mold etching can remove both the protective layer and the gold seed layer in large features, resulting in non-electroplatable areas. (b) Shortening the oxide mold etch time helps preserve the seed layer in large open areas but may leave oxide residue in smaller features, preventing electroplating in subsequent steps.....29

Fig. 2.9: A similar issue arises with the a-Si mold, where the etch rate is higher in large open areas. This results in the removal of the protective layer and the underlying seed layer, leading to unintended non-electroplated regions.....29

Fig. 2.10: Poor adhesion between the SiO_2 protective layer, gold seed layer, and the substrate results in the delamination of the a-Si mold from the substrate, rendering it unsuitable for the subsequent electroplating step.....30

Fig. 2.11: The deposited a-Si film appears blurry and contains debris-like inclusions, highlighting cleanliness issues with the a-Si mold that need to be addressed.....30

Fig. 2.12: Process flow of the gold electroplated resoswitch with photoresist mold.....31

Fig. 2.13: SEM image of the interdigitated comb fingers of a resoswitch, demonstrating that the PR mold successfully achieves a finger spacing of $1\ \mu m$31

- Fig. 2.14: SEM and optical microscope images showing the fully fabricated resoswitch devices.....32
- Fig. 2.15: All fixtures are custom-designed and fabricated from Teflon. The setup enables precise control of electroplating parameters, including the spacing between the cathode and anode, the depth of the sample in the plating solution, plating uniformity across samples or wafers, and other critical factors.33
- Fig. 2.16: Electroplating results using the PR mold under varying temperature and current conditions.34
- Fig. 2.17: Experimental setup of the resoswitch receiver.....35
- Fig. 2.18: (a) Mixing measurement setup and applied bias and local oscillator voltages to null parasitic feedthrough en route to obtaining the (b) transmission spectrum of the gold resoswitch, showing a resonance frequency of 23.7 kHz and a Q of 502.....36
- Fig. 2.19: (a) Measured output signal and its corresponding waveform after processing through a comparator circuit, with the threshold set to half of the maximum output signal, for an ASK-modulated input bit stream. (b) Measured output signal and its corresponding waveform after processing through a comparator circuit, with the threshold set to half of the maximum output signal, for an FSK-modulated input bit stream.....36
- Fig. 2.20: Measured output signals for (a) ASK-modulated input signals and (b) FSK-modulated input signals. In both cases, frequency instability caused by the phenomenon known as 'squegging' was observed, leading to bit errors in the output. This instability highlights the challenges in maintaining consistent signal integrity during demodulation, particularly when operating under certain input conditions or device configurations.....37
- Fig. 2.21: Process flow of Ru-electroplated resoswitch with PR mold.....40
- Fig. 2.22: Optical microscopic images showing electroplated Ru structures develop cracks when the thickness exceeds 250 nm.....40
- Fig. 2.23: Process flow of Ru-electroplated Resoswitch with oxide mold.....41
- Fig. 3.1: All-mechanical communication receiver employing (a) an all-gold micromechanical resoswitch to accept at its (b) input a (c) ASK-modulated resonance carrier with marks and spaces. The resoswitch responds to mark periods, i.e., when the resonance sinusoid appears, by vibrating at resonance to impact its (d) shuttle impactor against (e) a conductive cantilever output electrode, connecting the cantilever to V_{DD} , hence charging the (f) output load capacitance C_L to V_{DD} and registering an output high or '1'. When receiving a space input, i.e., no sinusoid, the resoswitch does not move, allowing (g) bleed resistor R_L to discharge the load

to an output low, or '0'. In the end, the output bit stream matches the input modulating bit stream, meaning that the bits have been successfully communicated.....43

Fig. 3.2: Microscope photograph of a fabricated resoswitch with labels to identify important parts. This resoswitch features gold cantilever electrodes designed to soften impacts to reduce squegging, which occurs when hard impacts de-phase a resoswitch in a way that temporarily lowers the efficiency of the drive input, causing the device to lose amplitude and stop impacting until a return to proper phasing reinstates the drive, allowing impacting once again.....44

Fig. 3.3: Equivalent mass-spring-damper second order system of resoswitch. m_r , k_r and c_r represent the dynamic mass, stiffness, and mechanical damping of resoswitch.....45

Fig. 3.4: (a) Long period ASK excitation of a resoswitch with long space periods allows the resoswitch to come to rest on each cycle, forcing it to traverse the full gap distance in order to impact again, greatly slowing the time to impact, i.e., the switching time t_{slow} . (b) Shorter period ASK marks (that realize a faster bit rate) do not allow the resoswitch to come to rest, allowing it to retain energy than then permits much faster rise times from the next mark input to impact, and thus much faster switching times t_{fast} to support the faster bit rate. Here, the long first ASK mark input is required to pre-energize the resoswitch before accepting the fast data rate.....47

Fig. 3.5: Equivalent circuit of resoswitch when impact happens. R_{on} is the contact resistance between shuttle and output electrode, R_L is the load resistance, C_L is the load capacitance and V_{DD} is the applied DC voltage on the shuttle. C_L will be charged up through R_{on} and discharge through R_L49

Fig. 3.6: Measured maximum bit rate vs. driving power.....49

Fig. 3.7: Manchester encoding divides a bit into two halves with the transition happens at the middle of the bit. It provides synchronization and avoids the condition of long train of 0's.....50

Fig. 3.8: Process flow of electroplated gold resoswitch.....51

Fig. 3.9: (a) Mixing measurement setup and applied bias and local oscillator voltages to null parasitic feedthrough en route to obtaining the (b) transmission spectrum of the gold resoswitch, showing a resonance frequency of 23.7 kHz and a Q of 502.....52

Fig. 3.10: Measured oscilloscope waveforms showing the modulation waveform, ASK input signal, and resoswitch responses for three bit-period cases: (a) 1 kbps, (b) 2 kbps, (c) 4 kbps, and (d) 8 kbps.....53

Fig. 3.11: (a) Switching time vs. pre-energizing time T (cf. Fig. 10) at different modulation factors. Here, switching time decreases with higher pre-energizing amplitudes and longer pre-energizing times. (b) Switching time vs. modulation factor (V_M in Fig. 10) for a 50% duty-cycle square wave input with $T=20$ ms. Increasing the modulation factor decreases the switching time, since it increases the initial displacement amplitude upon an input rise.....54

Fig. 3.12: Switch time with and without pre-energization. The first bit with amplitude V_i has no pre-energization and shows a long switch time. Between the first and second bit is a pre-energizing period where the input amplitude is reduced to V_M for time T . The switch time for the second bit is subsequently faster.....54

Fig. 4.1: Wireless communication demonstration set-up employing (a) ferrite-rod antennas and (b) an all-mechanical resoswitch to receive and demodulate the (d) OOK-modulated data bit stream of (c) into the matching resoswitch output bit stream of (e).....59

Fig. 4.2: Z parameter magnitude, derived from measured S parameters, of the ferrite-rod antenna before and after tuning.....61

Fig. 4.3: SEM micrograph of the single-mask electroplated-gold resoswitch fabricated for this work.....63

Fig. 4.4: Measured power delivered to the resoswitch vs. antenna separation distance falls off with an inverse square law.....64

Fig. 4.5: Transmitted (orange) and antenna received (blue) waveforms (decimated to show sinusoids) for the cases of slow and fast bit rates.....64

Fig. 4.6: Measured waveforms showing successful wireless demodulation using the antenna-fed resoswitch receiver.65

Fig. 4.7: Measured comparison of received waveforms (orange) and resoswitch outputs (green) at 1 kbit/sec connected directly (top) and wirelessly using an antenna (bottom).....65

Fig. 4.8: Measured ferrite-rod antenna-driven resoswitch receiver sensitivity vs. transmit bit rate.....66

Fig. 5.1: SEM of a gold resoswitch identifying important features. Upon application of a dc-biased sinusoid at the device resonance frequency to the input comb-finger electrode, the movable suspended shuttle vibrates to impact the output electrode, periodically closing the shuttle-to-output switch.....69

Fig. 5.2: Illustrations depicting one mechanism behind squegging. Here, a continuous wave input at resonance frequency f_0 drives the resoswitch device (a). Ideally, the resoswitch shuttle

would impact the output electrode periodically (b) and maintain the 90° phase-shift between displacement and input force needed for efficient drive, generating the output waveform in (c). Unfortunately, impacts introduce phase shifts that pull the displacement and force away from 90° (d), reducing the drive efficiency and causing missed impacts until the phase recovers to restore drive efficiency and induce impacting once again. Less frequent impacts lead to an output waveform with much deeper sawtooths, as depicted in (e) and the measured waveform of (f).....71

Fig. 5.3: Measured results comparing the performance of resoswitches with soft contact output electrodes (a) and hard contact output electrodes (b). When given an ASK-modulated input signal, the output electrode with higher stiffness exhibits greater frequency instability due to squegging, compared to the soft contact electrode.....73

Fig. 5.4: Measurement of frequency instability in resoswitches with varying contact stiffness (*cf.* Fig. 5.3). (a) An input bit stream with ASK-modulated signals at a 1 ms period is applied to the resoswitch, and the corresponding output signal periods are measured. The standard deviation of these periods is then calculated over N input bits. (b) The standard deviation of the output period is plotted as a function of contact stiffness. In the absence of squegging-induced frequency instability, the standard deviation would ideally be zero.....74

Fig. 5.5: Illustrative summary of a push-pull all-mechanical zero quiescent power FSK receiver. Here, the (a) input bit stream is (b) FSK-modulated into an off-resonance signal to represent a ‘0’ or an on-resonance signal to denote a ‘1’. Reception of a ‘1’ at the input electrode induces resonance vibration of the top structure, in turn instigating impacting of the shuttle to the output electrode at (c). Impacting then periodically transfers charge from V_{DD} to the output load capacitor (d) C_L , eventually charging it to V_{DD} , which corresponds to a ‘1’. Any ‘0’ input received afterwards stops resonant impacting of the top resonator and instigates it in the bottom one, which impacts to connect the output node to ground, allowing C_L to discharge to ground, denoting a ‘0’. In this way, the input bit stream is faithfully reproduced at the output, as shown in (e).....75

Fig. 5.6: Equivalent circuits of a single resoswitch receiver. (a) When the resoswitch shuttle makes contact with the output electrodes at input "1." (b) When the resoswitch does not make contact, causing the charge on C_L to dissipate through the bleed resistor.....76

Fig. 5.7: Illustrative summary of a low-frequency all-mechanical zero quiescent power OOK receiver. Here, the (a) input bit stream comprises a (b) OOK-modulated on-resonance carrier signal that drives the device into resonance vibration, instigating shuttle-to-electrode impacts during “on” periods that then charge (c) C_L to deliver a (d) output high. During “off” periods, the resoswitch does not move, so does not impact the output, allowing bleed resistor R_{bleed} to discharge C_L to 0V (i.e., output low). Constant current bleed by R_{bleed} becomes problematic from both stability and processing power consumption perspectives.....76

Fig. 5.8: One-mask gold resoswitch fabrication process.....78

Fig. 5.9: Measured OOK input, C_L output, and comparator output waveforms for the single-device circuit of Fig. 3 followed by a comparator (amplifier), as in [*]. (V_{CL} is the voltage across C_L , while V_{CLK} is the output of the comparator.) Here, squegging induces a deep drop in V_{CL} around 3 ms that then causes the comparator output V_{CLK} to switch in error.....79

Fig. 5.10: Measured FSK input and practically perfect output (despite possible squegging) of the push-pull resoswitch receiver of Fig. 3. No comparator is needed here to achieve the “brick wall” output waveform.....79

Fig. 5.11: Illustration of the simultaneous activation ("both ON" condition) in a push-pull resoswitch receiver. (a) Resonance frequencies of the top and bottom resoswitches used in the measurements. (b) Measured output waveforms with an FSK-modulated input signal, showing distinct "spikes" in the output. These spikes result from both resoswitches activating simultaneously—where the top resoswitch charges the output electrode to V_{DD} while the bottom resoswitch discharges it within the same cycle.....80

Fig. 5.12: Illustration of the Duffing effect in resoswitch receivers. As the input power increases, the resonance peak broadens, resulting in an expanded passband.....81

Fig. 6.1: Schematic illustration of the Clamped-Clamped (CC) beam resoswitch, featuring a central input beam and two symmetric output beams positioned on either side. The symmetric design enhances the overall performance of the resoswitch by reducing losses and minimizing the likelihood of squegging.....86

Fig. 6.2: (a) COMSOL simulation of the CC-beam Ru Resoswitch demonstrating a displacement gain of $\sqrt{2}$, where the output beam displacement is $\sqrt{2}$ times greater than that of the input beam. (b) COMSOL simulation of the CC-beam Ru Resoswitch with a displacement gain of 2, showing the output beam displacement to be approximately twice that of the input beam.....89

Fig. 6.3: Schematic illustration of the Clamped-Clamped (CC) beam resoswitch design featuring separated input beams connected by very short coupling beams. This design is intended to address potential fabrication challenges associated with wide input beams, such as difficulties in fully etching the sacrificial layer beneath the structure. By dividing the input beam into narrower segments and coupling them, the design maintains equivalent performance to the wide beam configuration while improving manufacturability. The separated input beams are expected to exhibit similar displacement amplification and mechanical behavior as the original wide beam design, making this approach a practical alternative for achieving comparable functionality.....89

Fig. 6.4: (a) COMSOL simulation of the CC-beam Ru Resoswitch with separated input beams illustrating a displacement gain of $\sqrt{2}$, where the output beam displacement is $\sqrt{2}$ times greater than that of the input beam. (b) COMSOL simulation of the CC-beam Ru Resoswitch with a

displacement gain of 2, showing the output beam displacement to be approximately twice that of the input beam. The separated input beams, connected by very short coupling beams, effectively function as a displacement amplifier.....90

List of Tables

Table I: Design equations linking the mechanical properties of the resoswitch to their corresponding circuit elements.....	17
Table II: Example Resoswitch Designs.....	24
Table III: Predicted And Measured Pre-Energized Resoswitch Performance.....	48
Table IV: Resoswitch Design and Performance.....	63
Table V: Clamped-Clamped Beam Resoswitch Design Summary with Equations.....	87

Acknowledgements

First and foremost, I would like to express my deepest gratitude to my parents for their unwavering love, support, and encouragement throughout my academic journey. Their belief in me has been my greatest motivation, and their sacrifices have laid the foundation for everything I have achieved. Their wisdom and guidance have inspired me to persevere during the most challenging times. I would also like to acknowledge my beloved cat, Baobao Jin, whose companion has brought immeasurable joy and comfort during countless late nights and demanding moments.

I am profoundly grateful to my advisor, Professor Clark Nguyen, for his exceptional mentorship, insightful feedback, and unrelenting support throughout the course of my research. His vast knowledge and patient guidance have been instrumental in shaping this dissertation and expanding my intellectual horizons. I am deeply appreciative of his belief in my potential and the opportunities he has provided me to grow as a researcher and engineer.

My heartfelt thanks go to the members of my dissertation and qualifying exam committee: Professor Liwei Lin, Professor Ming C. Wu, and Professor Alp Sipahigil. Their time, effort, and constructive critiques have significantly enriched my research. Their insightful questions and discussions challenged me to think critically and strengthened the overall impact of my work.

I extend my sincerest appreciation to my lab mates, Kevin Zheng, Xintian Liu, Kieran Peleaux, and Alper Ozgurluk, for their camaraderie, collaboration, and shared dedication to pushing the boundaries of knowledge. The hours we spent troubleshooting, brainstorming, and celebrating small victories have been a vital part of this journey. I am particularly grateful for the moments of humor and encouragement that helped make the long hours in the lab more enjoyable and fulfilling.

Additionally, I would like to thank the staff and faculty members of the EECS department for their assistance and support throughout my time at the university. Their hard work and dedication behind the scenes have provided the resources and environment necessary for my academic pursuits.

I am incredibly grateful to the staff and labmates of the Berkeley Marvell Nanolab, including Ryan Rivers, Sam Tsitrin, Daniel Martinez, Zeying Ren, Min He, and many others who have supported me throughout the fabrication process. Their expertise, patience, and willingness to help have been invaluable. The time spent in the lab, overcoming challenges and refining techniques, was made possible by their guidance and encouragement. Their contributions have been integral to the success of my research, and I will always treasure the memories of collaboration and learning that took place in the Nanolab.

Finally, to my extended family, friends, and mentors who have cheered me on and reminded me of the bigger picture, I am truly grateful. Your encouragement and understanding have provided the strength I needed to keep going.

This dissertation is the culmination of the support and contributions of many, and I am deeply indebted to all those who have been part of this journey. Thank you for helping me achieve this milestone.

Chapter 1

Introduction

The concept of the Internet of Things (IoT)—a network of interconnected objects equipped with electronics—has steadily advanced since its inception in 1982 [1]. Today, we rely on environments densely populated with sensors that gather, exchange, and process data, providing a multi-dimensional understanding of our surroundings. Electric vehicles, for instance, are equipped with over 100 sensors to monitor and control critical parameters such as temperature, pressure, and system performance, ensuring safe navigation and operation. Similarly, everyday devices like smartphones and wearables are embedded with a wide array of sensors, including accelerometers and LiDAR scanners, while smart homes utilize sensors to measure temperature, humidity, and motion. Currently, more than 18 billion IoT devices are connected globally, and this number continues to grow exponentially [2].

Despite the rapid expansion of IoT, energy consumption has emerged as a significant challenge for the deployment of these vast sensor networks. While cost considerations remain important, the limited energy capacity of typical power sources constrains the long-term operation of wireless sensors. For example, a standard lithium coin cell battery stores approximately 600J of energy, which would allow a sensor to operate for a year only if its power consumption is limited to 19 μ W. With IoT applications spanning environments from building rooftops to the ocean floor, sensors must be deployed across vast areas to collect data on air quality, traffic patterns, and even submarine [3]. However, powering trillions of sensors becomes impractical with current technologies, given the cost and energy limitations. Printed batteries, though more affordable, store only about 1J of energy in a 1.6mm² form factor [4], requiring an even more drastic reduction in power consumption—below 31nW for a one-year lifespan. Current devices, however, still consume power in the milliwatt range, highlighting the pressing need for innovation [5].

The wireless communication module is one of the most power-hungry components within a sensor node. As such, developing extremely-low-power wireless communication technologies is essential for realizing the potential of large-scale IoT sensor networks. This thesis addresses these challenges by focusing on the design and optimization of wireless receivers, with an emphasis on enhancing performance, reducing power consumption, and improving frequency stability. The following chapters will delve into the principles and innovations that make these advancements possible.

1.1 Wireless Receiver Front-End

The conventional receiver front-end is depicted in Fig. 1.1(a). Here, a signal source (which could be an antenna or similar) carrying the information to be received feeds a bandpass filter that removes interferers before forwarding the signal to a low noise amplifier (LNA), which then amplifies the signal and directs it to demodulation circuits. As depicted in Fig. 1.1(a), any nonlinearity in the LNA (or other parts of the receiver) can interact with interferers, e.g., via intermodulation distortion or other nonlinear mixing [6], to generate unwanted spurious signals that might fall right into the desired channel, masking the desired signal and degrading or denying signal reception. Since these spurious signals derive from nonlinearity, a perfectly linear LNA could outright prevent them. Unfortunately, perfect linearity is not practically possible. In addition, linearity generally comes at the cost of power consumption.

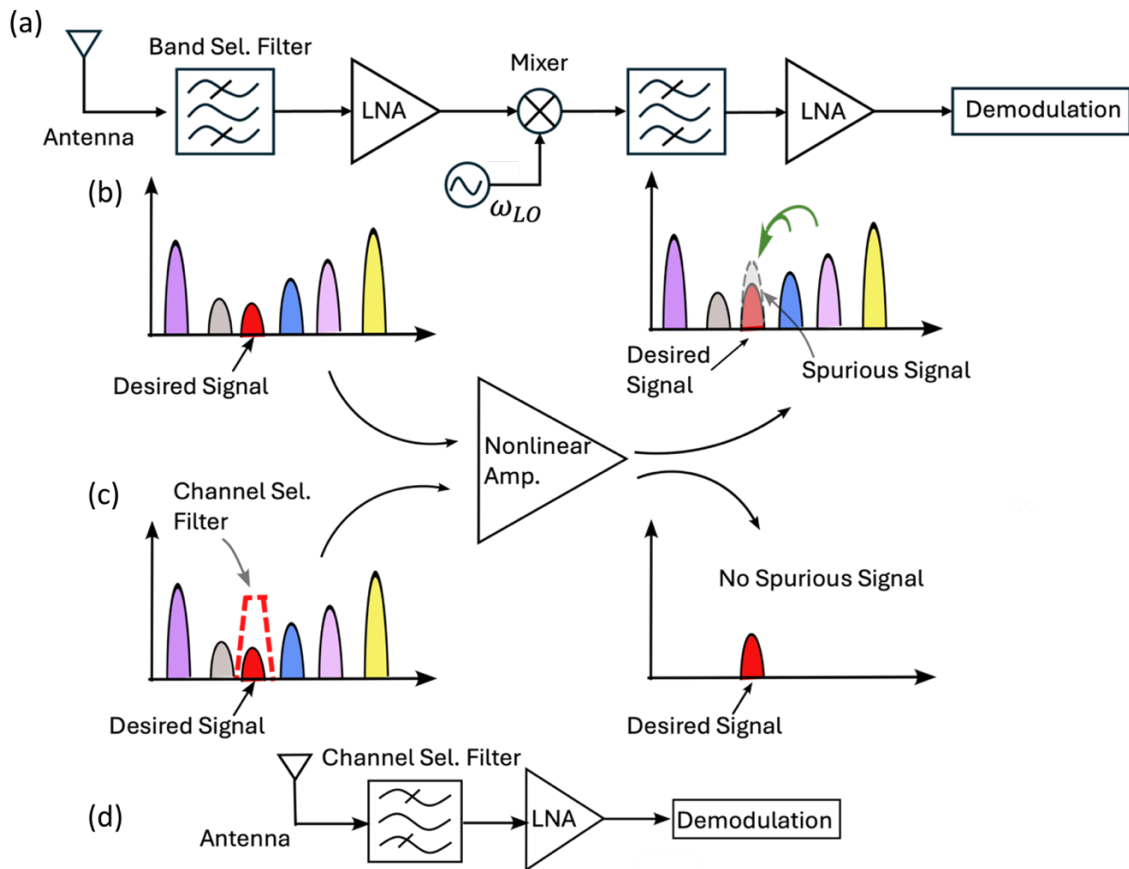


Fig. 1.1: (a) A schematic overview of a conventional receiver front end, highlighting the critical role of the low noise amplifier (LNA) in ensuring proper functionality. (b) The spectrum input to the LNA in a conventional receiver front end after the band-select filter, showing nearby interferers that can overshadow the desired signal after amplification by the LNA. (c) The spectrum input to the LNA after a channel-select filter, where interferers are significantly attenuated, reducing the likelihood of spurious signals. (d) An ideal receiver front end concept achievable through the use of a resoswitch.

In the Fig. 1.1(a) circuit the linearity required of the LNA depends heavily on the capability of the preceding bandpass filter. Normally, a conventional filter using LC , SAW, FBAR, or ceramic technology cannot remove all interferers, so a typical spectrum directed to the LNA input is as shown in Fig. 1.1(b). Here, the LNA need not handle extremely strong interferers, but must still handle close-by ones that are often several tens of decibels more powerful than the desired signal. To maintain adequate linearity, a conventional LNA generally operates at a bias point situated in the linear region of its transfer function, as shown in Fig. 1.2(b), where for simplicity an inverter amplifier (Fig. 1.2(a)) illustrates the concept with the understanding that conventional LNAs generally feature more complex biasing schemes to facilitate matching. The figure also shows how the bias point that maximizes linearity (Point A) often also maximizes the DC current draw, thereby maximizing power consumption.

On the other hand, quick inspection of Fig. 1.2(b) reveals that a much lower power draw ensues at bias point B . Unfortunately, the zero slope at this point means no linear gain, as the LNA drive transistor would be off. However, if the goal is to charge the output capacitor to a high voltage, then this is still possible if the input signal excursion were large enough to exceed the switching threshold V_{switch} , where the voltage transfer characteristic (VTC) transitions from an output low at point B to an output high at point C . Here, the amplifier essentially serves as a comparator. If the amplifier has an (ideal) infinite gain, as depicted in Fig. 1.2(c), then the minimum detectable signal would approach $0V$, being limited by noise and placement of the input bias point.

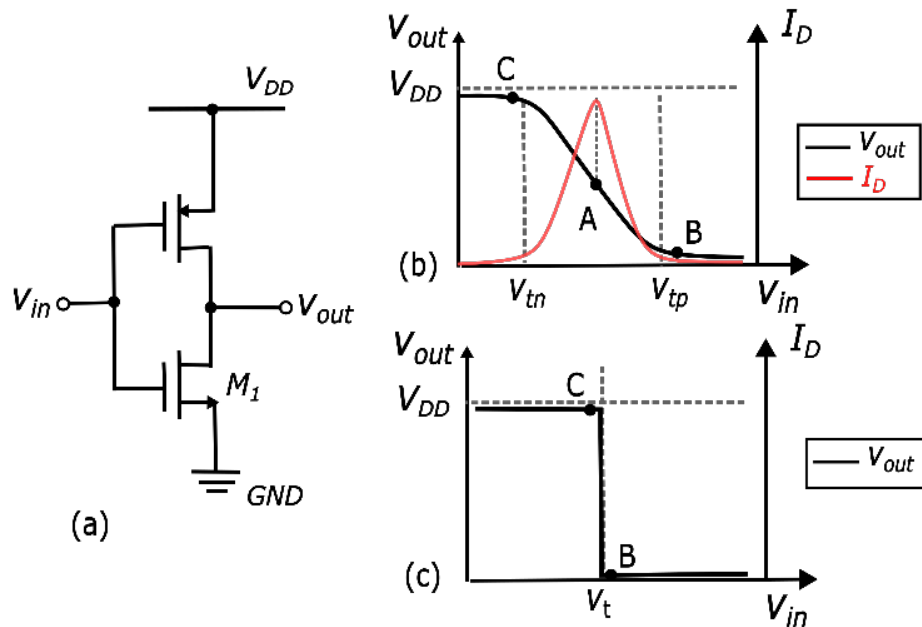


Fig. 1.2: (a) Schematic of a CMOS inverter amplifier. (b) The I - V curve of the inverter amplifier illustrates that maximum linearity (Point A) corresponds to the highest power consumption. To reduce power consumption, Point B is preferred, but it results in minimal linear gain, which is undesirable. (c) The issue can be resolved if an amplifier with infinite gain is realized.

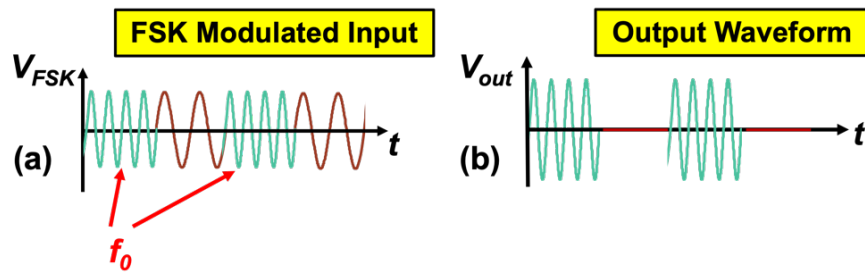
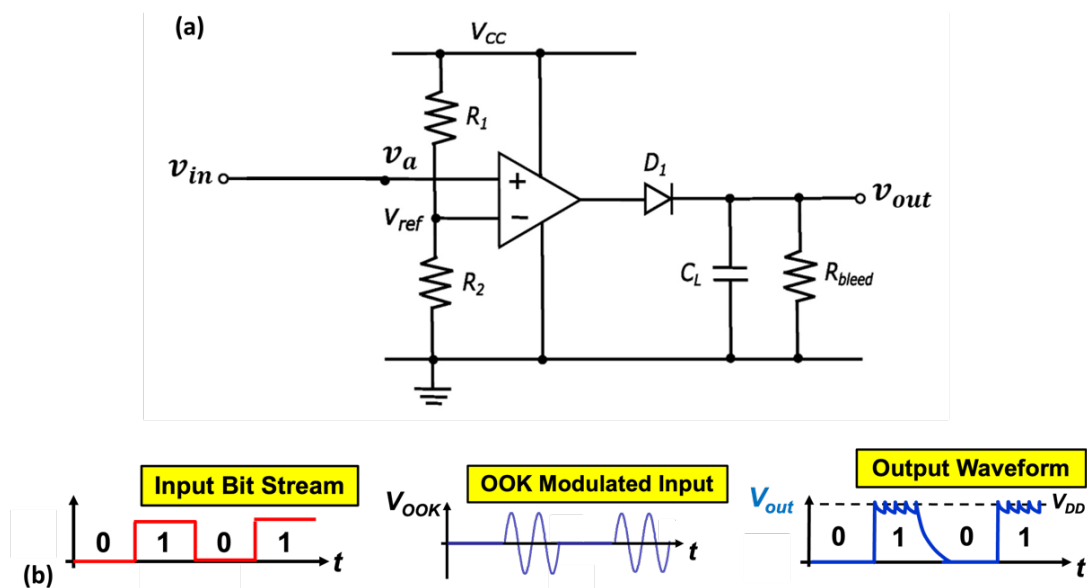


Fig. 1.3: (a) Input FSK waveform applied to a conventional LNA. (b) Expected output waveform, where the output toggles between low and high voltages in response to the valid input sinusoidal wave crests at the amplifier's operating frequency (f_0). When the input signal falls outside the amplifier's working frequency range, the output remains zero.

If the input signal were an ac signal, e.g., like the FSK waveform of Fig. 1.3(a) then the output would switch from low to high and back as sinusoidal wave crests come and go, as shown in Fig. 1.3(b). This then necessitates use of a (preferably ideal) diode to maintain an output high charge on load capacitor C_L . The circuit would be as in Fig. 1.4(a), which if all components were ideal represents one way to realize a receiver with zero quiescent power consumption.

This circuit readily demodulate an OOK input, such as in Fig. 1.4(b). Here, when the input is 0V, the comparator output remains at 0V, outputting a '0'; and when the input is a finite sinusoid large enough to traverse the comparator threshold, then an output high appears across the output diode, signifying a '1'.



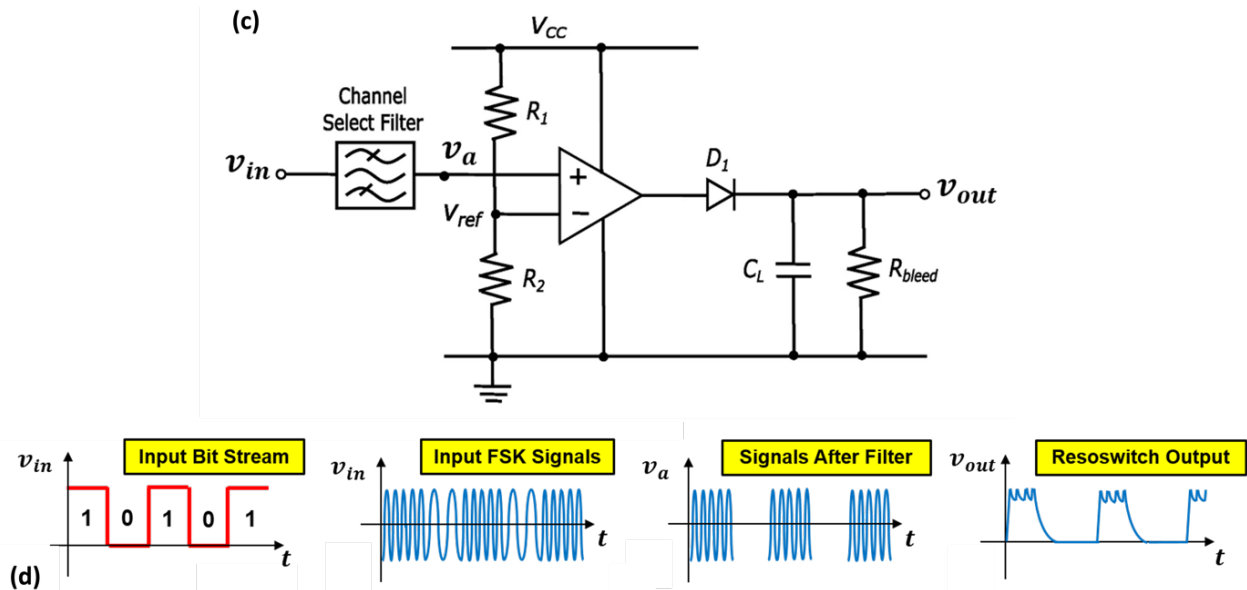


Fig. 1.4: (a) Schematic of a comparator-diode-capacitor circuit capable of demodulating an OOK (ASK-modulated) input signal to reproduce the input bitstream at the output load under ideal component conditions. (b) By incorporating a channel select filter, the circuit can also demodulate an FSK-modulated input signal, restoring the input bitstream at the output load (d).

Despite its simplicity, the Fig. 1.4(a) circuit can also demodulate an FSK-modulated input in an On-Off Keyed (OOK) fashion with the addition of a preceding bandpass filter, as shown in Fig. 1.4(c) and appropriate selection of mark and set frequencies. Specifically, if the mark and set frequencies are within and outside the filter passband, respectively, then only mark frequencies will get through to the comparator-diode-capacitor circuit. So only '1's charge load capacitor C_L to a high voltage, while '0's permit bleed resistor R_{bleed} to discharge it to ground. Ultimately, any '1' of the original bit stream produces a '1' at the receiver output, and any '0' produces a corresponding '0' at the output, as shown in Fig.1.4(d). Since only '1's are actually detected, this scheme does not realize full FSK reception, which requires detection of '0's as well. It does, however, realize a valid OOK receiver, at least if all components are ideal.

Unfortunately, a real implementation of Fig. 1.4(c) would fall far short of ideal. To start, if realized using transistors, leakage currents alone would negate any prospect for zero quiescent power consumption, allowing at best what some call "near zero power consumption". In addition, the finite subthreshold slope of transistors precludes a transition as sharp as depicted in Fig. 1.2(c). Rather, a transition like that in Fig. 1.2(b) is more realistic, and this means the detectable input signal excursion must be at least the distant between points B and C, suggesting that a very large (power consuming) gain would be required for this circuit to respond to the microvolt input voltage swings typically seen by wireless receivers.

If the bandwidth of the bandpass filter is similar to the typical band-select variety in current use (as opposed to channel-select), then perhaps more important than any of the above drawbacks is the sheer nonlinearity of the Fig. 1.4(c) circuit. Granted, it is in fact its highly nonlinear operation that permits this circuit to operate with such low power consumption. The battery draw could even be zero in a dormant listening state if the transistor (or other switching

device) were ideal. Unfortunately, however, given the prospects for spurious signal generation described above, as seen in Fig. 1.1(a), the sheer nonlinearity of this circuit makes it unusable in practical communication scenarios, where interferers abound, and assuming use of a conventional band-selecting (as opposed to channel-selecting [7]) bandpass filter.

Nevertheless, circuits like this have been proposed, such as those of [8] and [9], which dispense with the comparator portion and just use a diode or nonlinear transistor in an effective envelop detector circuit. Without the comparator, the time for signal acquire becomes impractically long for standard communications, although possibly acceptable for low duty cycle trigger detectors. Whether or not it employs a comparator, circuits like these still suffer from nonlinear spurious signal generation, so can be jammed or spoofed very easily. They also do not operate with truly zero quiescent power consumption.

Achieving true zero-quiescent power reception requires a fundamentally different approach, which is demonstrated in this thesis through an all-mechanical implementation. This design addresses the nonidealities discussed above, enabling genuine zero-quiescent power operation. It integrates all stages and the functionalities depicted in Fig. 1.1(c)(d) into a single micromechanical resonant switch, known as a resoswitch.

1.2 Review of Resoswitches & Previous Work

Resonant switches, or resoswitches, are microelectromechanical system (MEMS) devices that integrate resonators and switches into a single component [10]. They operate by utilizing mechanical resonance to actuate switching functions, making them highly efficient in terms of energy consumption and performance. As the demand for ultra-low-power devices continues to grow, particularly in fields such as wireless communication, the IoT, and distributed sensor networks, resoswitches have emerged as a key enabling technology.

A resoswitch is a type of mechanical switch that operates by periodically driving a resonator into sustained oscillation at its natural resonance frequency. When the oscillation amplitude surpasses a critical threshold, the resonator makes physical contact with an electrode, producing a switching event. This periodic impact-based operation sets the resoswitch apart from conventional RF MEMS switches, which typically rely on quasi-static electrostatic actuation and remain in a fixed ON or OFF state until the actuation voltage changes. This key distinction leads to significant differences in power consumption, switching dynamics, and system integration. The use of mechanical resonance allows the device to store and utilize vibrational energy to toggle the switch, enabling fast switching speeds with minimal power draw [11]. This is particularly beneficial in scenarios requiring zero or near-zero quiescent power consumption when inactive, making resoswitches ideal for energy-constrained environments.

In resoswitch design, two critical parameters are the resonance frequency and the quality factor (Q-factor). The resonance frequency defines the operational range of the device, determining its suitability for various applications, such as AM, FM, or higher frequency systems. The Q-factor plays a significant role in determining the energy dissipation within the system, with higher Q-factors corresponding to reduced energy losses during operation. As a

result, high Q-factor resoswitches are favored for low-power applications. Additionally, the Q-factor is related to the device's sensitivity, defined as the minimum input level at which the resoswitch can switch and generate reliable output. A higher Q-factor is desirable for improved sensitivity, allowing for more efficient signal detection.

Previous members of our research group have designed, fabricated, and tested various resoswitch architectures featuring diverse structures, including disk resonators [12] and comb drives [13], with electrostatic actuation being the predominant activation mechanism. The material selection for resoswitches is application-dependent, with silicon, nickel, and gold being common choices due to their favorable electrical and mechanical properties. Several fabrication methods exist for constructing resoswitches. For example, polysilicon comb-driven resoswitches are typically fabricated using LPCVD polysilicon deposition, while electroplated resoswitches—such as those plated with gold—offer superior mechanical durability and lower electrical resistance, making them well-suited for high-performance and high-frequency applications [14].

Wei-Chang Li, Yang Lin, et al. [12] implemented a wine-glass mode disk resonator as a resonant switch, operating at 61 MHz with a 2.5 V AC drive signal, causing it to impact electrodes along an orthogonal switching axis. This mechanism enables the switch to close a circuit through the switch-axis electrodes, as shown in Fig. 1.5. This disk-based resoswitch demonstrated significantly improved performance compared to conventional RF MEMS switches, achieving a remarkably fast switching time of 16 ns, high reliability with over 16.5 trillion hot-switching cycles, and a low actuation voltage of 2.5 V. Further advancements in disk resonator-based resoswitches include the use of electroplated nickel as a structural material [15], as illustrated in Fig. 1.6.

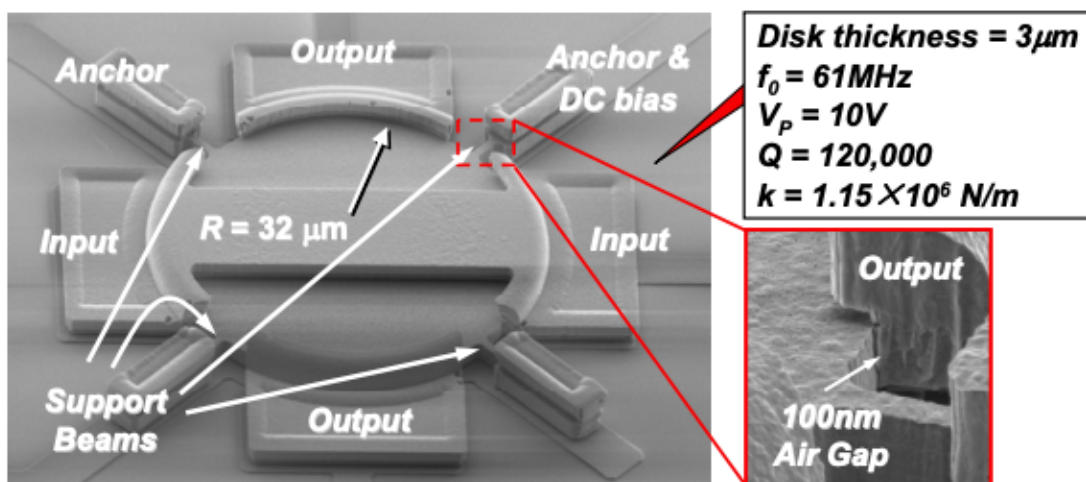


Fig. 1.5: (a) SEM of the polysilicon resoswitch demonstration used in [12], which comprises a wine-glass disk resonator with properly spaced and positioned input/ output electrodes; and (b) zoom-in view of the electrode-to-resonator gap of the device along the switch axis.

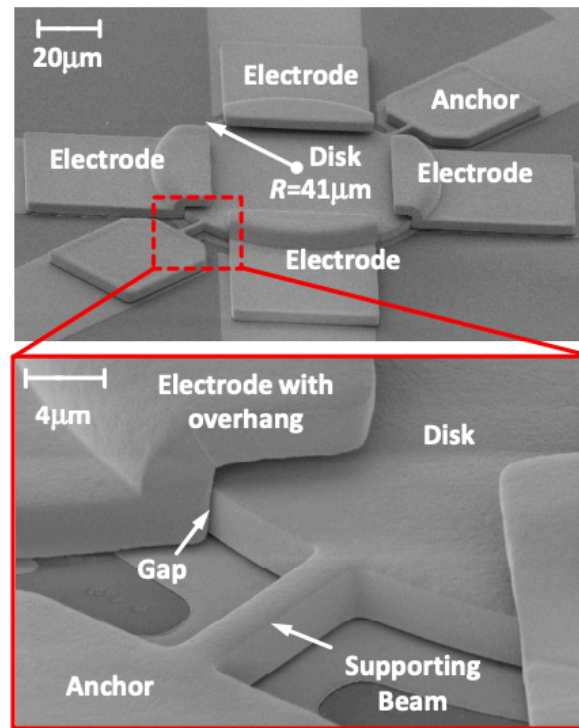


Fig. 1.6: SEM of a 25-MHz wine-glass mode electroplated-nickel disk resonant switch, with a zoom in view of an anchor and the electrode-to-disk gap [15].

In addition to disk resonators, Yang et al. pioneered the development of the first comb-drive-based resoswitch [23]. Building on this foundation, Ruonan Liu et al. advanced the design by creating a comb-drive-based resoswitch specifically for very low frequency (VLF) communication. VLF and Low Frequency (LF) receivers operating from 3-30 kHz and 30-300 kHz, respectively, with wavelengths on the order of kilometers, already serve very long-range (intercontinental) communications applications, such as depicted in Fig. 1.7. While high frequency radio waves propagate omnidirectionally along line-of-sight paths, so suffer from free space path losses proportional to the square of the distance between transmitter and receiver; VLF and LF signals propagate by surface wave through an effective waveguide formed by the ionosphere and the earth that confines their energy to follow the curvature of the earth, and hence, suffer less loss [13]. Such frequencies are presently used for time transfer over long distances, where their propagation by ground wave eliminates multipath issues, ultimately helping to maintain timing precision. Integrating VLF communication with the zero-quiescent-power resoswitch receiver concept demonstrated in prior research could unlock new applications, enabling remote sensors and autonomous devices to be commanded or interrogated from hundreds of miles away. This comb-driven resoswitch, depicted in Fig. 1.8(a), utilizes electroplated gold as its structural material, leveraging the advantages of gold discussed in [14]. However, challenges such as limited device lifetime, frequency instability due to squegging [17][41], as seen in Fig. 1.8(b), and potentially restricted bit rate in low-frequency operation necessitate further investigation and optimization. These issues will be systematically addressed in later chapters of this thesis (Chapter 3 and Chapter 5).

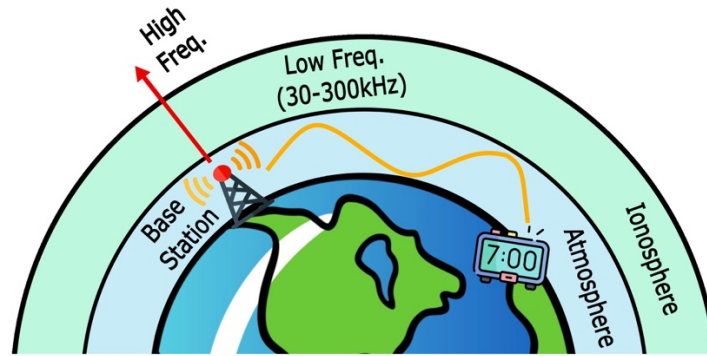
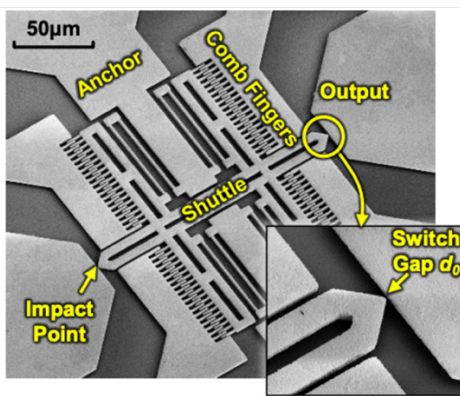
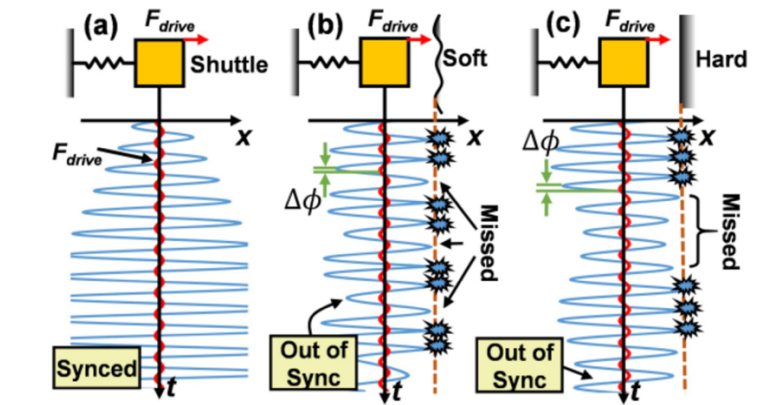


Fig. 1.7: Very-Low-Frequency (VLF) and Low-Frequency (LF) communication systems enable long-distance and cross-continent signal transmission.



(a)



(b)

Fig. 1.8: (a) SEM image of an electroplated gold comb-drive-based resoswitch from [13]. (b) Illustration of squegging behavior as described in [41]: Simulated transient waveforms demonstrating (a) no impacts, (b) small phase shifts ($\Delta\phi$) for soft impacts, and (c) large $\Delta\phi$ for harder impacts. In this phenomenon, phase shifts cause the resoswitch to lose synchronization with the driving force, reducing impact efficiency. As a result, the resoswitch temporarily stops impacting for several cycles until it re-synchronizes with the input force and resumes normal operation. Such missed impacts can introduce output errors and frequency instability. Investigations into both soft and hard contact resoswitch designs have been conducted; however, squegging-induced frequency instability remains unresolved.

The primary application of resoswitches lies in extremely-low-power wireless communication systems. They are particularly suited for use in energy-harvesting devices or systems where battery replacement is impractical, such as IoT sensors distributed across vast areas. The ability of resoswitches to operate at very low power levels, often in the nanowatt range, makes them ideal candidates for future sensor networks where power efficiency is paramount. Additionally, resoswitches play a critical role in the development of zero-quiescent-power receivers, which only consume power during valid signal reception. This feature is essential for applications in remote or autonomous devices, such as environmental monitoring systems, where sensors must remain operational for extended periods without external power sources.

1.3 Dissertation Overview

This dissertation presents a comprehensive investigation into the design, fabrication, and implementation of resoswitches for extremely-low-power wireless communication systems at Very-Low-Frequency (VLF)/ Low-Frequency (LF) range. The research is driven by the growing need for energy-efficient devices, particularly in the IoT and sensor networks, where minimizing power consumption is critical. Resoswitches, with their capability to operate at zero or near-zero quiescent power, emerge as a promising solution to these power-related challenges.

The dissertation first explores various design methodologies, assessing different structural configurations aimed at optimizing the performance of wireless receiver front-end systems. It then delves into the fundamental principles of resoswitch technology, focusing on their operational mechanisms and material properties. A significant emphasis is placed on the experimental validation of these designs through rigorous testing and analysis of the resoswitches' performance in practical applications. During the fabrication process, several techniques are evaluated to enhance both mechanical robustness and electrical efficiency, including the use of electroplating and advanced materials such as ruthenium.

The dissertation introduces the concept of bit rate-adapting resoswitches, which use stored resonance energy to dynamically adjust to varying input data rates. This capability is crucial for operating in power-constrained communication channels and represents a significant advancement in resoswitch functionality. Experimental results demonstrate the ability of these devices to achieve reliable communication even under limited bandwidth (high Q) and power conditions.

Additionally, the integration of ferrite-rod antennas with resoswitch receivers is explored and demonstrated to enable wireless operation. It addresses key challenges such as impedance matching and frequency tuning, which are critical for real-world implementations. The dissertation evaluates the impact of antenna bandwidth limitations on system performance and proposes methods to optimize this integration for low-bit-rate communication.

The study also addresses key challenges related to frequency instability and power dissipation, offering innovative design modifications to overcome these issues. A detailed discussion of the experimental results is provided, highlighting the advantages of "Push-Pull" resoswitch receivers and their suitability for integration into next-generation extremely-low-power communication networks.

The dissertation concludes with a reflection on the research contributions made and offers insights into potential future developments in the field. This includes exploring alternative resoswitch designs, refining fabrication processes, and broadening their application to energy-constrained environments, further advancing the field of energy-efficient communication systems.

Chapter 2

Design and Fabrication of Resoswitches

This chapter details the structural design principles and fabrication processes developed for micromechanical resonant switches, or *resoswitches*. The chapter begins by introducing the comb-driven resoswitch structure and its fundamental mode of operation, followed by a description of the design considerations that influence performance. It then explores the materials selection process and fabrication techniques—including electroplating and mold preparation—that were optimized to produce high-yield, mechanically robust devices. Special attention is given to the challenges encountered during the transition from gold to alternative structural materials, such as ruthenium.

2.1 Comb-Driven Resoswitch Structure and Operation

The circuit of Fig. 2.1(b) constitutes a micromechanical realization of the Fig. 2.1(a) circuit, where mechanical implementation is key to removing the nonidealities described in the previous section, ultimately allowing for true zero-quiescent power operation. It realizes all stages of Fig. 2.1(a) and functions of Fig. 2.1(a) via the single micromechanical resonant switch, a.k.a., resoswitch, of Fig. 2.1(b) which itself comprises a conductive gold metal folded-beam comb-driven resonant structure designed to impact a gold output electrode upon achieving adequate displacement amplitude [17]. The resonant structure employs many of the same mechanisms as folded-beam comb-driven predecessors [13] including:

- 1) shuttle comb fingers inter-digitated with electrode fingers to linearize the electrostatic voltage-to-drive force transfer function, as well as increase the permissible displacement range; and
- 2) etch holes to lighten the shuttle mass (for higher frequency) and reduce the time needed to release the device.

The resonant structure also deviates from those of past literature in its employment of mechanisms to minimize the effect of post fabrication stress and to facilitate the impacting function of a resoswitch. Specifically, the structure of Fig. 2.1(b) employs

- 1) centralized anchoring of the folded beam suspensions that further reduce the impact of in-plane stress (beyond the benefits of folding) while permitting a geometry suitable for the

large oxide mesa-supported anchor needed by the one-mask surface-micromachining fabrication process used here, cf. Section 2.3; and

- 2) an impactor protrusion that sets the impacting gap distance between the resonant shuttle and the impact electrode while also tailoring the impact impulse by choice of geometry, e.g., sharp, square, rounded tip.

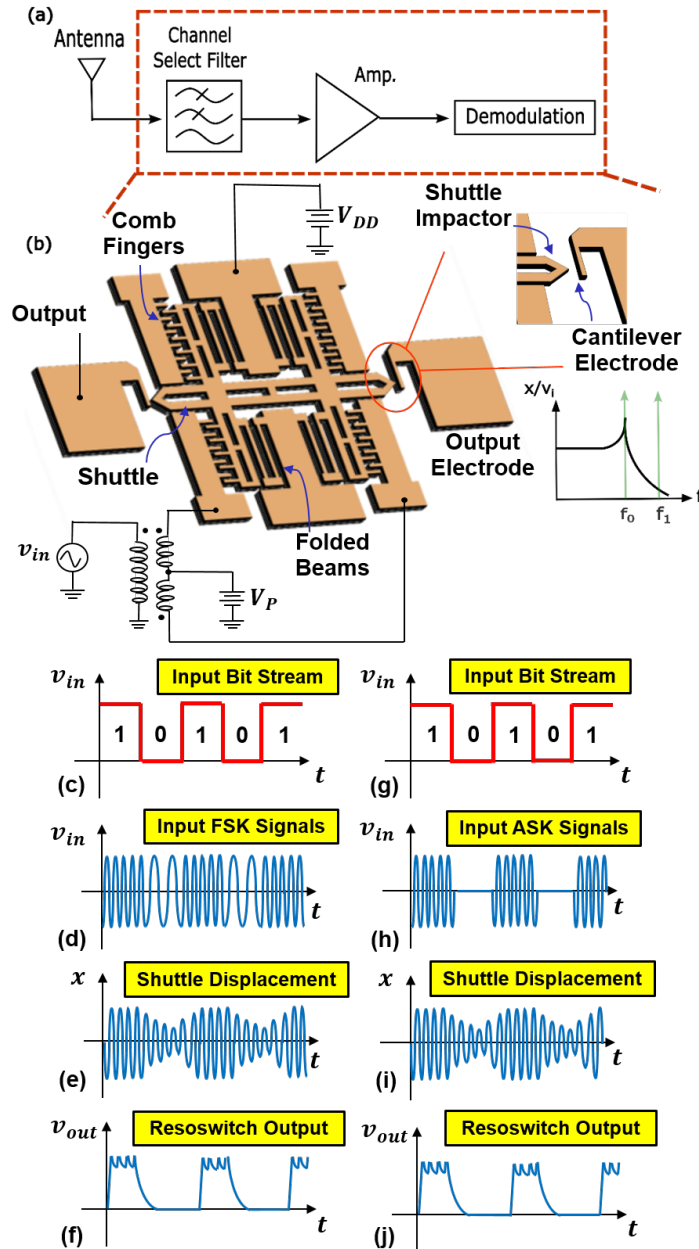


Fig. 2.1: Mechanical implementation of a receiver front end (a) utilizing a resoswitch receiver (b). For FSK-modulated input signals (c) and (d), the movable shuttle of the resoswitch displaces and impacts the output electrodes (e), reproducing the input bitstream at the output (f). Similarly, the resoswitch receiver can process ASK-modulated input signals (g) and (h), yielding the corresponding output bitstream (j), with analogous shuttle displacements illustrated in (i).

Here, the frequency response of the folded-beam micromechanical resonator [17] realizes the channel select filter of Fig. 2.1(a), which because of its very high Q exceeding 500, has a passband narrow enough to be channel selecting. This ability to channel-select allows reception of only the on-resonance mark frequency and rejection of off-resonance signals, including the set frequency (in FSK) and all interferers. Removal of all interferers precludes nonlinear generation of spurious signals and thereby outright permits the use of the heavily nonlinear comparator-based approach of Fig. 2.1(a).

The resoswitch of Fig. 2.1(b) realizes the comparator function via resonant mechanical impact switching, where the Q of the resonator provides a pre-comparator electrical-to-mechanical gain that allows detection of very small signals, while the gap between the shuttle impact point and the output electrode defines the comparator threshold. An on-resonance mark input induces a resonator shuttle resonance displacement amplitude that exceeds this threshold, thus triggering impact-induced shuttle-to-output electrode contact and a resultant charge transfer between the power supply V_{DD} and load capacitor C_L that raises the output voltage to V_{DD} , i.e., to an output high or ‘1’. Meanwhile, the shuttle remains stationary upon reception of a (off-resonance) set frequency, allowing bleed resistor R_{bleed} to discharge C_L to ground, i.e., an output low or ‘0’.

2.1.1 Resoswitch Versus Conventional MEMS Switch

To better appreciate the details of resoswitch design, it is instructive to first review the attributes that permit this device to excel in this zero-quiescent power application. Specifically, as described in [16][18], the micromechanical resoswitch provides the same benefits that conventional aperiodic micromechanical switches have over transistor switches while also alleviating several of their limitations.

Like conventional aperiodic MEMS switches, the on/off switching slope of a resoswitch is quite steep, with a significantly steeper slope than the 70mV/decade subthreshold switching of a typical MOS transistor. This means the voltage transfer characteristic for both an aperiodic conventional MEMS switch and a resoswitch resembles more the ideal solid curve that switches quite abruptly, without the trailing low-gain end regions that constrain the minimum comparator threshold of a transistor implementation, as seen in Fig. 2.1(c)-(j).

Conventional aperiodic switches, of course, have the more important problem that their turn-on thresholds are generally quite large, on the order of >50V for RF MEMS switches [18]. Although near-pull-in biasing strategies have effectively reduced the threshold voltages of NEMS switches that target logic applications [19], the achieved thresholds are still on the order of single-digit volts and thus much greater than the microvolt input amplitudes of typical received wireless input signals.

The resoswitch used here solves this problem by virtue of resonance operation. Specifically, Q multiplication of its displacement at resonance allows it to impact-switch with very low power inputs. The impulsive contact force of resonance impacting operation also improves contact resistance and reliability, making possible previously measured cycle counts greater than 170 trillion [12] (for VHF resoswitches), which is several orders higher than aperiodic counterparts [20].

At first glance, the constraint to resonant or periodic inputs seems limiting when

compared to a conventional MEMS switch designed to switch via more general inputs. However, this is not a problem for a signal processing application like the present RF front-end application for which modulated carrier inputs are periodic by default. Periodic operation is in fact a benefit when one considers how it enables channel-select filtering to eliminate drawbacks derived from nonlinearity.

2.1.2 Practical Receiver Operation

The specific low frequency comb-driven resoswitch of Fig. 2.2 features a pair of output electrode impacting points at both sides of the shuttle. Four pairs of folded beams suspend the resonator shuttle from central anchor points. To suppress squegging [21] this resoswitch uses fully differential input comb electrodes and impact points, both of which help to overcome impact-induced energy loss. As shown in Fig. 2.2, the receiver takes as input a differential ac signal $\pm(1/2)V_{FSK}$ combined with a dc bias voltage V_P applied to resoswitch comb electrodes on opposite sides. The dc voltage ($V_P - V_{DD}$) and capacitance change per unit displacement across the resoswitch's comb capacitive transducer, together with the resoswitch's Q , set an effective electrical-to-mechanical gain for the device, where the larger these quantities, the higher the gain. The dc voltage source V_{DD} tied to the shuttle as shown in Fig. 2.2 serves as the supply to be switched to the output upon impact with the switch electrodes.

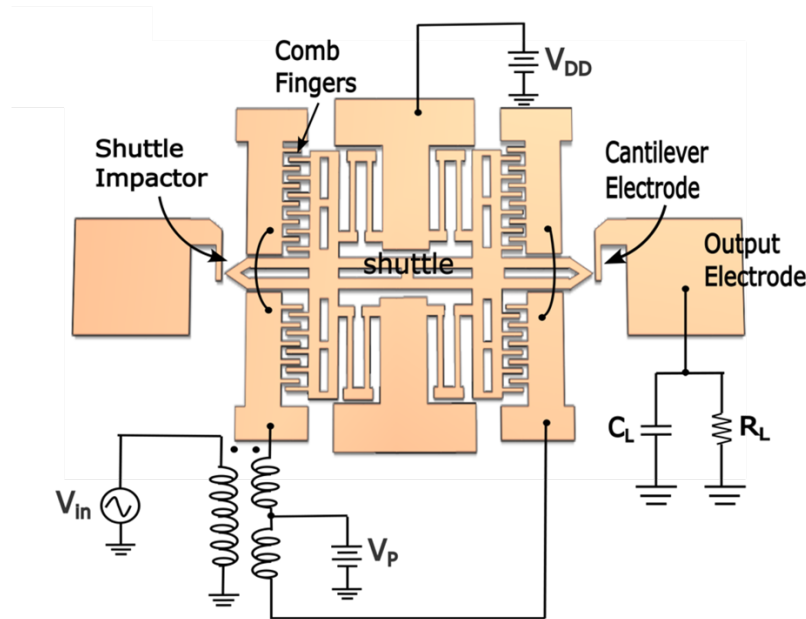


Fig. 2.2: schematic of a low-frequency comb-driven resoswitch receiver.

When the frequency of V_{FSK} is outside the resonator's passband, i.e., is an off-resonance set input, the resoswitch does not move enough to overcome the air gap of d_0 separating the shuttle impact points from the output electrodes, so is electrically open. When a V_{FSK} of sufficient amplitude appears within the frequency passband of the resoswitch, making it a mark input, the shuttle vibrates laterally with an amplitude approximately Q times larger than would

ensue with an out-of-band input. If V_{FSK} induces a shuttle displacement larger than the switch gap d_0 , the shuttle periodically electrically connects the output to V_{DD} , delivering charge to output load R_L and C_L on each impact.

When operating in this fashion, the receiver accepts a frequency-shift keyed (FSK) input but processes it in an on-off keyed (OOK) fashion, since it only really receives mark inputs. To support full FSK, which would then allow a smaller signal-to-noise ratio for a given bit error rate, the Fig. 2.2 receiver must add another resoswitch to detect set inputs.

Not surprisingly, the ultimate sensitivity of this all-mechanical receiver depends strongly on the details of the micromechanical resoswitch design.

2.2 Micromechanical Resoswitch Designs

2.2.1 Design Process

Resoswitches are comb-driven mechanical resonators equipped with mechanical stops that serve as output electrodes. The movement of the shuttle, which is suspended by folded beams, is driven by forces generated by the capacitive actuators formed between the comb fingers. These forces act in the lateral direction, causing the shuttle to move laterally. The resonance frequency of the resoswitch is determined by the equation:

$$\omega_0 = \sqrt{\frac{k_r}{m_r}} \quad (\text{Eq. 1})$$

where k_r is the stiffness of the folded beams, and m_r is the equivalent dynamic mass of the resoswitch. The dynamic mass is expressed as [22]:

$$m_r = m_s + 1/4 m_t + 12/35 m_b \quad (\text{Eq. 2})$$

Here, m_s represents the shuttle mass, m_t denotes the truss mass, and m_b is the total mass of the folded beams. At resonance, the displacement of the shuttle x_0 in response to the driving force F_0 is given by:

$$x_0 = \frac{F_0}{k_r} Q \quad (\text{Eq. 3})$$

where Q is the quality factor, and F_0 is the driving force generated by the change in capacitance between the comb fingers under an applied DC voltage V_P and an AC input voltage v_{in} . This force can be expressed as:

$$F_0 = V_P v_{in} \frac{\partial C}{\partial x} = \eta_e v_{in} \quad (\text{Eq. 4})$$

where η_e , the electromechanical coupling coefficient, is defined as:

$$\eta_e = 2NV_p \frac{\epsilon h}{g_f} \quad (\text{Eq. 5})$$

Here, ϵ is the vacuum permittivity, h is the thickness of the structure, N is the total number of comb fingers and g_f is the gap spacing between fingers.

For the resoswitch to impact the output electrodes, the shuttle must achieve a minimum displacement equal to the switch gap g_{switch} , which represents the distance between the shuttle's impactor and the output electrode. The input voltage v_{in} required to achieve this displacement defines the sensitivity of the resoswitch. However, when this minimum input is applied, the shuttle reaches the output electrode with zero velocity, leading to an enormous contact resistance. As the displacement increases with greater driving force, the contact velocity also increases, reducing the contact resistance and enabling faster charging of the output circuit. However, excessive contact velocity or impacting force can degrade the contact surfaces and disrupt the resonance dynamics of the system, leading to a phenomenon known as "squegging." [23] This phenomenon can significantly affect the performance and reliability of the resoswitch.

Given that the Fig. 2.1(a) receiver relies entirely on the mechanical resoswitch, proper design of this zero-quiescent power receiver comes down to proper design of the micromechanical resoswitch. This then necessitates a model and a set of analytical design formulations. Specifically, the design process requires quantitative formulations for the following:

1. Electrical equivalent circuit, including the motional resistance R_x of the resoswitch's resonant element,
2. Impact contact resistance,
3. Input sensitivity,
4. Maximum receive bit rate,
5. Bit error rate as a function of various contributors, such as noise, squegging, etc., and
6. Frequency mask, i.e., plot of minimum input power required to instigate impacting versus frequency.

The following sub-sections now address each of the above in sequence.

A. Resoswitch Equivalent Circuit

Maximum power transfer from the source, e.g., an antenna, into the resoswitch normally necessitates a conjugate match between the resoswitch input impedance and the source impedance. This in turn requires a formulation for the resoswitch's electrical equivalent circuit.

Given that the resonator portion of the device uses a classic folded-beam comb-driven structure, the literature already provides an equivalent circuit formulation [24]. Table I summarizes the circuit topology and design equations from [24]. The table indicates how the resonance frequency depends on a combination of material properties and mainly lateral dimensions, so is quite tailorable via CAD layout. A designer can easily achieve a bank of resoswitch receivers at various carrier frequencies to realize a multi-channel communication

system all in one fabrication process run on a single chip.

Table I: Design equations linking the mechanical properties of the resoswitch to their corresponding circuit elements.

Design Equations			
Equivalent Circuit Elements	Motional Inductance, L_x	$L_x = m_r / \eta_e^2$	Eq. 6
	Motional Capacitance, C_x	$C_x = \eta_e^2 / k_r$	Eq. 7
	Motional Resistance, R_x	$R_x = \sqrt{m_r k_r} / Q \eta_e^2$	Eq. 8

Just as important as frequency is the impedance seen looking into the resoswitch input. At resonance, the motional inductance L_x and capacitance C_x cancel, leaving the motional resistance R_x , which when reflected through the input transformers presents the resoswitch's input impedance, which takes the form

$$R_x = \frac{k_r}{2\pi f_0 Q \eta_e^2} = \frac{k_r}{2\pi f_0 Q V_P^2 \left(\frac{4N\epsilon h}{g_f}\right)^2} \quad (\text{Eq. 9})$$

Here, the size of device and its electrode-to-resonator gaps, as well as the dc-bias voltage V_P , serves as the most effective knobs to tailor R_x . Specifically, smaller size and gap spacing and larger V_P lead to smaller R_x .

For maximum power transfer, R_x should match the resistance of the input power source. For a VLF wireless application, the source is generally a ferrite core antenna, which at the 20kHz frequency of the demonstrated receiver herein has a source resistance on the order of 31 k Ω [25].

To gauge this design's ability to achieve a matching R_x , Table II summarizes three different designs. Here, the design in Table II design B achieves the needed impedance using the smallest dc bias voltage V_P , suggesting that performance improves as lithography improves. While the design B has features down to 250 nm, so is much smaller than most folded-beam comb-drive resonator designs, it is not unprecedented [26].

B. Impact Contact Resistance

The contact resistance of any mechanical switch is a function of the contact force. Expressions modeling contact resistance as a function of force abound in the literature, one which takes the form [27]:

$$R_{on} = R_0 - \varphi F_C \quad (\text{Eq. 10})$$

where R_0 is a low contact force initial resistance, and φ models the dependence of contact resistance R_{on} on contact force F_C . Here, $F_C = \frac{m_r(v_1 - v_1')}{t_c}$, where m_r is the shuttle mass, t_c is the contact time, and v_l and v_l' are the pre- and post-impact velocities, respectively, of the shuttle.

As a periodic switch, the contact resistance of a resoswitch fluctuates over time, reaching its lowest values when the impulsive impact force is at its peak. This dynamic behavior causes the current through the resoswitch to depend on the impact dynamics, which directly affects the rise time of the voltage across the output capacitor during charge reception.

Since contact resistance inversely scales with impact velocity, any variation in electrical contact resistance during impact alters the charging rate of the load capacitor (C_L), resulting in fluctuations in rise time and contributing to system instability.

C. Maximum Receive Bit Rate

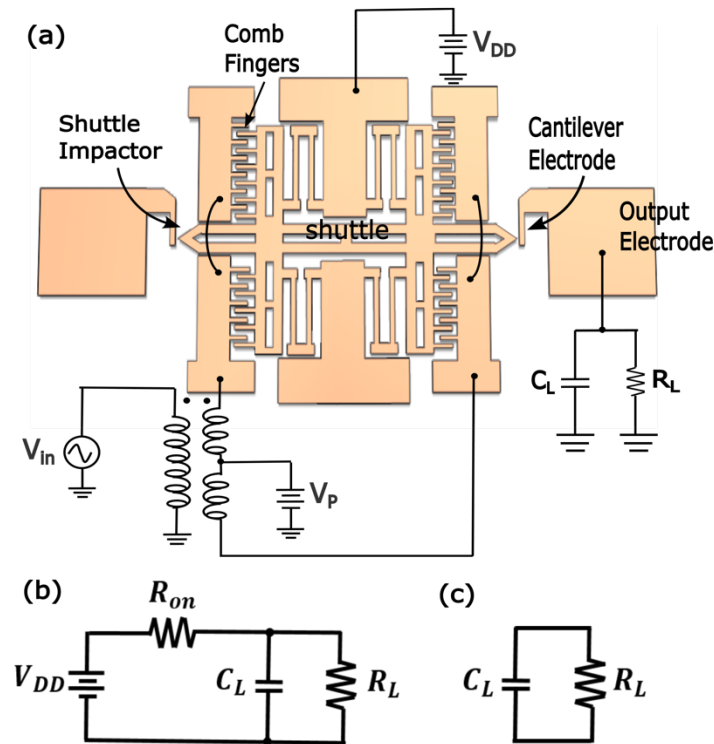


Fig. 2.3: Equivalent circuits of (a) the resoswitch receiver when it processes (b) an input “1” (charging the output load, R_L and C_L) and (c) an input “0” (discharging the load).

One factor that influences the maximum achievable receive bit rate is the charging rate of the output load capacitor, C_L . While the ultimate upper limit is set by the mechanical dynamics of the resoswitch itself—such as impact timing and oscillation frequency—the electrical charging behavior of C_L imposes an additional constraint that can limit bit rate performance in practical circuits. To analyze this behavior, Fig. 2.3(b) and Fig. 2.3(c) present the circuit configurations involving the resoswitch, R_L , and C_L when the input is “1” and “0,” respectively. The effective bit rate is thus influenced by the contact resistance R_{on} , the load resistance (also known as bleed resistance) R_L , and the capacitance C_L . The time required to charge C_L , defined as t_{rise} , is given by:

$$t_{rise} = 2.2\tau_{charge} = 2.2R_{on}C_L \quad (\text{Eq. 11})$$

When the input is “0”, C_L discharges through bleed resistance R_{bleed} , with the discharge time $t_{discharge}$ expressed as:

$$t_{discharge} = 2.2\tau_{discharge} = 2.2R_{bleed}C_L \quad (\text{Eq. 12})$$

The maximum bit rate achievable by the resoswitch receiver, constrained by the charging and discharging rates, is therefore:

$$f_{max} = \frac{1}{t_{rise}+t_{discharge}} \times 2 = \frac{2}{2.2(R_{on}+R_{bleed})C_L} \quad (\text{Eq. 13})$$

Other factors, including input power level, the resoswitch's resonance frequency, and input bit rate, may also constrain the maximum bit rate and need further investigation. A detailed analysis of achievable bit rates is presented in Chapter 3.

D. Input Sensitivity

Sensitivity threshold of the receiver is defined as the minimum input power needed for the shuttle to overcome the impactor-to-electrode gap, g_{switch} , and make contact (Fig. 2.4). This is expressed as:

$$S = \frac{g_{switch}^2 k_r \omega_0}{Q} \quad (\text{Eq. 14})$$

where k_r represents the dynamic stiffness of the resoswitch at the shuttle location, ω_0 is the resonance frequency, g_{switch} is the gap, and Q is the quality factor. A smaller gap spacing and higher Q factor both contribute to improved sensitivity. However, when input power is near the sensitivity threshold, the resulting high contact resistance limits achievable bit rate.

Moreover, since the maximum receive bit rate depends on input power, as discussed in Chapter 3, input sensitivity—defined here as the minimum input power required for the resoswitch to impact at a specified bit rate—varies accordingly with the target bit rate. Therefore, determining sensitivity necessitates first establishing the desired bit rate.

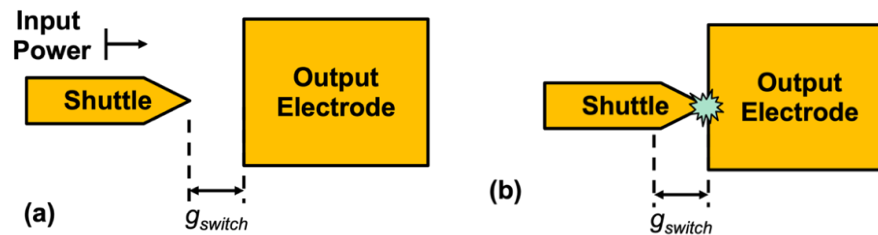


Fig. 2.4: Input power drives the resoswitch shuttle to move laterally, overcoming the gap spacing g_{switch} , making contact with the output electrode to transmit signals. The sensitivity threshold represents the minimum input power required to achieve this impact.

E. Bit Error Rate

Errors in resoswitch communications are attributable to two factors: errors due to thermal noise and errors due to squegging. Of these two factors, error due to squegging is presently the dominant factor limiting resoswitch performance.

a. Thermal Noise

There are two types of white thermal noise that contribute to bit errors in resoswitch devices: the noise from the damping internal to the resoswitch, and the noise present at the input of the resoswitch, both of which contribute to a displacement noise $x_{n,rms}$. In a resoswitch, two situations give rise to bit errors. The first is where a zero bit is registered as a one bit when the displacement of resoswitch shuttle caused by thermal noise is sufficient to overcome the gap. The second type of bit error due to thermal noise is where a one bit is incorrectly registered as a zero bit when thermal noise causes the resoswitch shuttle to lose contact with its outputs. This occurs when $x_{n,rms}$ is greater than the contact depth x_d , the distance past the resting displacement of the output electrode due to its finite stiffness that the shuttle travels. Since g_{switch} is typically larger than x_d , the second type of bit error is more common than the first in the case of no pre-energizing. When pre-energizing, both types of errors should be considered [17].

Internal damping noise from the resoswitch and voltage noise from the source resistance both contribute to $x_{n,rms}$. The resoswitch can be modeled as a damped simple harmonic oscillator whose damping contributes thermal noise by the fluctuation-dissipation theorem. The RMS displacement due to thermal noise from the damper, $x_{n,d}$ is given by integrating the spot noise of a simple harmonic oscillator across all frequencies:

$$\overline{x_{n,d}^2} = \frac{k_b T}{k_r} \quad (\text{Eq. 15})$$

Where k_b is Boltzman's constant, T is absolute temperature, and k_r is the equivalent stiffness of the resoswitch. In a typical 23-kHz resoswitch with $Q = 500$ at 300K, $x_{n,d}$ is in the picometer range and is small enough to ignore. The source noise x_s , whose noise voltage is converted to mechanical noise by a factor of η and is a function of the source resistance R_s :

$$\overline{x_{n,s}^2} = k T R_s \frac{\eta^2 Q}{\omega_0 m k_r} \quad (\text{Eq. 16})$$

To calculate the probability of a bit error, we need an estimate of the contact depth x_d . Assume that in steady state, the shuttle is in simple harmonic motion and energy is conserved. This is approximately valid because losses due to finite Q and damping at from the contacts are balanced by the external driving force. Equating potential energy stored in the contact springs to the maximum shuttle velocity:

$$\frac{1}{2} k_c x_d^2 + \frac{1}{2} k (x_d + g)^2 = \frac{1}{2} m v_{max}^2, \quad v_{max} = g \omega_0 \quad (\text{Eq. 17})$$

Where k_c is the output electrode stiffness, v_{max} is the maximum velocity of the shuttle, and g is the displacement amplitude, equal to the gap space. x_d can then be calculated by substituting for v_{max} and solving the resulting quadratic equation. For the resoswitch in this example, x_d is $0.27g$. Finally, the probability of a 1-to-0-bit error due to thermal noise is given by:

$$p_e = \Phi\left(-\frac{x_d}{x_{n,rms}}\right), \quad x_{n,rms} = \sqrt{x_{n,d}^2 + x_{n,s}^2} \quad (\text{Eq. 18})$$

Where Φ is the cumulative distribution function of the standard normal distribution. In the case of pre-energizing, 0 to 1 bit errors may be more common, in which case it is appropriate to replace x_d with $(1-M) \cdot g_{switch}$.

b. Squegging

Squegging is the dominant source of bit errors for resoswitch devices. Squegging occurs when the shuttle makes contact with the output electrode, disturbing the phase relationship between the drive voltage and displacement, decreasing the efficiency of the drive [23]. This causes the output to miss for a few cycles, and if the duration of the squegging is sufficiently long, results in a 1-to-0-bit error. The phase relationship disturbance occurs because impacting the output electrode temporarily shifts the resonant frequency with the addition of the output electrode stiffness. This fractional frequency shift is given by:

$$\Delta\omega = \frac{\omega - \omega_0}{\omega_0} = \sqrt{1 + \frac{k_c}{k}} - 1 \quad (\text{Eq. 19})$$

The phase shift due to squegging after N impacts can be found by time-averaging the fractional frequency shift. Assuming that impact occurs for fraction d of every half cycle, the phase shift after N impacts is given by:

$$\phi = Nd\Delta\omega \quad (\text{Eq. 20})$$

If there are two output electrodes, then the number of impacts per second is double the resonant frequency:

$$N = 2f_0 = \frac{\omega_0}{\pi} \quad (\text{Eq. 21})$$

Resulting in a phase shift per second given by:

$$\phi = 2f_0d\left(\sqrt{1 + \frac{k_c}{k}} - 1\right) \quad (\text{Eq. 22})$$

How much phase shift is necessary to result in a bit error? The resoswitch stops making contact if x_d becomes less than zero. Therefore, the “excess” energy in making contact is:

$$E_{excess} = \frac{1}{2} k_c x_d^2 \quad (\text{Eq. 23})$$

We now need an expression for the efficiency loss of the drive as a function of the fractional phase difference from 90° . This can be calculated by taking the integral of work done on the resoswitch by the drive electrode over a cycle:

$$W = \int F(x) dx \quad (\text{Eq. 24})$$

Apply a change of variables:

$$x = \cos(\omega t), \quad dx = -\sin(\omega t) \omega dt$$

$$W = -\omega \int_0^\pi \sin(\omega_0 t) \sin(\omega t) dt \quad (\text{Eq. 25})$$

The resulting integral can be evaluated numerically. For $\Delta\omega = 0$ corresponding to zero phase shift, the drive efficiency is 1. As the phase shift increases and $\Delta\omega$ is greater than 1, drive efficiency decreases.

The resoswitch makes a one-to-zero bit error if the resoswitch stops making contact, i.e. if the contact depth becomes zero. This occurs if the drive efficiency falls below a critical threshold of:

$$\alpha = \frac{kg^2}{k_c x_d^2 + k(x_d + g)^2} \quad (\text{Eq. 26})$$

For the resoswitch above, $\Delta\omega = 0.631$ and $\alpha = 0.62$. Assuming $d = 0.05$, then it takes only 165 μs of impacting (about 4 cycles at 23 kHz) before the resoswitch starts to squeg.

F. Frequency Mask

To gauge the degree to which this mechanical receiver selects the desired input and rejects blockers, it is instructive to consider phenomena that influence the frequency mask for this receiver. Given that impacting registers input detection, the most appropriate frequency mask for this all-mechanical receiver plots the minimum power required to instigate impacting versus frequency.

The displacement of the shuttle impactor is given as:

$$\frac{x(s)}{F(s)} = \frac{1}{k_r} \cdot \frac{\omega_0^2}{s^2 + s\omega_0/Q + \omega_0^2} \quad (\text{Eq. 27})$$

Where k_r is the dynamic stiffness of the resoswitch at the shuttle location, ω_0 is the resonance frequency of the resoswitch, $x(s)$ represents the displacement of the resoswitch shuttle in frequency domain, and $F(s)$ is the force applied on the shuttle, which takes the form

$$F(s) = L\{F(t)\} = L\left\{\frac{\epsilon h}{2g_f} [V_P^2 - 2V_P v_{in} \cos(\omega t) + v_{in}^2 \cos^2(\omega t)]\right\} \quad (\text{Eq. 28})$$

Where V_P is the dc-bias voltage, h is the thickness of the resonator structure, g_f is the resonator finger spacing, and $v_{in} \cos(\omega t)$ is the input ac voltage at frequency ω . With a fixed V_P , the minimum input ac voltage, or the minimum input power required for the shuttle to instigate reliable impacting, and thus produce an output, varies with respect to input frequencies.

Fig. 2.5 plots the calculated minimum input power at different frequencies required for impacting for device in design C with 25V dc-bias.

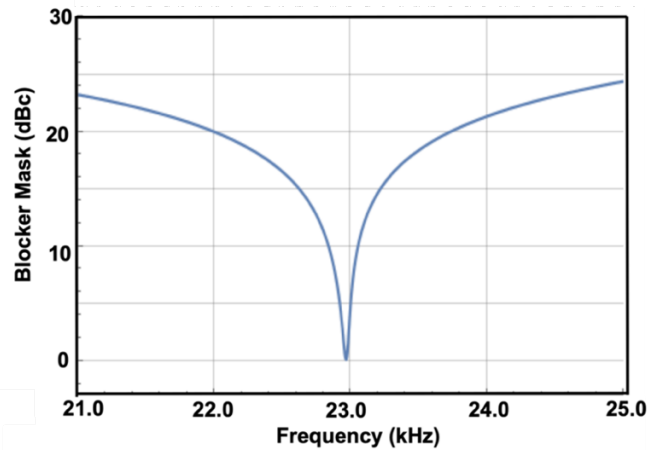


Fig. 2.5: Frequency mask of the device in design C (Table II) with V_P 25V.

2.2.2 Example Resoswitch Receiver Designs

Armed with the design formulations of Section 2.2.1, Table II summarizes resoswitch receiver designs representing what is achievable for different minimum feature sizes: 1 μm , 500 nm, and a combination of 1 μm general features with a 500 nm impact gap. To provide a practical backdrop, each design attempts to address a long-distance wireless application using a 20 kHz carrier and a ferrite core receive antenna with a tuned impedance of 31 k Ω .

Table II: Example Resoswitch Designs

		Parameter	Source	Feature Size			unit
				Design A	Design B	Design C	
				1- μm	250-nm	1- μm w/ 500-nm Gap	
Designed/Fabricated/Given	1	Resonator Shuttle, L_s	layout	160	122	160	μm
	2	Resonator Shuttle Width, W_s	layout	15	10	15	μm
	3	Resonator Truss Length, L_t	layout	10	10	10	μm
	4	Resonator Truss Width, W_t	layout	5	4	5	μm
	5	Resonator Beam Length, L_b	layout	60	80	60	μm
	6	Resonator Beam Width, W_b	layout	1.5	0.6	1.5	μm
	7	Resonator Finger Length, L_f	layout	10	10	10	μm
	8	Resonator Finger Width, W_f	layout	1	0.25	1	μm
	9	Resonator Finger Spacing, g_f	layout	1	0.25	1	μm
	10	Impactor-to-electrode gap, g	layout	1	0.25	0.5	μm
	11	Gold Film Thickness, h	measured	2	2	2	μm
	12	Finger Number Per Side, N	layout	38	150	38	---
	13	Structural Material	---	Gold	Poly-Si	Gold	---
	14	Young's Modulus, E	measured	79	158	79	GPa
	15	Density, ρ	measured	19300	2300	19300	kg/m^3
Measur	16	Measured Frequency, f_0	measured	23.7	21.4	23.7	kHz
	17	Measured Quality Factor, Q	measured	502	10,000	502	---
	18	V_p Used in Measurement, V_{PM}	measured	25	2	25	V
Analytically	19	Calculated Shuttle Mass, m_s	Eq. 29	2.28×10^{-10}	1.41×10^{-11}	2.28×10^{-10}	kg
	20	Calculated Truss Mass, m_t	Eq. 30	7.72×10^{-12}	3.68×10^{-13}	7.72×10^{-12}	kg
	21	Calculated Beam Mass, m_b	Eq. 31	2.78×10^{-11}	1.77×10^{-12}	2.78×10^{-11}	kg
	22	Equivalent Mass, m_r	Eq. 32	2.39×10^{-10}	1.48×10^{-11}	2.39×10^{-10}	kg
	23	Resonator Stiffness, k_r	Eq. 33	4.938	0.267	4.938	N/m
	24	Resonance Frequency, f_0	Eq. 34	22.9	21.40	22.9	kHz
	25	Motional Resistance, R_x	Eq. 35	60.39	0.0275	60.39	M Ω
	26	Sensitivity, S	Eq. 36	-58.5	-96.5	-64.5	dBm

A. 1- μm Minimum Feature Size

The 1 μm minimum feature size design of design A makes little attempt to match its motional resistance to the 31 k Ω source resistance, since its 1- μm comb-transducer gaps and relatively low Q of 500 make this very difficult. With a dc-bias voltage of 275 V, this design could achieve a 31.2 k Ω motional resistance, but this will not be a reasonable voltage in most

applications. Instead, the design uses a more tractable 25 V dc-bias voltage, which yields an R_x of 60.39 M Ω , significantly higher than the desired value. This large resistance greatly attenuates the power delivered to the resoswitch, necessitating further design optimization.

To at least capture potential device performance, rows 26 provides a performance metric for the device alone, where the input power is now assumed to be the power into the resoswitch. (When R_x is matched to the source impedance, this would be half the source power.) Here, the input sensitivity of this design is -64.5 dBm, which is sufficient for networked sensor applications that commonly required -60 dBm.

The sensitivity performance is further improved in the design B design, which increases the resonator's Q-factor to 10,000, a value commonly seen in polysilicon comb-driven folded-beam resonators. As a result, the sensitivity is enhanced to -96.5 dBm.

B. 250-nm Minimum Feature Size

In keeping with the historical theme of MEMS, scaling to smaller size permits better overall performance. Specifically, better lithography that allows smaller dimensions to attain smaller mass [28] and smaller comb-finger gaps improves not only sensitivity, but also the ability to impedance match an input source.

To illustrate, design B of Table II presents a design using a 250-nm minimum feature size. This design now easily achieves a 31 k Ω matching motional resistance using a 3.8 V dc-bias. In addition, with a 250-nm impact gap and a stiffness of 0.267 N/m significantly smaller than that of the design A design, the sensitivity improves to -96.5 dBm, which approaches the value needed for cross-continent communication, such as WWVB [29].

C. 1- μ m Minimum Feature Size with 500-nm Gap

The device of Fig. 2.2 features an impactor that tapers down to a blunt tip. This effectively reduces the overlap between the impactor edge and the edge of the adjacent electrode, making it easier to achieve a smaller gap than the 1- μ m lithographic resolution. The device demonstrated herein takes advantage of this and realizes a 500-nm impactor-to-electrode gap. Design C of Table II summarizes this design.

With the same finger spacing as the design A, this design suffers from the same inability to impedance match a 31 k Ω source impedance. However, its smaller impacting gap allows a considerably better sensitivity of -64.5 dBm.

Table II design C summarizes the design of one of the specific devices fabricated and evaluated experimentally in this thesis.

2.3 Gold-Electroplated Comb-Driven Resoswitches

For this study, gold was selected as the structural material for the resoswitches instead of poly-Si or nickel, as investigated in prior work by Ruonan [16]. Gold offers several advantages over these materials, making it particularly suitable for the demands of resoswitch operation:

1) *Low Resistivity for Reduced Contact Resistance*

Gold has a resistivity of $2.44 \times 10^{-8} \Omega \cdot \text{m}$, significantly lower than that of nickel ($6.99 \times 10^{-8} \Omega \cdot \text{m}$) and much lower than that of poly-Si. This lower resistivity reduces the contact resistance at the interfaces during operation, enabling faster charge transfer to the output circuit. This property is crucial for achieving efficient and reliable signal transmission in resoswitch-based systems.

2) *Resistance to Oxidation for Enhanced Durability*

Resoswitches operate by the mechanical impact between shuttle impactors and output electrodes to transfer charge (hot switching). The enormous current density at the impact points can cause other metals to oxidize easily, rendering the impacted areas non-conductive and leading to device failure. Gold, by contrast, is highly resistant to oxidation, maintaining its conductivity even under such conditions. This property ensures the long-term reliability and durability of resoswitches, especially in harsh or energy-sensitive environments.

3) *Compatibility with Electroplating for Efficient Fabrication*

Gold can be deposited using electroplating, which offers significant advantages over other deposition methods such as sputtering or e-beam evaporation. Electroplating is cost-effective, scalable, and fast, making it well-suited for the fabrication of micromechanical structures. Additionally, electroplated gold typically exhibits lower residual stress and stress gradients compared to films deposited via physical vapor deposition (PVD) techniques.

While gold offers several advantages as a structural material for resoswitches, it also presents some notable disadvantages compared to poly-Si. These trade-offs must be carefully considered when optimizing device performance for specific applications:

1) *Mechanical Softness and Deformation*

Gold is notoriously soft, which can pose challenges during the operation of resoswitches. The repeated impacts between the shuttle's impactors and the output electrodes, essential for charge transfer, can cause deformation of the gold impactors over time. This deformation could eventually lead to device failure, such as an inability to establish contact during subsequent impacts. The mechanical softness of gold could limit its long-term durability under high-stress operational conditions.

2) *Lower Quality Factor (Q)*

The quality factor (Q) of gold resonators is typically much lower than that of poly-Si. While poly-Si devices can achieve Q values on the order of 10,000, gold resonators usually exhibit Q values in the range of a few hundred. This lower Q impacts the sensitivity of the resoswitches, as high sensitivity requires a higher Q . For applications where sensitivity is crucial, the limitations of gold in this regard may necessitate additional design considerations or trade-offs.

Despite these challenges, the use of electroplated gold remains attractive for its superior electrical conductivity, oxidation resistance, and compatibility with cost-effective fabrication techniques. This section provides a detailed examination of the development and testing of resoswitches utilizing electroplated gold, shedding light on the material's strengths and weaknesses. Through this analysis, the dissertation seeks to provide a comprehensive understanding of the implications of material choice on the functionality, reliability, and application scope of resoswitches.

2.3.1 Fabrication Process: Electroplating Mold

The fabrication process for gold comb-driven resoswitches involves addressing several critical challenges to achieve reliable device performance. These challenges include designing and developing the electroplating mold, selecting appropriate seed layer and protection layer, and optimizing the electroplating recipe.

Gold electroplating is typically performed on a gold seed layer, with alternatives such as nickel (Ni) or chromium (Cr) also considered. Previous studies have identified gold as the optimal seed layer [16] with a Cr layer underneath it to enhance adhesion to the substrate. However, the removal of the seed layer after electroplating involves a short dip in a wet etchant, which can erode the electroplated structures. To mitigate this issue, the gold seed layer must be extremely thin, often only a few nanometers. A protective layer is also applied over the seed layer to shield it from damage during the development of the electroplating mold, and the choice of this protective layer is closely tied to the type of mold material used.

Three materials were investigated as candidates for the electroplating mold in the fabrication process: developed photoresist, silicon dioxide (SiO_2), and amorphous silicon (a-Si). To achieve a 1 μm -thick electroplated microstructure, the mold must be between 1.5 μm and 2 μm thick. The most challenging aspect of the resoswitch design (design C in Table II) involves achieving a minimum feature size of 500 nm between the shuttle impactor and output electrodes, as well as 1 μm spacing between comb fingers. The suitability of electroplating molds made from all three materials was evaluated to ensure they meet these stringent design requirements.

A. SiO_2 Electroplating Mold

Plasma Enhanced Chemical Vapor Deposition (PECVD) silicon dioxide (SiO_2) can be utilized as a mold material for the fabrication of resoswitches. A 2 μm -thick SiO_2 mold can achieve etch profiles with resolutions down to 500 nm, making it a promising option. In this approach, SiO_2 is deposited over the metal seed layer. However, the deposition of SiO_2 over a gold seed layer imposes limitations on the thermal budget of the deposition process. To address this, low-temperature PECVD oxide deposition at 300°C is employed.

The mold's etch profile is defined using Reactive Ion Etching (RIE), and the specific etching recipe is detailed in Appendix A. To protect the underlying gold seed layer during the oxide etching process, alumina (Al_2O_3) is selected as the protective layer. Al_2O_3 is resistant to the oxide etching and can be deposited via sputtering, ensuring minimal interaction with the etch chemistry. The designed process flow is shown in Fig. 2.6.

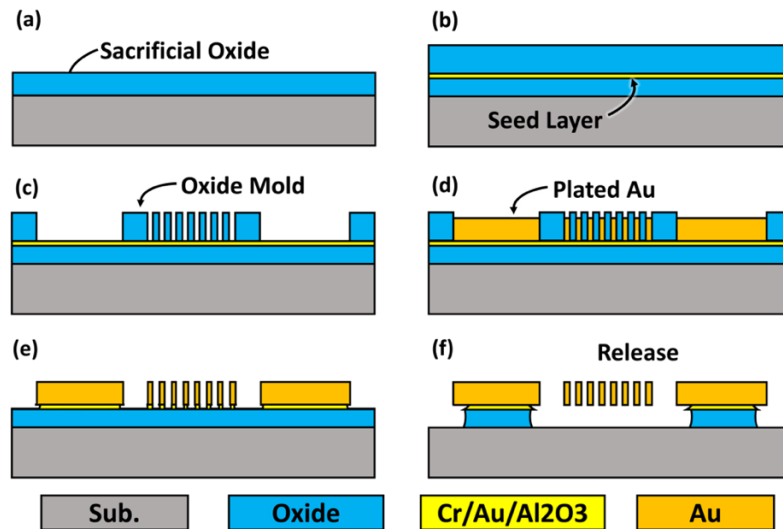


Fig. 2.6: Process flow of electroplated gold resoswitch using oxide mold.

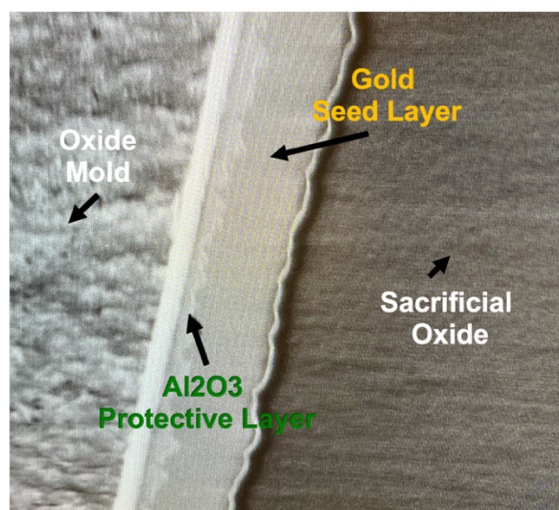


Fig. 2.7: SEM image showing that the Al_2O_3 protective layer and the gold seed layer, which is critical for future electroplating, have been completely etched away in large open areas during the oxide mold etching process. This issue must be resolved to successfully fabricate functional electroplated devices.

However, several challenges arise during the oxide mold etching process. The etching rate of SiO_2 varies depending on feature size: larger features are etched more rapidly than smaller ones, which is attributed to the difficulty ions face when accessing narrower areas. This discrepancy can cause issues during electroplating. As shown in the SEM image in Fig. 2.7, the protective layer above the gold seed layer is completely etched away in large open areas, exposing and removing the seed layer in those regions. This results in un-electroplated areas. On the other hand, if the oxide etch time is reduced to preserve the seed layer in larger features, the oxide in smaller features may not be fully removed, preventing proper electroplating in those areas, as shown in Fig. 2.8.

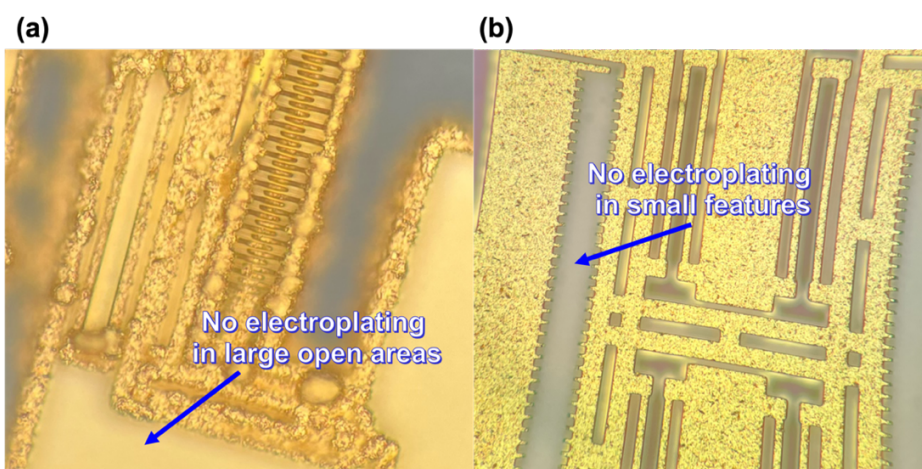


Fig. 2.8: (a) Larger features are etched at a faster rate than smaller ones. Prolonged oxide mold etching can remove both the protective layer and the gold seed layer in large features, resulting in non-electroplatable areas. (b) Shortening the oxide mold etch time helps preserve the seed layer in large open areas but may leave oxide residue in smaller features, preventing electroplating in subsequent steps.

To mitigate this issue, one potential solution is to increase the thickness of the protective Al_2O_3 layer. However, this introduces a trade-off: a thicker protective layer reduces the resolution of the device by increasing the finger spacing. This occurs because the removal of the protective layer involves isotropic wet etching, which can erode the edges of fine features. Balancing the protective layer thickness with the desired resolution is thus critical for optimizing the fabrication process.

B. a-Si Electroplating Mold

Plasma-Enhanced Chemical Vapor Deposition (PECVD) amorphous silicon (a-Si) is another potential material for use as an electroplating mold. In this approach, the protective layer can be either SiO_2 or alumina, depending on the process requirements. However, during the development and evaluation of this technique, several issues were identified.

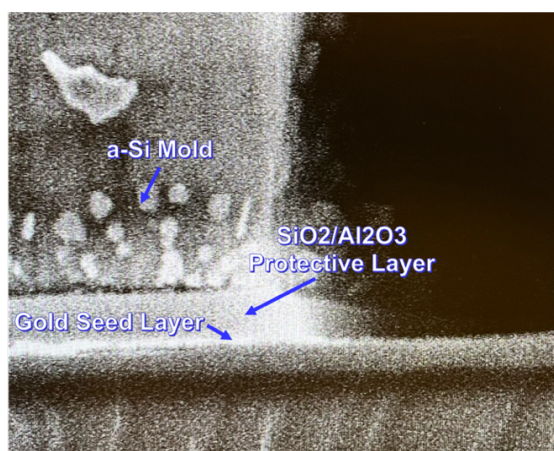


Fig. 2.9: A similar issue arises with the a-Si mold, where the etch rate is higher in large open areas. This results in the removal of the protective layer and the underlying seed layer, leading to unintended non-electroplated regions.

One major challenge is the difference in etch rates using RIE between small and large features, a problem similar to that encountered with SiO_2 molds. This disparity results in non-uniform electroplating outcomes, with the electroplated structures exhibiting similar deficiencies to those observed in SiO_2 mold-based molds, as shown in Fig. 2.9.

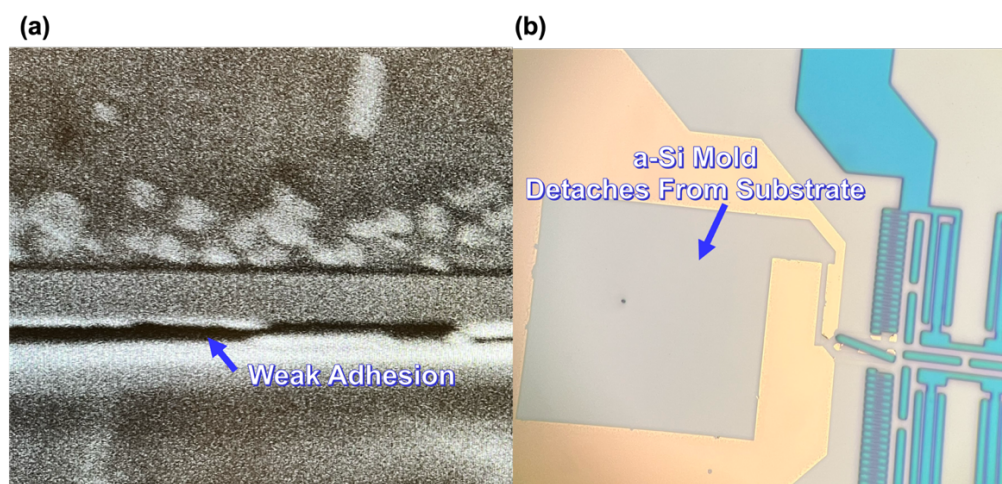


Fig. 2.10: Poor adhesion between the SiO_2 protective layer, gold seed layer, and the substrate results in the delamination of the a-Si mold from the substrate, rendering it unsuitable for the subsequent electroplating step.

When SiO_2 is used as the protective layer, a significant problem arises with its adhesion to the gold seed layer. Poor adhesion can cause the oxide mold to peel off the substrate during processing, as illustrated in Fig. 2.10. This peeling not only disrupts the mold's integrity but also compromises the subsequent electroplating process, leading to defective structures.

Additionally, the cleanliness of the deposited a-Si film presents another challenge. As the thickness of the a-Si layer increases, as shown in Fig. 2.11, the deposited film appears blurry and contains debris-like inclusions, which degrade the quality and reliability of the mold.



Fig. 2.11: The deposited a-Si film appears blurry and contains debris-like inclusions, highlighting cleanliness issues with the a-Si mold that need to be addressed.

C. Developed Photoresist

The traditional electroplating process utilizes developed photoresist as the mold material. When using photoresist, the protective layer can be chromium (Cr), the same material used as the adhesion layer beneath the gold seed layer to the substrate. The process flow is illustrated in Fig. 2.12. A 2.5 μm -thick photoresist layer (UV26_3.0-2.5 μm) is applied, exposed with an energy of 38 mJ using ASML, and developed to form the electroplating mold. This process successfully produces interdigitated comb fingers with 1 μm spacing and a 500 nm gap between the impactor and output electrode, as seen in Fig. 2.13.

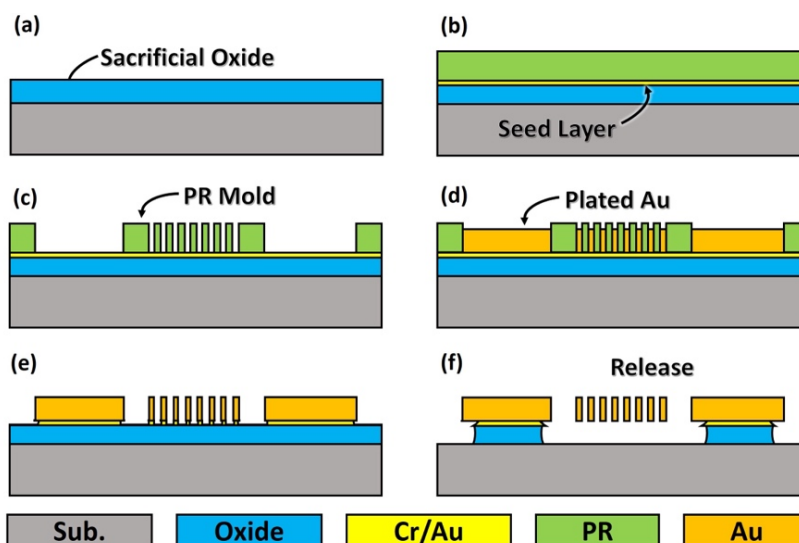


Fig. 2.12: Process flow of the gold electroplated resoswitch with photoresist mold.

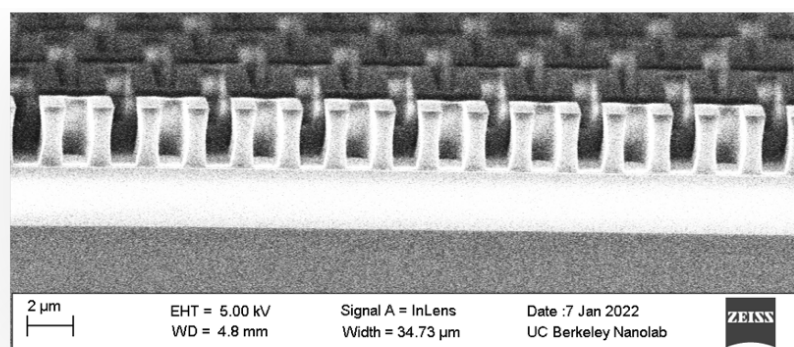


Fig. 2.13: SEM image of the interdigitated comb fingers of a resoswitch, demonstrating that the PR mold successfully achieves a finger spacing of 1 μm .

After forming the mold, the die undergoes a short dip in Cr-7 etchant to expose the seed layer, preparing it for gold electroplating using the recipe detailed in Section 2.3.2. Following electroplating, the devices are released through a series of steps: photoresist stripping, sequential dips in Cr-7 etchant, Au etchant, and another Cr-7 etchant. The final step involves a timed etch of the sacrificial oxide using either wet HF or vapor-phase HF. The completed devices are depicted in Fig. 2.14.

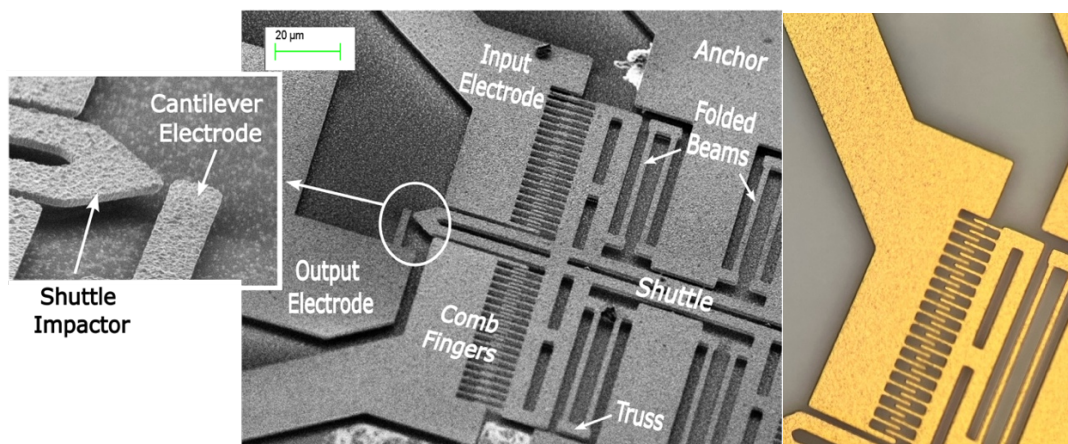


Fig. 2.14: SEM and optical microscope images showing the fully fabricated resoswitch devices.

2.3.2 Fabrication Process: Electroplating Recipe

The gold electroplating solution used in this work is Elevate 7934, a cyanide-based solution supplied with separate concentration and electrolyte components. The vendor recommends a plating solution temperature between 45°C and 55°C and an electrolyte-to-concentration ratio of 4:1. The suggested current density range is between 1 mA/cm² and 10 mA/cm².

Given the broad recommended ranges for temperature and current density, experimental optimization was required to identify the optimal operating conditions. A series of trials were conducted to determine the ideal temperature and current density for achieving uniform deposition with minimal surface roughness and optimal film properties.

The steps for setting up the electroplating station and performing the process are outlined below:

1. *Prepare Tools:* Clean all beakers, tweezers, anode, and cathode thoroughly.
2. *Prepare the Solution:* Fill a 200 mL beaker with sufficient Elevate Gold 7934 to fully submerge the sample.
3. *Heat the Solution:* Place the beaker with the solution in a water bath on a hotplate, setting it to the desired temperature. Monitor the temperature using a probe thermometer.
4. *Prepare the Anode:* Use a platinized titanium anode for the electroplating process.
5. *Attach the Sample:* Secure the sample using a binder clip, ensuring good electrical contact with the gold seed layer.
6. *Submerge Electrodes:* Immerse both the cathode (sample) and anode into the solution.
7. *Position Electrodes:* Suspend the sample from a Teflon threaded rod and place it parallel to the anode in the beaker, ensuring proper orientation for plating.
8. *Connect Circuitry:* Attach alligator clips to the anode and cathode for electrical connections.
9. *Apply Current:* Determine the plating current based on the exposed seed layer area. Note that higher currents lead to faster deposition rates but may also increase surface roughness and film stress.



Fig. 2.15: All fixtures are custom-designed and fabricated from Teflon. The setup enables precise control of electroplating parameters, including the spacing between the cathode and anode, the depth of the sample in the plating solution, plating uniformity across samples or wafers, and other critical factors.

The experimental electroplating setup used for device fabrication is shown in Fig. 2.15. Several trials were conducted across varying temperatures and current densities, using developed photoresist as the electroplating mold, as illustrated in Fig. 2.16. Based on the results, the optimal plating conditions were identified as a temperature of 50°C and a current density of 1.5 mA/cm^2 , yielding high-quality deposition with uniform surface morphology.

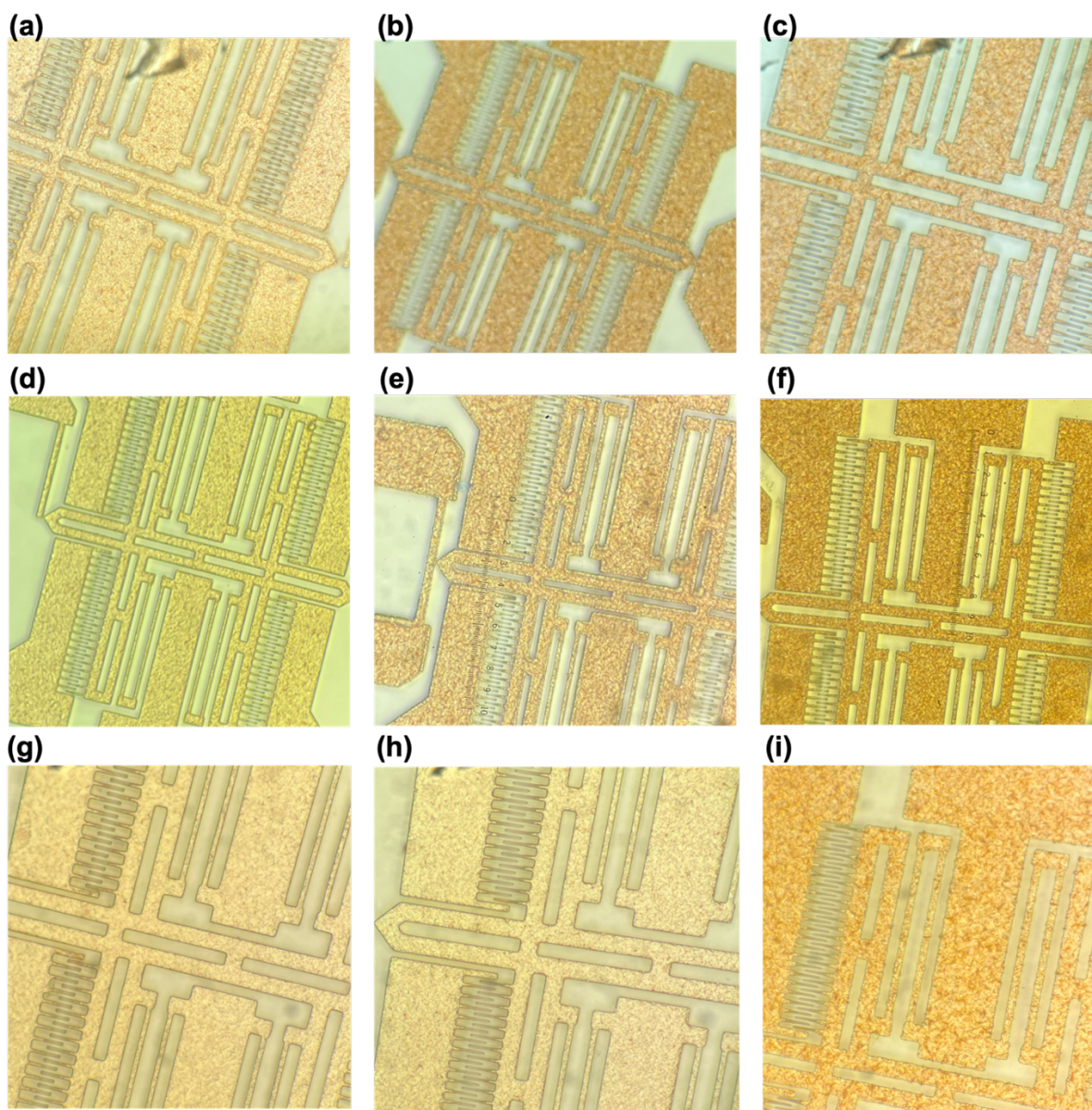


Fig. 2.16: Electroplating results using the PR mold under varying temperature and current conditions:

- (a) Temperature: 50°C, Current: 1 mA;
- (b) Temperature: 50°C, Current: 1.2 mA;
- (c) Temperature: 50°C, Current: 1.6 mA;
- (d) Temperature: 55°C, Current: 1 mA;
- (e) Temperature: 50°C, Current: 1.4 mA;
- (f) Temperature: 50°C, Current: 1.8 mA;
- (g) Temperature: 60°C, Current: 1 mA;
- (h) Temperature: 60°C, Current: 1.4 mA;
- (i) Temperature: 60°C, Current: 1.8 mA.

2.3.3 Experimental Results

The resowitch receivers studied in this thesis were fabricated using developed photoresist molds and evaluated using a Lakeshore FWPX vacuum probe station. This probe station provides an 800- μ Torr vacuum environment and includes feedthrough connections to external measurement instruments. For testing, a DC power supply was employed to deliver required DC voltages such as V_P and V_{DD} .

A Tektronix AFG3102 Arbitrary Function Generator was used to modulate a resonance carrier into on-off keying (OOK) waveforms, which served as the input signals for performance evaluation of the resowitch receivers. The complete experimental setup is illustrated in Fig. 2.17.

Prior to measuring the resowitch's performance as a communication receiver, the devices were characterized using the setup shown in Fig. 2.18, allowing determination of their resonance frequencies and corresponding quality factors (Q). These preliminary evaluations provided a baseline for understanding the dynamic behavior of the devices under test.

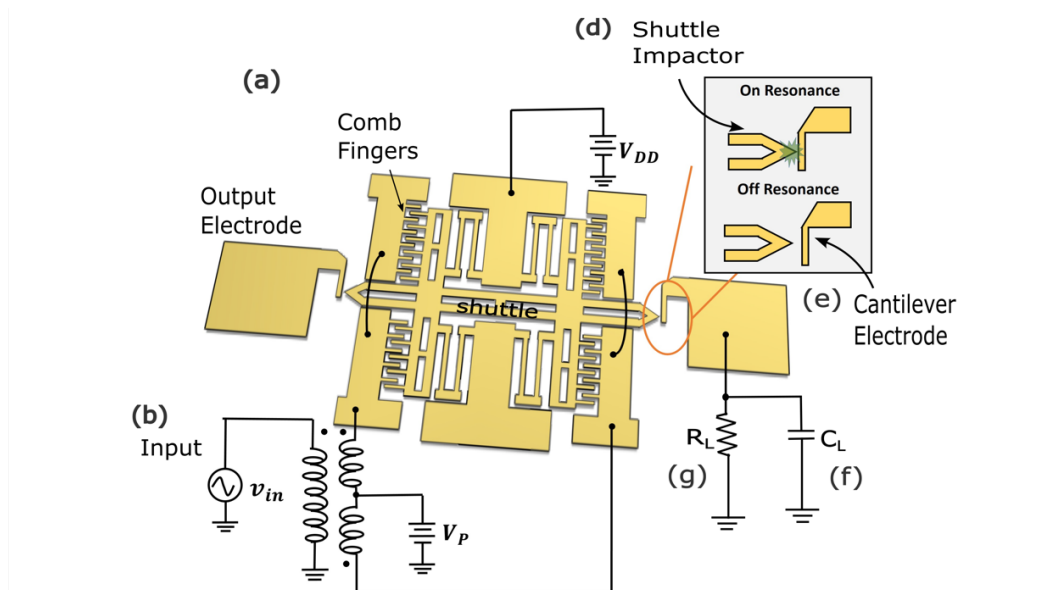


Fig. 2.17: Experimental setup of the resowitch receiver.

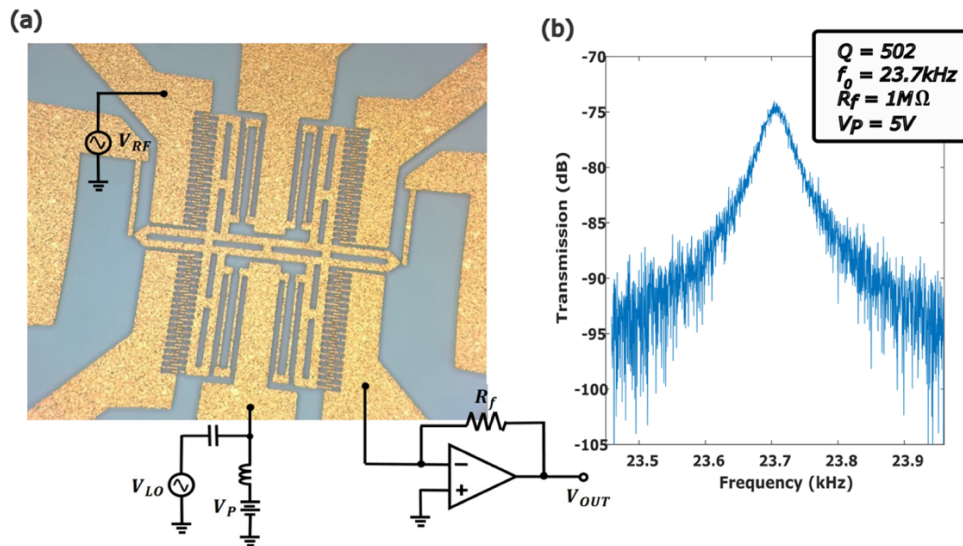


Fig. 2.18: (a) Mixing measurement setup and applied bias and local oscillator voltages to null parasitic feedthrough en route to obtaining the (b) transmission spectrum of the gold resoswitch, showing a resonance frequency of 23.7 kHz and a Q of 502.

Two types of OOK-modulated signals, Amplitude-Shift Keying (ASK) and Frequency-Shift Keying (FSK), were applied to the resoswitches using the experimental setup. In ASK modulation, a bit "1" is represented by a sinusoidal signal at the resonance frequency with an amplitude of v_{in} , while a bit "0" is represented by the absence of a signal (0), as illustrated in Fig. 2.19(a). For FSK modulation, a bit "1" is represented by a sinusoidal signal at the resonance frequency with an amplitude of v_{in} , and a bit "0" is represented by a sinusoidal signal of the same amplitude but at a non-resonance frequency. The corresponding measured output waveforms are shown in Fig. 2.19(b).

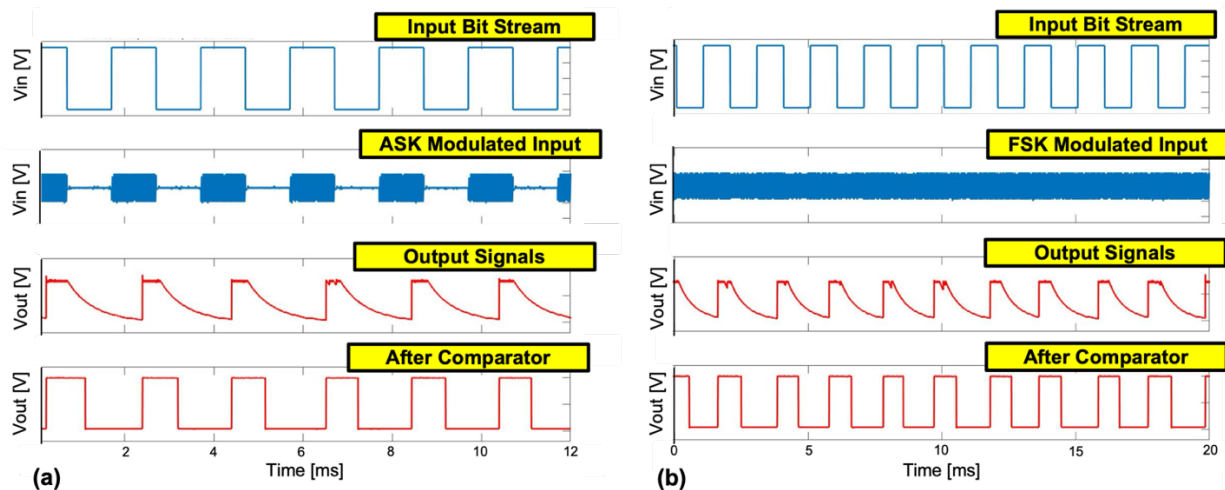


Fig. 2.19: (a) Measured output signal and its corresponding waveform after processing through a comparator circuit, with the threshold set to half of the maximum output signal, for an ASK-modulated input bit stream. (b) Measured output signal and its corresponding waveform after processing through a comparator circuit, with the threshold set to half of the maximum output signal, for an FSK-modulated input bit stream.

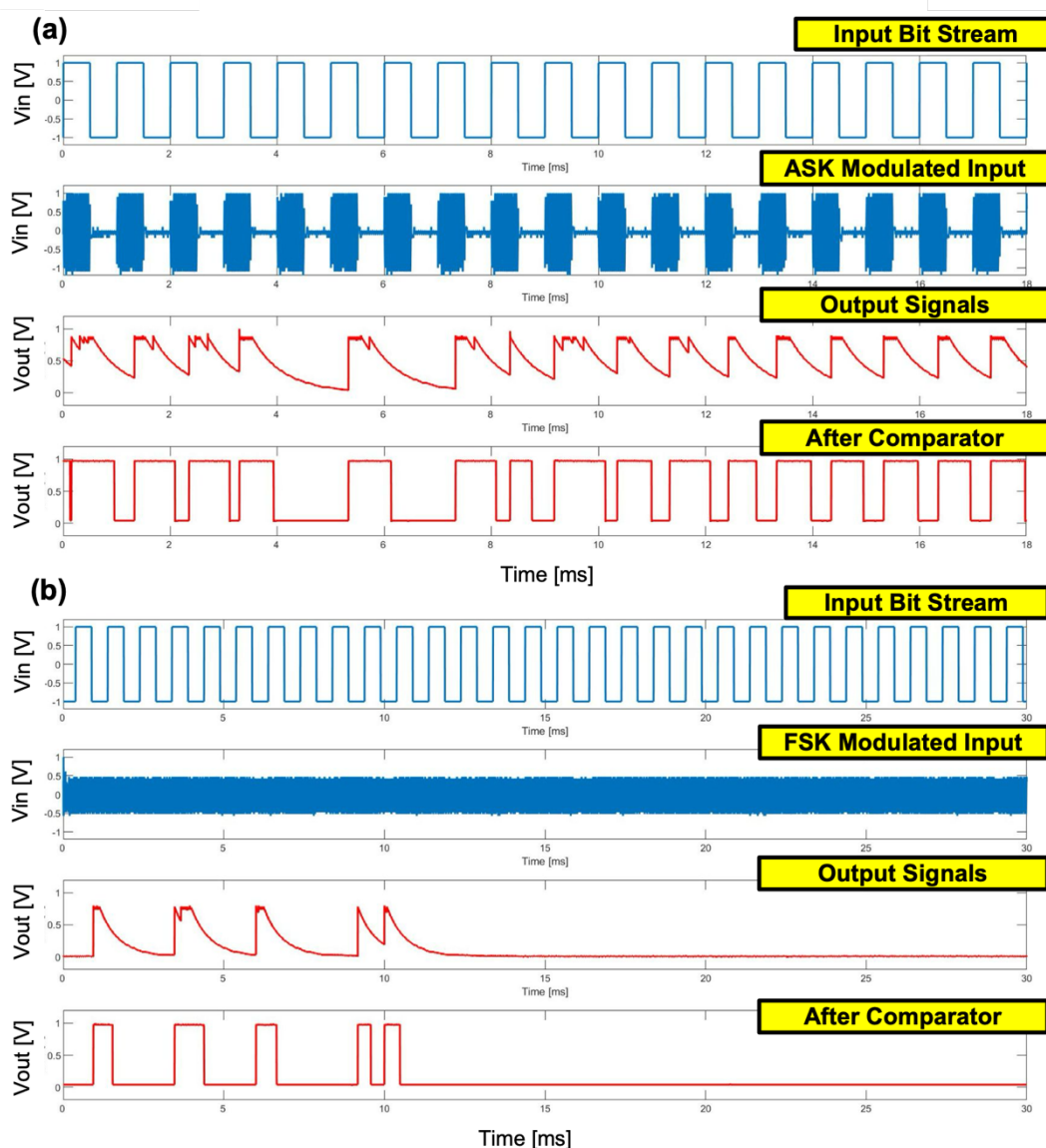


Fig. 2.20: Measured output signals for (a) ASK-modulated input signals and (b) FSK-modulated input signals. In both cases, frequency instability caused by the phenomenon known as 'squegging' was observed, leading to bit errors in the output. This instability highlights the challenges in maintaining consistent signal integrity during demodulation, particularly when operating under certain input conditions or device configurations.

These modulated signals were input to the resoswitches, and the corresponding outputs at the output electrodes were measured. The resoswitches fabricated using developed photoresist molds successfully received and demodulated the input signals, producing outputs that mimic the input bit streams. This confirmed the capability of resoswitches to function as communication receivers.

However, some undesired outputs with incorrect output frequencies were observed during the measurements. This phenomenon, known as "squegging," is illustrated in Fig. 2.20. It presents a significant challenge to achieving reliable demodulation and requires further

investigation to identify strategies to mitigate or eliminate it. The underlying causes and potential solutions for this issue are discussed in detail in Chapter 5 of this thesis.

2.4 Ruthenium-Electroplated Comb-Driven Resoswitches

Ruthenium (Ru) is considered a superior material compared to gold for resoswitch applications for several key reasons:

- 1) *Hardness and Durability*: Ru is a harder material with a higher Young's modulus than gold. This increased hardness reduces the likelihood of deformation at the impactor tips after repeated impacts, significantly enhancing the lifetime and reliability of resoswitches.
- 2) *High Quality Factor (Q)*: Ru has demonstrated the ability to achieve a significantly higher Q factor compared to gold. For example, a Q factor of up to 50,000 at 11.7 MHz has been reported in a CC-beam resonator under applied tensile stress [30]. This higher Q factor improves the sensitivity of resoswitches, making Ru particularly suitable for high-sensitivity applications.
- 3) *Oxidation Resistance and Conductivity*: While gold is highly resistant to oxidation, it is not completely immune, and any oxidation could compromise the functionality of resoswitches by making them non-conductive. In contrast, Ru forms a conductive oxide layer when oxidized. This property ensures that even if Ru oxidizes, the resoswitch remains functional, thereby enhancing its reliability and extending its operational lifetime.
- 4) *Cost-Effective Deposition*: Ru can be deposited using electroplating, a technique that is not only more cost-effective than methods like sputtering or evaporation but also much faster. The ability to electroplate Ru makes it a highly practical choice for resoswitch fabrication.

2.4.1 Fabrication Process: Ru Electroplating

The Ruthenium (Ru) electroplating process utilizes a solution consisting of RUTHUNA 479 Black Initial Concentrate and deionized water, mixed in a 1:4 ratio. A gold seed layer serves as the foundation for Ru electroplating. The steps below outline the process, including setup and operation:

1. *Electrolyte Preparation*
 - Prepare the electroplating solution by combining the RUTHUNA 479 concentrate with deionized water in a 1:4 ratio. Mix thoroughly to ensure uniformity.
2. *Temperature Setup*
 - a. Place the beaker containing the solution in a water bath on a hotplate.
 - b. Set the bath to the desired temperature (initially 65 °C as per vendor recommendations).

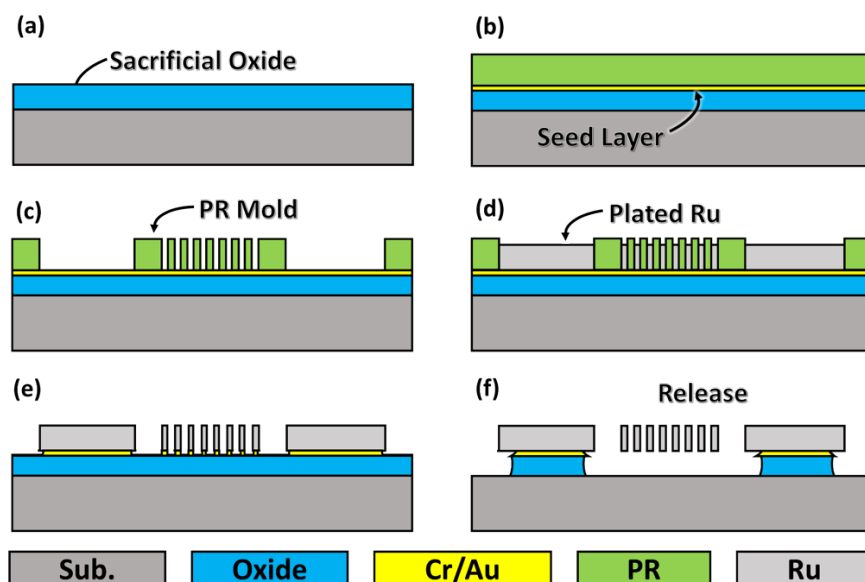


Fig. 2.21: Process flow of Ru-electroplated resoswitch with PR mold.

The Ru electroplating was performed using the procedures detailed in Section 2.4.1. However, significant challenges were encountered during the process. One major limitation was the maximum thickness of Ru that could be electroplated. The structures typically cracked when the thickness reached 250 nm, as illustrated in Fig. 2.22. Attempts to mitigate these failures by varying the plating temperature and current density were unsuccessful, and the maximum stable thickness could not exceed 300 nm.

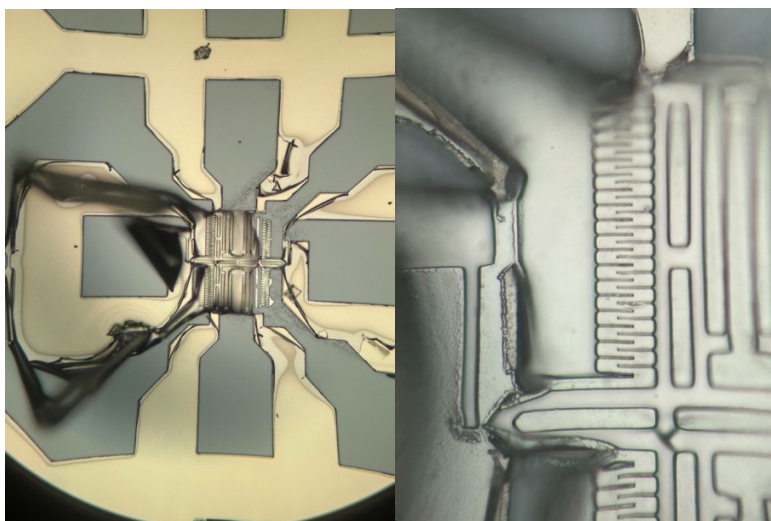


Fig. 2.22: Optical microscopic images showing electroplated Ru structures develop cracks when the thickness exceeds 250 nm.

Additionally, issues arose during the release process. The developed photoresist mold could not be effectively removed, as the Ru electroplating caused crosslinking with the photoresist. This crosslinking rendered the mold removal impossible, leading to non-functional

devices. Consequently, a change in mold material is necessary, with oxide molds emerging as a potential alternative.

B. Silicon Dioxide Mold

For Ruthenium (Ru) electroplating, a protective layer is necessary to shield the gold seed layer during the etching of the oxide mold, which involves either wet HF etching or reactive ion etching (RIE) of the oxide. Both nickel (Ni) and chromium (Cr) are resistant to wet HF etching, and Ni can withstand most oxide RIE etch recipes [31]. Since the oxide mold profile is defined using RIE, Ni is chosen as the protective layer. However, due to poor adhesion between Ni and oxide, an additional adhesion layer, such as Cr, is preferred. The process flow is illustrated in Fig. 2.23.

Despite employing the oxide mold, achieving a Ru film thicker than 300 nm remains unsuccessful. For comb-driven resoswitches to function effectively, the structural thickness must be thick. If the structure is too thin, vertical resonance dominates over lateral resonance, which is crucial for proper operation of the resoswitch.

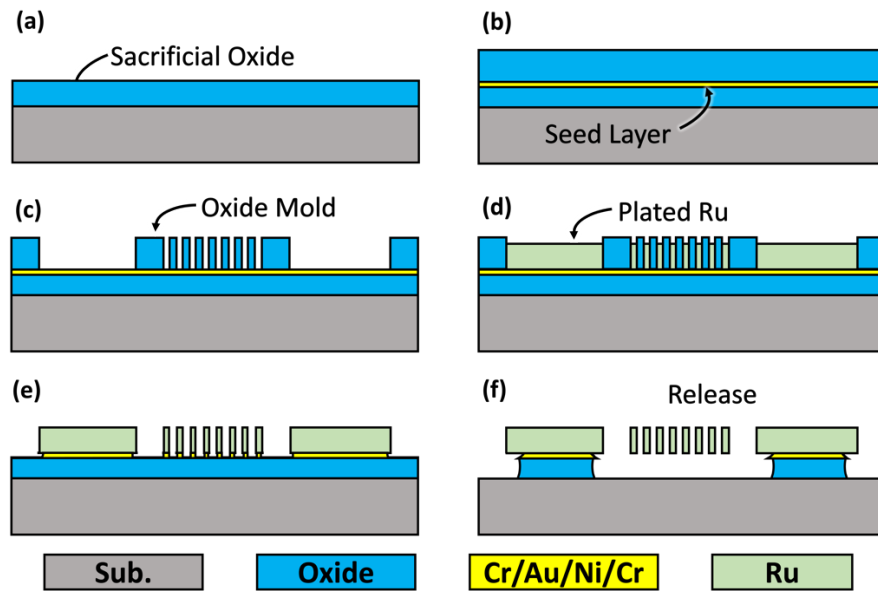


Fig. 2.23: Process flow of Ru-electroplated Resoswitch with oxide mold.

Chapter 3

Bit Rate-Adapting Resoswitches

Micromechanical resonant switches, a.k.a., resoswitches, that transfer charge from pole to throw by impacting a conductive resonant vibrating structure against a conductive receive electrode have numerous advantages over their conventional non-resonant counterparts [12]. Specifically, because they harness resonance dynamics, they require considerably smaller actuation power than non-resonant switches, making possible reception of tiny wireless signals. In addition, amplification of displacements at resonance permits the use of geometries with substantially higher restoring stiffnesses than conventional MEMS switches, contributing to much better reliability [12]. Furthermore, the use of impulsive contact forces makes possible very small instantaneous contact resistance [21] and tiny contact times, both of which contribute to fast charging speed and additional reliability enhancements. Finally, because they operate at resonance, they provide a built-in selectivity needed for multiplexed communications.

Indeed, switch characteristics like these have made possible the first all-mechanical communication receiver (*cf.* Fig. 3.1) capable of receiving and demodulating very-low-frequency (VLF) FSK-modulated signals at 1 kbps with -60 dBm sensitivity, all while consuming zero standby power when merely listening [17]. The ability to listen continuously without consuming power makes this all-mechanical receiver especially attractive for applications that only require infrequent data reception, but must be attentive for long periods, e.g., years, such as desirable to track clothing in the recently exploding rented fashion industry. Here, a passive receiver attached to clothing that can listen for decades, draining its power supply only on the rare reception of new data—perhaps transmitted across continent at VLF [32]—could be quite enabling for many similar industries.

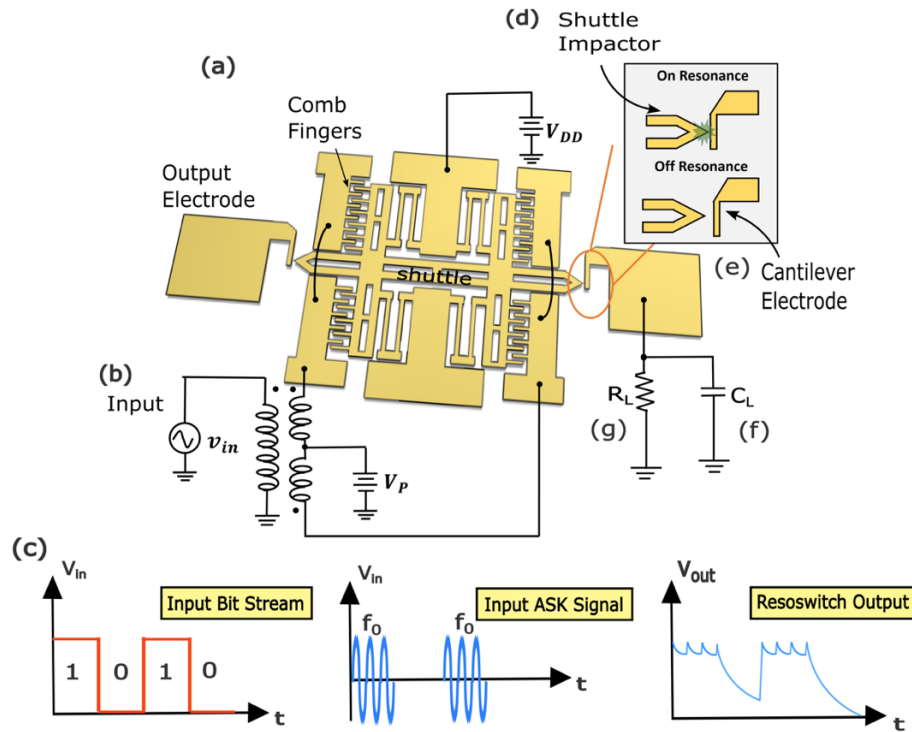


Fig. 3.1: All-mechanical communication receiver employing (a) an all-gold micromechanical reswitch to accept at its (b) input a (c) ASK-modulated resonance carrier with marks and spaces. The reswitch responds to mark periods, i.e., when the resonance sinusoid appears, by vibrating at resonance to impact its (d) shuttle impactor against (e) a conductive cantilever output electrode, connecting the cantilever to V_{DD} , hence charging the (f) output load capacitance C_L to V_{DD} and registering an output high or '1'. When receiving a space input, i.e., no sinusoid, the reswitch does not move, allowing (g) bleed resistor R_L to discharge the load to an output low, or '0'. In the end, the output bit stream matches the input modulating bit stream, meaning that the bits have been successfully communicated.

While compelling, the use of high Q resonance to enable sensing of tiny wireless signals generates skepticism regarding the ultimate bit rate of this receiver. Indeed, since the number of oscillations needed for a reswitch to reach an amplitude exceeding its impact switch threshold goes as the device Q , one would expect switching time to increase with increasing Q , which then reduces the bit rate. In essence, one expects a trade-off between sensitivity (which improves with increasing Q) and bit rate (which slows as Q increases).

This section of the thesis demonstrates how design and operation of a reswitch to strategically harness the energy storage nature of the device can break this supposed trade-off, allowing the reswitch to switch faster to accommodate a higher bit rate, i.e., to adapt to the desired bit rate. Here, the right device design and input modulation density that maintain a reswitch in a pre-energized state have lowered the measured response time of the device from 1.58 ms to 0.048 ms, which is 32 times faster than the theoretical expectation based on the device Q of 502. This 32x reduction in response time then permits a bit rate as high as 20 kbps, which is 20 times faster than demonstrated in [13]. A data rate this fast now opens this device to a much wider swath of applications that might soon include things like cross-continent firmware updates from a central location.

3.1 Device Structure and Operation

Fig. 3.2 presents the all-gold resoswitch used in this work, comprising a 1- μm -thick movable shuttle suspended 2.5- μm above the substrate by folded-beam flexures that themselves anchor to central locations. Comb fingers on opposite sides of the shuttle interdigitate with comb fingers from anchored gold electrodes to form classic comb-drive transducers capable of electrostatically driving the shuttle to amplitudes on the order of the finger lengths [16]. The typical drive scheme employs the combination of a dc-bias ($V_P - V_{DD}$) and ac signal input v_i across the finger gaps that generates a force proportional to their product $(V_P - V_{DD}) \cdot v_i$ acting at the frequency of v_i . Fig. 3.1 specifically shows the hookup needed to operate the resoswitch as a communication receiver, where the ac voltage enters through a bias tee atop the large V_P .

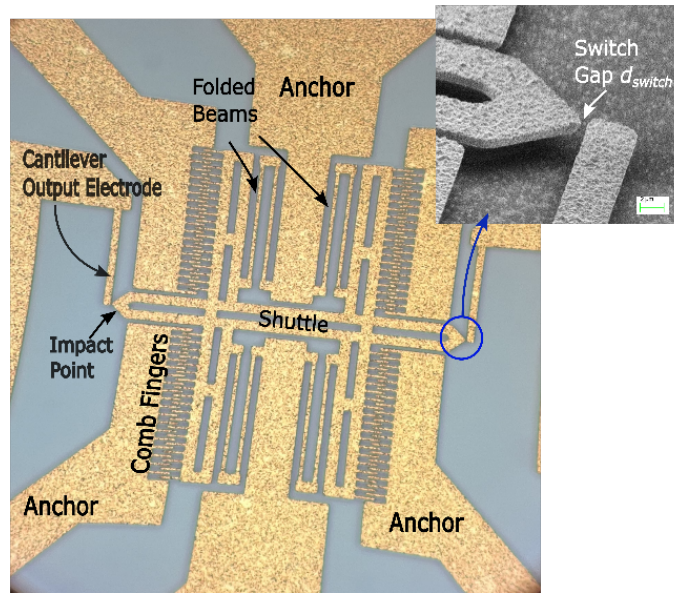


Fig. 3.2: Microscope photograph of a fabricated resoswitch with labels to identify important parts. This resoswitch features gold cantilever electrodes designed to soften impacts to reduce squegging, which occurs when hard impacts de-phase a resoswitch in a way that temporarily lowers the efficiency of the drive input, causing the device to lose amplitude and stop impacting until a return to proper phasing reinstates the drive, allowing impacting once again.

The shuttle also possesses impactor protrusions indicated in the figure. Unlike the resoswitch of [13], the Fig. 3.2 device impacts bendable cantilevers rather than hard anchored electrodes in order to soften the blow, reducing a squegging phenomenon that plagued earlier resoswitches [21]. As will be obvious later, harnessing pre-energization to raise bit rates works best when squegging is suppressed.

When the ac input signal frequency matches the mechanical resonance frequency f_o of the resoswitch, the shuttle displacement amplitude grows exponentially from rest until it is large enough to induce periodic impactor-to-cantilever contact. This contact then charges the output electrode node to V_{DD} , effectively closing the switch—an operation that fits nicely into an OOK signal reception role, as depicted in Fig. 3.1(c). Here, the gated-sinusoid input waveform realizes an ASK-modulated resonance carrier that switches the resoswitch to low

and high outputs that match the modulation, where each period of the modulation waveform contains an information bit.

3.2 Time to Impact and Maximum Bit Rate

3.2.1 Bit Rate and Sensitivity Tradeoff

A traditional filter with quality factor Q has a 3-dB bandwidth given by:

$$\omega_{BW} = \frac{\omega_0}{Q} \quad (\text{Eq. 37})$$

The time required for a resonance input force to drive the resoswitch from rest to impacting depends strongly on the device Q and is proportional to the Q/f_0 ratio. Consequently, the bit rate is inversely proportional to this Q/f_0 ratio; in other words, the bit rate is directly proportional to the 3-dB bandwidth of the filter.

At the same time, the minimum detectable input power, or sensitivity S , as defined in Eq. 38, is inversely proportional to f_0/Q , displaying an opposite dependency (since a lower sensitivity is desirable, implying we want f_0/Q to be minimized). The tradeoff between sensitivity and switching time (which sets bit rate) is clear.

$$S = \frac{2\pi d_{switch}^2 k_r f_0}{Q} \quad (\text{Eq. 38})$$

The key to breaking this trade-off and achieving simultaneous good sensitivity and high bit rate capability lies in the energy storage ability of the resoswitch's high Q . Specifically, by tapping into stored energy during non-driven periods, a resoswitch can be made to adapt to whatever bit rate appears at its input, where the faster the bit rate, the faster the reso-switching time, so the more capable to support the faster bit rate.

In the following sections, we show that pre-energizing a resoswitch decreases the time that it takes to make contact, and so expands the bit rate from that predicted by Q .

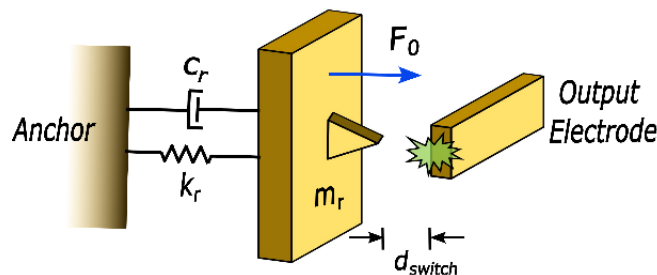


Fig. 3.3: Equivalent mass-spring-damper second order system of resoswitch. m_r , k_r and c_r represent the dynamic mass, stiffness, and mechanical damping of resoswitch.

3.2.2 Pre-Energizing Theory

Fig. 3.3 shows the second-order mass-spring-damper equivalent system of Fig. 3.1. Here m_r , k_r and c_r represent the dynamic mas, stiffness, and mechanical damping determined using equations given in [22]:

$$m_r = m_{shuttle} + \frac{1}{4} m_{truss} + \frac{12}{35} m_{beam}, \quad (\text{Eq. 39})$$

$$k_r = \frac{2EW_b^3h}{L_b^3}, \quad c_r = \frac{\sqrt{m_r k_r}}{Q} \quad (\text{Eq. 40})$$

The driving force applied on the shuttle comes from the change in capacitance of the comb fingers, which takes the form:

$$F_0 = V_P v_{in} \frac{\partial C}{\partial x} = \eta_e v_{in} \quad (\text{Eq. 41})$$

where C is the overlap capacitance between the comb fingers: $C = \frac{N\epsilon hL}{g_f}$; N is the total number of fingers; ϵ is the permittivity; h is the thickness of the structure and g_f is the gap spacing between fingers; and η_e is the electromechanical coupling coefficient, which takes the form:

$$\eta_e = V_P \frac{\partial C}{\partial x} = V_P \frac{\epsilon h}{g_f} \quad (\text{Eq. 42})$$

The governing equation of the periodically forced second order systems holds:

$$m_r \frac{\partial^2 x(t)}{\partial t^2} + c_r \frac{\partial x(t)}{\partial t} + k_r x(t) = F_0 \sin(\omega t) \quad (\text{Eq. 43})$$

For under-damped system ($\frac{c_r}{2m_r} < \sqrt{\frac{k_r}{m_r}}$), the expression for shuttle displacement $x(t)$ becomes

$$x(t) = (x_0 - x_{ss}) \exp(\sigma t) [\cos(\omega_d t) - \frac{\sigma}{\omega_d} \sin(\omega_d t)] + x_{ss} \quad (\text{Eq. 44})$$

Where $\sigma = -\frac{c_r}{2m_r} = -\frac{2\pi f_0}{2Q}$, $\omega_d = \sqrt{\frac{k_r}{m_r} - \left(\frac{c_r}{2m_r}\right)^2}$, x_0 is the initial displacement of the shuttle due to pre-energizing, and $x_{ss} = \frac{\eta_e v_{in}}{\omega_0 c_r} \sin(\omega_0 t + \phi)$ is the steady-state displacement.

To impact the output electrodes, the shuttle needs to vibrate with a large enough amplitude to overcome the impactor-to-electrode gap d_{switch} . Switch time t_{switch} is defined as the time required to reach the displacement from x_0 to d_{switch} with on-resonance input v_{in} . The rise time of the resoswitch for making impacting with the output electrodes, becomes:

$$t_{switch} = \frac{1}{\sigma} \ln \left(\frac{1 - d_{switch} k_r / Q \eta e v_{in}}{1 - x_0 k_r / Q \eta e v_{in}} \right) \quad (\text{Eq. 45})$$

The expression for time to impact (or switch time t_{switch}) shown in (Eq. 45) depends strongly on the starting displacement amplitude x_0 , which in turn depends on the input bit rate R_i , as shown in Eq. 46.

$$x_0 = d_{switch} \exp \left(-\frac{\pi f_0}{Q R_i} \right) \quad (\text{Eq. 46})$$

To illustrate, Fig. 3.4(a) depicts how resoswitch comes to a complete rest between mark bits and requires a long resoswitch mechanical switch time to impact when the input bit rate is low. This long switch time is not problematic when the bit rate is low. It would, however, be problematic if the bit rate were fast. When excited by the fast bit rate-modulated input depicted in Fig. 3.4(b), with a much shorter input bit period, the resoswitch is still vibrating by the (short) time the next mark input arrives. This means it possesses stored energy, i.e., it is pre-energized with an initial condition that allows it to reach the impact threshold much faster.

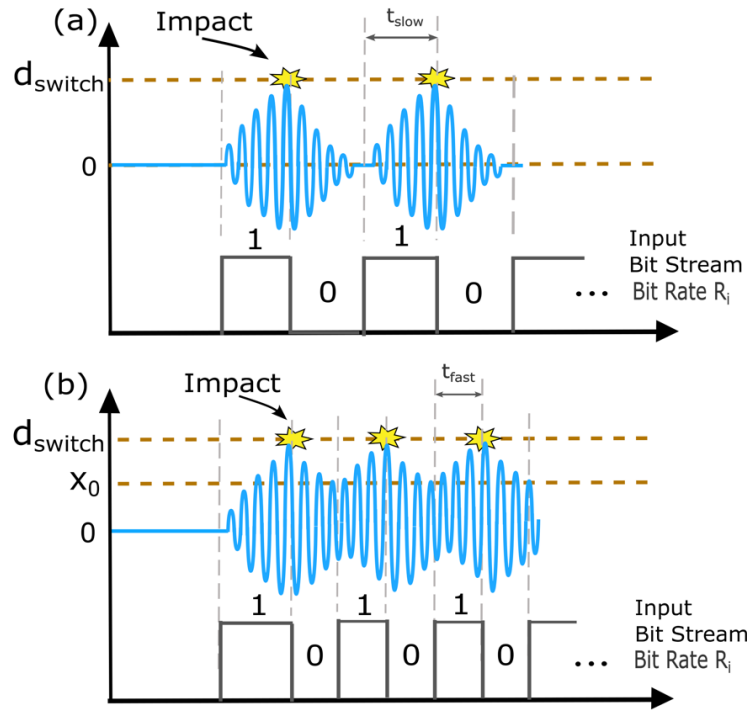


Fig. 3.4: (a) Long period ASK excitation of a resoswitch with long space periods allows the resoswitch to come to rest on each cycle, forcing it to traverse the full gap distance in order to impact again, greatly slowing the time to impact, i.e., the switching time t_{slow} . (b) Shorter period ASK marks (that realize a faster bit rate) do not allow the resoswitch to come to rest, allowing it to retain energy than then permits much faster rise times from the next mark input to impact, and thus much faster switching times t_{fast} to support the faster bit rate. Here, the long first ASK mark input is required to pre-energize the resoswitch before accepting the fast data rate.

Table III illustrates this by comparing the predicted performance of a resoswitch with

the design demonstrated in Section 3.2, but with assumed values of Q , one low (100) and one high (100,000). The $Q=100$ device posts a moderate sensitivity of -60.4 dBm (still adequate for short range communications) and a switching time of 1.23 ms. On the other hand, the $Q=100,000$ posts a much better sensitivity of -90.4 dBm, but a rather poor switching time of 1.23 s, hence, poor bit rate).

Table III: Predicted And Measured Pre-Energized Resoswitch Performance

	Section III Examples		Measured Devices			
Quality Factor, Q	100	100000	502	502	502	502
Input Bit Rate, R_i (bps)	Supported Bit Rate	Supported Bit Rate	1000	2000	4000	8000
Sensitivity, S (dBm)	-60.4	-90.4	-67.4	-67.4	-67.4	-67.4
	Not Pre-Energized					
Switch Time, t_{switch} (ms)	1.23	1230	1.58	1.58	1.58	1.58
Bit Rate, R_b (bps)	813	0.82	632	632	632	632
	Pre-Energized					
Switch Time, t_{switch} (ms)	0.0167	16.7	0.28	0.14	0.11	0.048
Bit Rate, R_b (bps)	71600	72	1000	2000	4000	8000

3.2.3 Maximum Bit Rate

The resoswitch has the ability to adapt to whatever bit rate by reducing its own switching time. The adaption is such that (Eq. 45) predicts that the switch time of resoswitch, t_{switch} , will not limit the ultimate bit rate, but rather some other factors. For example, resoswitch is vibrating on resonance frequency and this resonance frequency may ultimately restrict the maximum achievable bit rate.

The RC time constant associated with charging the output load, as shown in Fig. 3.5, is another factor that may limit the maximum bit rate of resoswitch. Our resoswitches are fabricated using gold as the structural materials, which has an electrical resistivity of approximately $2.44 \times 10^{-8} \Omega \cdot m$, lower than most metals commonly available in microfabrication processes. Hence the contact resistance R_{on} of resoswitch is quite small (few Ω s). With few pFs output load capacitance, the RC time constant constraint takes into account only with input bit rate in Gbps range.

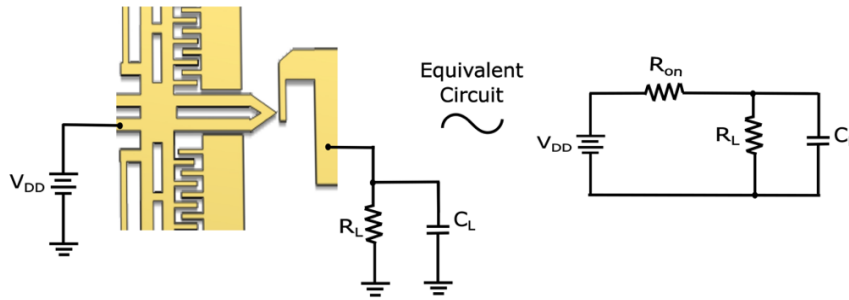


Fig. 3.5: Equivalent circuit of resowitch when impact happens. R_{on} is the contact resistance between shuttle and output electrode, R_L is the load resistance, C_L is the load capacitance and V_{DD} is the applied DC voltage on the shuttle. C_L will be charged up through R_{on} and discharge through R_L .

Additionally, the requirement of $t_{switch} < 1/R_i$ imposes an upper limit on the maximum bit rate when the driving force is relatively weak. Assuming that the maximum achievable displacement of the shuttle without output electrodes is x_{max} , if $x_{max} < 2 \times d_{switch}$ (i.e., input power $<$ Sensitivity + 6dBm), the maximum bit rate of the resowitch is primarily constrained by this requirement, expressed as:

$$R_{i,max} = \frac{\sigma}{\ln\left(\frac{\eta e v_{in} Q}{d_{switch} k r} - 1\right)} \quad (\text{Eq. 47})$$

For higher input power levels that give $x_{max} > 2 \times d_{switch}$ (i.e., input power $>$ Sensitivity + 6dBm), the dominant limiting factors shift to others such as resonance frequency. Fig. 3.6 presents the measured and theory-predicted maximum bit rate of resowitch when excited by 50% duty cycle ASK-modulated input signals with different driving strengths. When the input power is less than the threshold discussed above, Eq. 47 becomes the limit of maximum bit rate and this limit alleviates as the input strength increases, until it reaches the threshold.

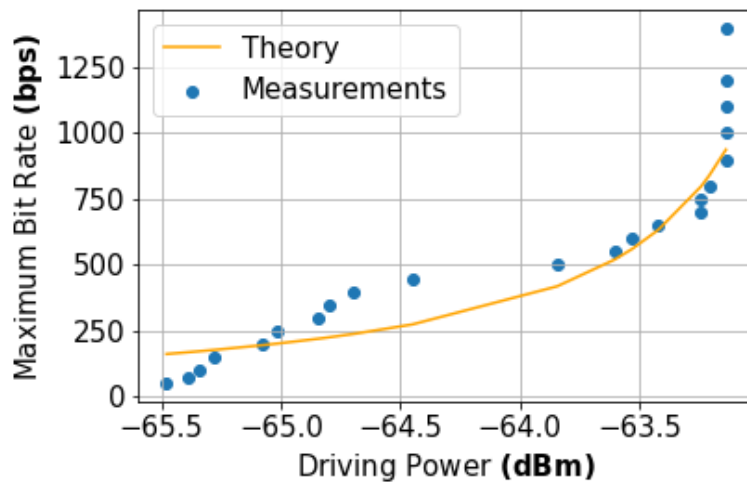


Fig. 3.6: Measured maximum bit rate vs. driving power.

Noises are believed to limit the bit rate of resowitch. Further investigation of maximum bit rate vs. signal-to-noise ratio (SNR) is needed.

3.2.4 What About Long Trains of 0's?

Clearly, the use of pre-energization is applicable only to cases where the communicated information signal does not contain long trains of 0's, which would of course remove the stored energy that enables fast switching. Fortunately, this is generally not an issue in communication applications, where synchronous clock encoding schemes like Manchester encoding [33], as shown in Fig. 3.7, are commonly used to ensure data security and speed of transmission. Manchester encoding divides a bit into two halves. The voltage remains the same during the first half and moves to the other level at the second half. The transition happens at the middle of the bit provides synchronization and eliminates long zero sequences. This feature broadens the use of resoswitches and pre-energizing methods in communication systems.

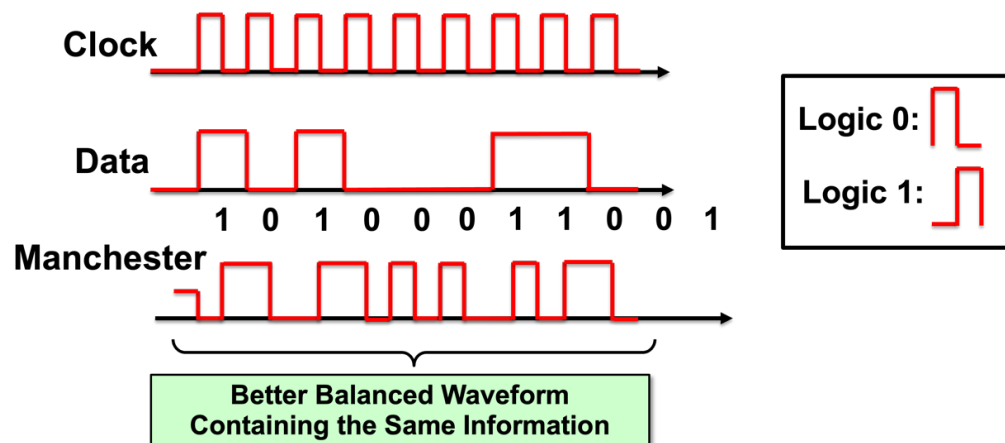


Fig. 3.7: Manchester encoding divides a bit into two halves with the transition happens at the middle of the bit. It provides synchronization and avoids the condition of long train of 0's.

3.3 Fabrication Process

The resoswitch in this work was fabricated using a simple single-mask electroplating process. Cross sections of major process steps are shown in Fig. 3.8.

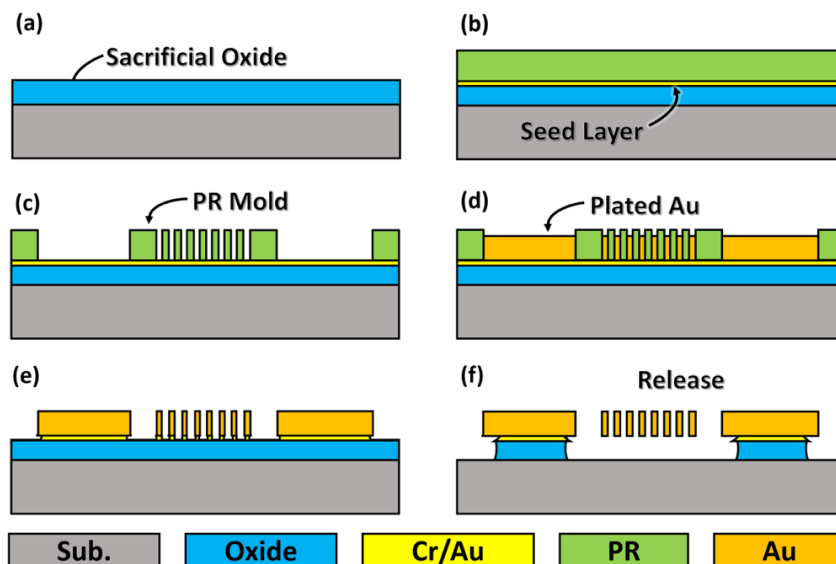


Fig. 3.8: Process flow of electroplated gold resoswitch.

The process begins on 6" blank Si wafers with LPCVD deposition of 2.5 μm LTO at 450°C to serve as a sacrificial layer, followed by a 1-hour annealing at 1000°C as depicted in Fig. 3.8(a). A seed layer comprised of 8nm Cr/25nm Au is then evaporated. The bottom layer of Cr serves as an adhesion layer between the sacrificial oxide and gold structure, and the central Au layer is the seed layer for electroplating. The seed layer needs to be very thin so that the removal process after electroplating does not significantly erode the structure. Spin photoresist 2.5- μm , expose and develop. Next, the Au structural layer is electroplated 1 μm thick, using a cyanide based electroplating solution (Elevate 7934) into the photoresist mold, as depicted in Fig. 3.8(d). The photoresist mold is then stripped using O₂ plasma, followed by Au and Cr-7 TFA etchants to remove the metal seed layers. Finally, the structure is released via a timed etch in vapor HF, while preserving sacrificial oxide under the large area anchors.

With an appropriate exposure energy, this process achieves 800nm gaps between comb fingers. Compared to the conventional photoresist mold used here, use of oxide mold allows higher resolution, i.e., smaller gaps between comb fingers, which will lead to a smaller device impedance as well as a better sensitivity.

3.4 Experimental Results

A Lakeshore FWPX vacuum probe station housed the resoswitch die during testing, providing 800- μ Torr vacuum and feedthrough connections to outside measurement instruments. A resoswitch diagnostic that lacked cantilever impact electrodes was first evaluated as a standalone resonator using the circuit of Fig. 3.9(a), which employs a mixing method to eliminate unwanted parasitic feedthrough current that might otherwise mask the motional current [34]. The measured frequency spectrum of Fig. 3.9(b) yields a resonance frequency f_0 and Q of 23.7 kHz and 502 (expected for gold), respectively.

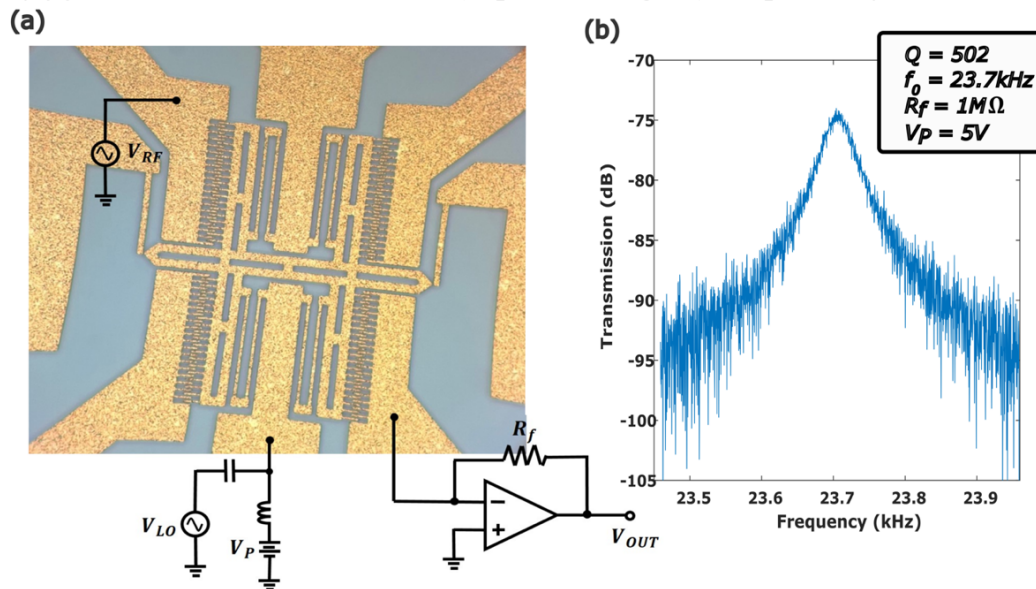


Fig. 3.9: (a) Mixing measurement setup and applied bias and local oscillator voltages to null parasitic feedthrough en route to obtaining the (b) transmission spectrum of the gold resoswitch, showing a resonance frequency of 23.7 kHz and a Q of 502.

A Tektronix AFG3102 Arbitrary Function Generator modulated a resonance carrier into ASK (gated sinusoid) waveforms to provide inputs for resoswitch performance evaluation. Fig. 3.10 presents measured oscilloscope waveforms of a resoswitch excited by a 50% duty cycle ASK-modulated input with four different input bit rates: (a) 1 kbps, (b) 2 kbps, (c) 4 kbps, and (d) 8 kbps. Note in each case how the resoswitch time to impact decreases as the bit rate increases, allowing the resoswitch to keep up with the bit rate, essentially adapting to each bit rate by retaining more energy as the bit period shrinks.

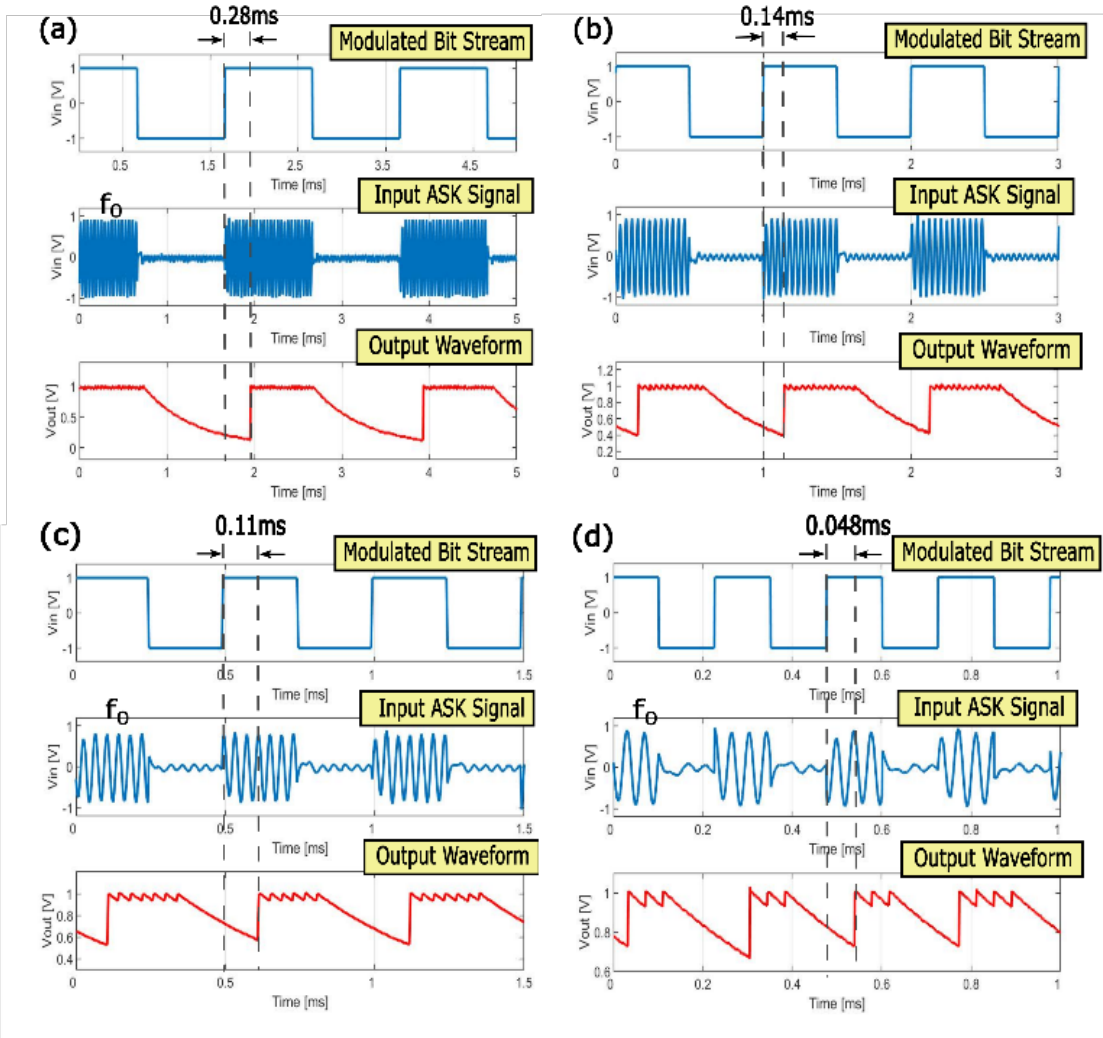


Fig. 3.10: Measured oscilloscope waveforms showing the modulation waveform, ASK input signal, and reswitch responses for three bit-period cases: (a) 1 kbps, (b) 2 kbps, (c) 4 kbps, and (d) 8 kbps. Note that the switch time—i.e., the time it takes for the output to go high after the input does—decreases to accommodate increasing bit rates, effectively adapting to them.

For a more structured evaluation of the performance of pre-energized reswitches, Fig. 3.11 present plots of the measured switching time t_{switch} of three devices with varied starting displacement amplitude x_0 alongside model-predicted curves using measured values of f_0 and Q , and calculated x_0 and d_{switch}/x_{max} . Here, the starting displacement amplitude x_0 is controlled by varying pre-energizing time T (cf. Fig. 3.11) and/or pre-energizing modulation factor M , which takes the form:

$$\frac{x_0(T, M)}{x_{max}} = \frac{v_M}{v_{in}} \left(1 - \exp\left(-\frac{\pi f_0 T}{Q}\right) \right) = M \left(1 - \exp\left(-\frac{\pi f_0 T}{Q}\right) \right) \quad (\text{Eq. 48})$$

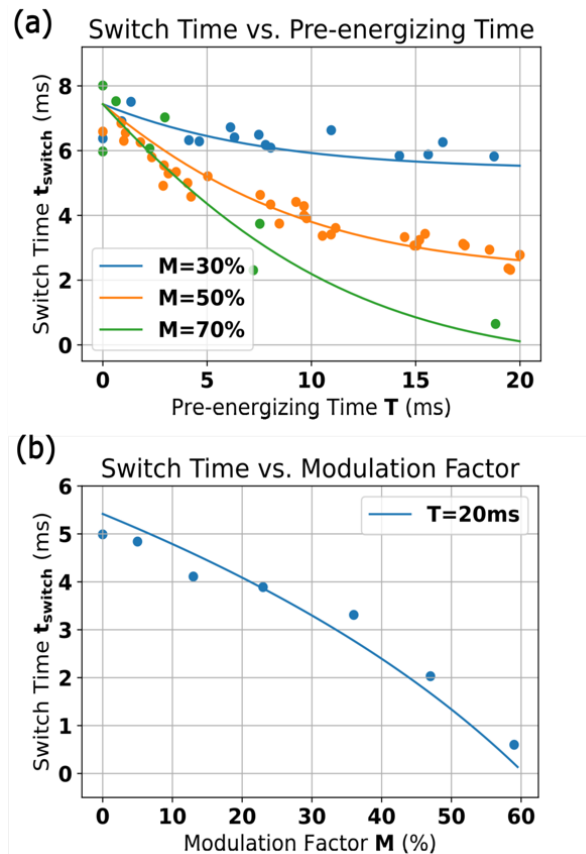


Fig. 3.11: (a) Switching time vs. pre-energizing time T (cf. Fig. 3.12) at different modulation factors. Here, switching time decreases with higher pre-energizing amplitudes and longer pre-energizing times. (b) Switching time vs. modulation factor (V_M in Fig. 3.12) for a 50% duty-cycle square wave input with $T=20$ ms. Increasing the modulation factor decreases the switching time, since it increases the initial displacement amplitude upon an input rise.

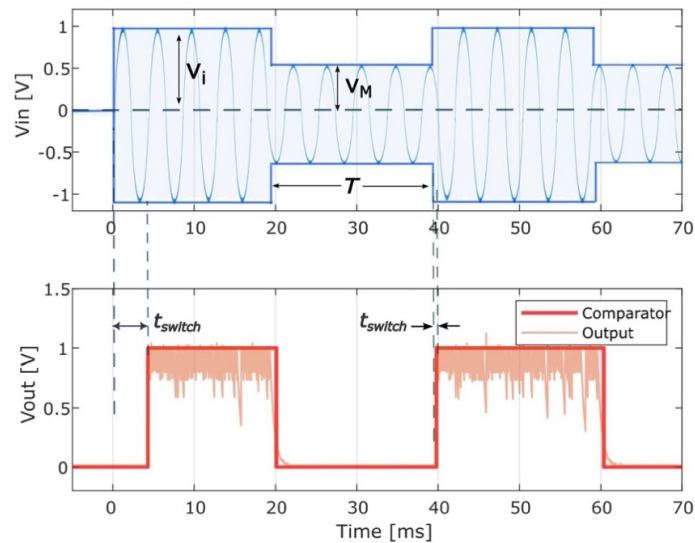


Fig. 3.12: Switch time with and without pre-energization. The first bit with amplitude V_i has no pre-energization and shows a long switch time. Between the first and second bit is a pre-energizing period where the input amplitude is reduced to V_M for time T . The switch time for the second bit is subsequently faster.

In each scenario, the switching time decreases as pre-energization increases, reaching as low as 48 microseconds in some cases. The close alignment between theoretical predictions and experimental results confirms the validity of our pre-energization theory.

3.5 Conclusion

This demonstration of resoswitch receivers achieving reasonable bit rate communication, despite their inherently high Q , marks a substantial advancement in the practical applications of resoswitch technology. Traditionally, resoswitches have been seen as suitable mainly for low-data applications, such as simple label updates or periodic timing synchronization. However, the results here expand the potential applications significantly, suggesting that resoswitch receivers could now be considered suitable for higher data-rate tasks. These include more demanding applications such as wireless audio reception, data-rich telemetry, and even large-scale firmware updates sent from a central location to devices distributed across vast distance. In particular, the ability of resoswitches to operate with low-frequency signals opens the possibility of leveraging established WWVB channels, such as the 60-kHz band traditionally used for radio-controlled clocks, to broadcast data over continental distances.

A key factor enabling this leap in functionality is the successful use of pre-energization to address switching time constraints, which historically limited resoswitch communication rates. With pre-energization, switching speed is no longer the primary bottleneck, shifting the main limiting factor for further bit rate increases to the resonance frequency of the resoswitch itself. This development suggests a clear path for future research aimed at achieving even higher communication rates: by increasing the resonance frequency while preserving sufficient sensitivity, resoswitches could be optimized for a broader range of high-performance communication requirements. This would open up new possibilities for high-bitrate, ultra-low-power communication, particularly in the domain of the Internet of Things (IoT) and other large-scale, distributed sensing networks where power efficiency and durability are critical.

In large-scale sensor networks and IoT applications, where battery-powered devices must operate for years without maintenance, the ultra-low-power characteristics of resoswitch receivers make them especially attractive. The fact that resoswitches consume no standby power and require minimal power during operation provides a significant advantage over traditional CMOS-based receivers, which typically exhibit higher power consumption and may require frequent battery replacements or recharges. By contrast, resoswitch receivers offer a sustainable alternative for deployments in remote or inaccessible locations, such as environmental monitoring stations, agricultural sensors, or smart infrastructure, where long-term reliability and low energy requirements are essential.

Beyond IoT, resoswitches could also play a role in challenging environments where electronic receivers are less effective. For instance, in high-temperature, high-radiation, or high-vibration settings, mechanical switches are often more robust than their semiconductor counterparts, providing reliable performance where traditional electronics may fail. These characteristics position resoswitches as a compelling option for harsh-environment communication systems, including industrial process monitoring, space applications, and

deep-sea exploration.

In conclusion, the advancements demonstrated here underscore the versatility of resoswitch technology and highlight its potential to enable high-data-rate communication within a highly energy-efficient framework. As resoswitch designs continue to evolve, particularly with respect to resonance frequency and sensitivity improvements, their application in the field of wireless communication could broaden considerably. Ultimately, the combination of high bit rates, ultra-low-power operation, and resilience in challenging environments may well position resoswitches as a core component in the next generation of wireless communication systems, paving the way for more sustainable, reliable, and high-performance sensor networks and IoT ecosystems. Future work should continue to explore these directions, aiming to optimize resoswitch parameters to meet the diverse needs of large-scale, distributed applications where conventional electronics may not suffice.

Chapter 4

Ferrite-Rod Antenna Driven Wireless Resoswitch Receiver

This chapter presents the design, implementation, and testing of a micromechanical resoswitch receiver that achieves short-range wireless reception at 23.7 kHz, driven by a ferrite-rod antenna and demonstrating sensitivity better than -62 dBm at an on-off keying (OOK) bit rate of 0.9 kbit/s. Experimental results validate performance models that predict the receiver's maximum achievable bit rate, with an adaptation capacity up to 8 kbit/s in the absence of the antenna. However, when coupled to a finite-bandwidth antenna, the system displays a clear trade-off between sensitivity and bit rate, as signal rise times become limited by the antenna's bandwidth constraints. Unlike conventional RFID tags, the resoswitch receiver's high-Q mechanical resonance enables it to reject interference from out-of-band signals in congested environments, enhancing its applicability in challenging wireless settings. Another unique feature of the resoswitch receiver is its ability to consume zero power while passively waiting for incoming signals. This inherently low-power operation, combined with selective filtering through mechanical resonance, makes the resoswitch an attractive candidate for always-on, low-bit-rate applications such as sensor networks. Future advancements in antenna-resoswitch co-design, especially with optimized ferrite-rod antennas matched to the desired frequency range, could expand the operating bandwidth and improve impedance matching, enabling the resoswitch receiver to support higher bit rates for more complex applications, such as voice communication over greater distances.

4.1 Introduction

Micromechanical resonant switches, or "resoswitches," represent a novel approach to achieving transistor-less mechanical communication receivers by harnessing resonant vibration to minimize the power required to close a mechanical switch [12][35]. This resonant principle allows the resoswitch to act as a mechanical filter, amplifier, and demodulator for communication signals, resulting in devices capable of bit rates up to 1 kbit/s with sensitivities as low as -60 dBm—all while consuming zero power in a passive "listening" mode when waiting for valid input signals [36]. This passive operation means that the resoswitches do not require sleep/wake cycling for power conservation, positioning them as ideal candidates for

always-on monitoring applications, such as remote sensors or low-power IoT devices that demand continuous availability without frequent battery replacement.

A recent advancement in resoswitch design introduces pre-energization, which enables a significant increase in bit rate capacity, allowing these devices to achieve up to 8 kbit/s [17]. This enhancement broadens the application scope of resoswitches from low bit-rate uses, like RFID tagging or label updates, to more data-intensive uses, such as voice communications. Theoretical models predict that, with pre-energization, resoswitches can adjust to higher bit rates as needed, limited only by external system constraints, such as environmental noise or the finite electrical bandwidth of the overall system.

In this work, we explore the practical impact of these bandwidth limitations by analyzing the wireless performance of a resoswitch when interfaced with a ferrite-rod antenna. Ferrite-rod antennas are particularly well-suited to this type of device, as they can be tuned to frequencies within the 20-kHz range and provide relatively high output impedance in the range of $>10\text{ k}\Omega$, aiding in signal transfer to the resoswitch. While pre-energization theory suggests that the intrinsic Q-factor of the resoswitch itself does not limit achievable bit rates [16], experimental findings indicate that the Q-factor of the antenna's matching network may impose practical bandwidth limitations. This bandwidth constraint, dictated by the limited rise time of the received signal due to the antenna, can reduce the maximum achievable bit rate.

Ultimately, leveraging the full potential of high bit-rate resoswitch receivers will require careful co-design between the resoswitch and its antenna. By matching the antenna's bandwidth with the resoswitch's capabilities, these devices could achieve higher bit rates and better sensitivities, paving the way for efficient, low-power communication solutions in always-on applications.

4.2 Device Structure and Operation

Fig. 4.1 illustrates the wireless demonstration setup that employs ferrite-rod antennas coupled with a resoswitch configured as a wireless receiver. This experimental setup highlights the capabilities of a micromechanical resonant switch (or "resoswitch") in receiving and demodulating wireless signals at ultra-low power levels. The central element of the resoswitch is a movable gold shuttle, which is suspended $2.5\text{ }\mu\text{m}$ above a silicon substrate by folded-beam springs. These folded-beam springs provide a flexible suspension mechanism, allowing the shuttle to respond to mechanical vibrations while remaining stable in its resting position. On either side of the shuttle are two comb-drive transducer electrode pairs with interdigitated fingers. These comb-drives convert electrical input signals from the antenna into mechanical vibrations in the shuttle, facilitating signal transduction and amplification at resonance. The shuttle is also equipped with two sharp impactor protrusions, positioned precisely $1\text{ }\mu\text{m}$ away from spring-softened impact output electrodes. This arrangement allows the shuttle to make contact with the output electrodes when resonated, creating a switching action that effectively demodulates the incoming signal.

The ferrite-rod receive antenna, selected for its ability to operate in the low-frequency 20-kHz range and its relatively high output impedance ($>10\text{ k}\Omega$), is connected directly to the left input electrode. This transducer translates incoming signals from the antenna into

mechanical movements in the shuttle, driving the receiver's operation. The right input electrode is not used in this setup but could be used in a differential configuration, enhancing the electromechanical coupling when a differential input signal is available. This could be achieved, for example, by using a balun to convert a single-ended signal into a balanced differential input [13], thereby improving the overall sensitivity and selectivity of the resoswitch.

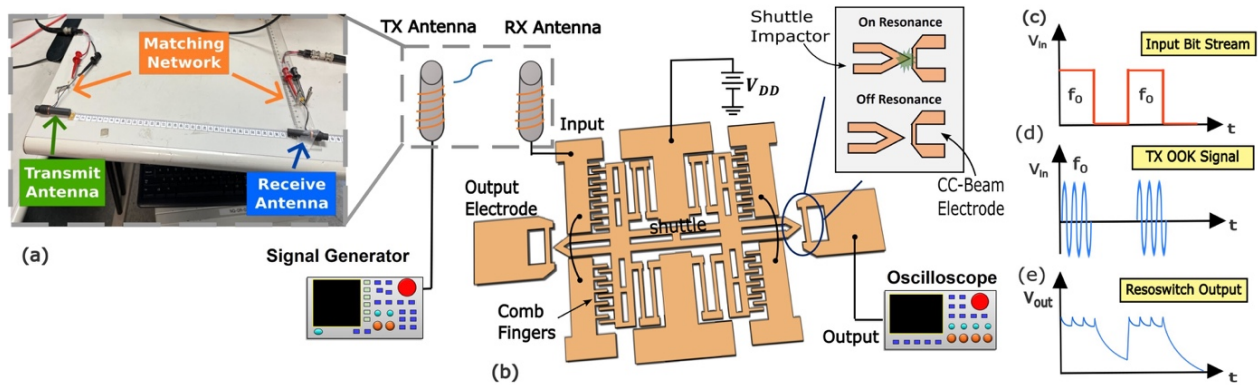


Fig. 4.1: Wireless communication demonstration set-up employing (a) ferrite-rod antennas and (b) an all-mechanical resoswitch to receive and demodulate the (d) OOK-modulated data bit stream of (c) into the matching resoswitch output bit stream of (e).

For proper operation, a DC bias voltage V_{DD} , set to 5V in this demonstration, is applied to the shuttle. This DC bias amplifies the electrostatic force generated by the input signal received from the antenna. Importantly, applying V_{DD} to the resoswitch shuttle consumes no power while the device is in standby, as the shuttle, when at rest, functions like one plate of a charged capacitor. In this idle state, the resoswitch is effectively in a low power “listening” mode, consuming no power until it receives a valid input that drives it to demodulate and amplify the signal.

In this demonstration, data is transmitted in the form of a bit stream, as depicted in Fig. 4.1(c). The data is modulated onto a carrier frequency before transmission through the communication channel. On-off keying (OOK) modulation is utilized, with each binary ‘1’ represented by a sinusoidal waveform at the resonance frequency of the resoswitch, and each ‘0’ by a zero-volt signal. This scheme allows the system to conserve energy, as transmitting a ‘0’ involves sending no signal at all. When a ‘0’ bit is transmitted, no signal is received, and the shuttle remains stationary. Any residual charge on the load capacitor C_L gradually discharges to ground through a large bleed resistor R_L , which in this setup is provided by the 1 M Ω input impedance of the connected oscilloscope. As a result, the voltage across the load capacitor reads 0V, indicating the successful transmission and reception of a ‘0’ bit.

Conversely, when a ‘1’ bit is transmitted, the transmitting antenna outputs a sinusoidal waveform at the resonance frequency of the resoswitch. This signal is received by the ferrite-rod antenna, which drives the resoswitch shuttle into resonance. At resonance, the shuttle vibrates and periodically makes contact with the output electrode, transferring charge from V_{DD} to C_L upon each impact. This results in the output voltage rising to V_{DD} , marking the

successful transmission and reception of a ‘1’ bit. Each mechanical contact charges the output capacitor, producing a clear and detectable signal at the receiver output.

One of the key advantages of the resoswitch-based receiver is its selective sensitivity to signals within its resonant passband. Only input signals within the passband of the resoswitch, which benefit from amplification due to the high quality factor (Q) of the device, can effectively drive the shuttle to impact. Stray signals or off-resonance interferers from other wireless sources are unable to achieve sufficient amplitude to make an impact, meaning they are inherently rejected by the system. This selective responsiveness provides the resoswitch with robust immunity to out-of-band interference, making it well-suited for operation in congested wireless environments. As a result, the resoswitch demonstrates desirable characteristics for low-power, high-selectivity wireless reception, showcasing the potential for deployment in applications requiring continuous monitoring with zero standby power consumption.

4.3 Antenna-Resoswitch Co-Design

Feeding a resoswitch receiver with a ferrite-rod antenna presents two main challenges: impedance matching and limited bandwidth. The high impedance of the comb-driven resonator is difficult to match with that of the antenna, leading to potential power losses; Additionally, the small, tuned bandwidth of the ferrite-rod antenna and its matching network restricts the range of frequencies they can efficiently capture.

4.3.1 Ferrite-Rod Antenna

Each ferrite-rod antenna shown in Fig. 4.1 consists of a magnetic rod wrapped with multiple turns of wire, allowing it to function as an electrically small antenna. In small loop antennas like these, the current flowing around the loop remains in phase because the total conductor length is much shorter than the wavelength (λ) of the signal. The ferrite core enhances the antenna’s effective area by concentrating magnetic field lines, resulting in a stronger magnetic coupling. By increasing the number of wire turns and the loop area, the voltage generated across the antenna terminals rises for a given magnetic field strength, though at the expense of increased physical size.

Electrically, a ferrite-rod antenna behaves primarily as an inductor with reactance $X=2\pi fL$, where f is the operating frequency, and L represents the coil inductance. Although there is also a series radiation resistance R_R and loss resistance R_L associated with the antenna, these values are typically small compared to the inductive reactance [37], making them less significant for the antenna’s performance at low frequencies-rod antennas. However, ferrite-rod antennas are generally inefficient due to their small physical size compared to the wavelength and their low radiation resistance, which limits their power radiation capabilities.

To compensate for this inefficiency, ferrite-rod antennas are often tuned using a parallel capacitor connected across the loop terminals. This configuration creates a parallel-resonant LC circuit, which amplifies the output voltage by a factor of Q_{ant} , the quality factor of the antenna. Although this Q_{ant} enhances signal reception, the trade-off is a narrower bandwidth.

The bandwidth f_{BW} of the antenna is inversely related to the quality factor Q_{ant} , expressed as $f_{BW}=f_0/Q_{ant}$, where f_0 is the resonance frequency.

In this work, commercially available ferrite-rod antennas designed for long-range signal reception at approximately 60 kHz were tuned for use at 23.7 kHz, the resonance frequency of the resoswitch. Both S11 and LCR meter measurements indicate inductances in the 10-15 mH range for these antennas. To tune the antenna to the desired 23.7 kHz, an external 6.8 nF capacitor was added in parallel.

Fig. 4.2 shows the real part of the measured S_{11} converted to Z (impedance) parameters. Before tuning, the antenna naturally resonates around 60 kHz with an impedance of only 22 Ω at 23.7 kHz. After adding the tuning capacitor, the resonant frequency shifts down to align with the resoswitch frequency, significantly increasing the real part of the antenna's impedance to around 31 k Ω . This impedance boost is preferred for matching with the high impedance of the resoswitch, enhancing power transfer. However, this tuning also reduces the antenna's bandwidth from approximately 5.6 kHz at 60 kHz to just 3 kHz at 23.7 kHz. This reduction in bandwidth will, as discussed later, limit the maximum achievable bit rate of the wireless receiver.

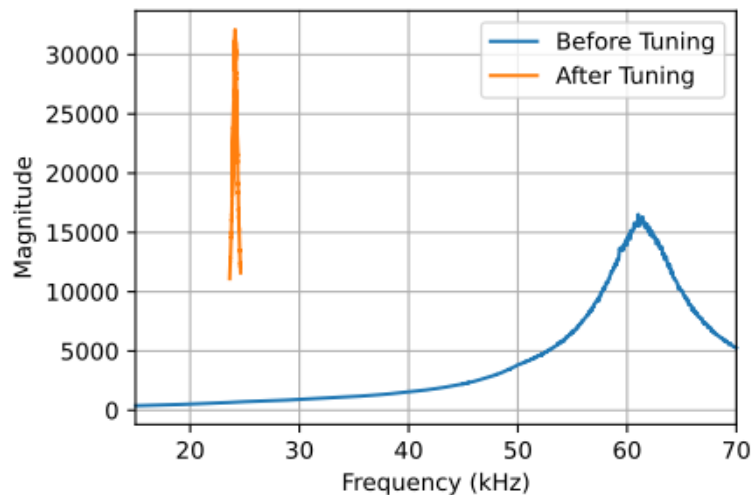


Fig. 4.2: Z parameter magnitude, derived from measured S parameters, of the ferrite-rod antenna before and after tuning.

4.3.2 Impedance Matching

The motional resistance R_x of the resoswitch in this work is that of a comb-driven resonator [38], which is highly dependent on factors such as the gap spacing between the comb-drive fingers and the applied DC bias voltage. As highlighted in Table IV, Device 1—a standard resoswitch design used in this study—has an estimated motional resistance R_x of 1654 M Ω , calculated based on device dimensions and operating conditions. This extremely high resistance is significantly larger than the 31 k Ω impedance of the receive antenna, resulting in a substantial mismatch between the antenna and resoswitch. This impedance mismatch hinders efficient power transfer from the antenna to the resoswitch, reducing the overall sensitivity and efficiency of the system.

To mitigate this issue, a scaled resoswitch design could be implemented, as indicated by Device 2 in Table IV. Device 2 employs the lithography technology as described in [38] to achieve a smaller finger gap, along with improved quality factors (Q) as presented in [30]. These design enhancements would give resoswitch a significantly lower motional resistance, potentially closer to the 31 k Ω of the receive antenna, thus facilitating better impedance matching. This more aggressive design approach could reduce the impedance mismatch, improving sensitivity and signal transfer efficiency.

However, for the purposes of this study, Device 1 was used despite the impedance mismatch. Using the sensitivity formula provided in [13], we calculate that the 1654 M Ω to 31 k Ω impedance mismatch imposes an additional 47 dB of loss between the antenna and resoswitch, compared to a matched system. Consequently, an input power level of approximately -18 dBm must be present at the antenna to achieve impacting within the resoswitch, corresponding to an effective sensitivity of -65 dBm. This sensitivity level, while not optimal, is still adequate for certain short-range applications, such as those found in RFID tags and other proximity-based communication devices where signal range requirements are minimal.

Thus, while Device 1's impedance mismatch limits its efficiency in longer-range applications, it remains suitable for short-range wireless communication. This underscores the potential benefits of improved impedance matching for future designs, where achieving a closer match between the resoswitch and antenna could enable better sensitivity and extended range.

4.4 Experimental Results

The 23.7-kHz gold micromechanical resoswitch was fabricated through a one-mask process similar to the techniques in [13]. This device, characterized by its key attributes summarized in Table IV and imaged via SEM in Fig. 4.3, was carefully prepared for performance testing. Placed inside a LakeShore FWPX vacuum probe station at a pressure of 1 mTorr, the resoswitch operated in a high vacuum environment to minimize damping and optimize the quality factor (Q). Within the chamber, the input, output, and shuttle electrodes were precisely probed, with signals routed externally to the receive antenna, a Keysight DSO1024 oscilloscope, and a dc power supply. To initiate transmission, a Tektronix AFG3102 function generator provided the on-off keying (OOK) modulated bit stream to the ferrite-rod transmit antenna, serving as the communication source.

Table IV: Resoswitch Design and Performance

Parameter	This Work (Device 1)	Scaled (Device 2)
Thickness, h [μm]	1.3	1.3
Finger Gap, d [μm]	1.0	0.1
Impact Gap, d_0 [μm]	1.0	0.1
Number of Fingers, N_f	38	270
Finger Width [μm]	1	0.1
Shuttle Mass [kg]	1.55×10^{-12}	1.50×10^{-12}
Frequency [kHz]	23.712	23.712
Q_{res}	706	7,200
V_P [V]	5	5
R_x [M Ω]	1654	0.032
Sensitivity [dBm]	-65.2	-92

Fig. 4.4 displays the received power as a function of distance between the transmit and receive antennas, powered by a function generator output of 13.6 dBm (~ 23 mW). As expected, the received power followed an inverse square dependency on distance, affirming basic antenna theory. Despite the transmit antenna's small size and inherent inefficiency, the setup (depicted in Fig. 4.1) demonstrated a viable range of up to 18 cm, achieving the -65.2 dBm sensitivity needed by the resoswitch receiver for effective detection. This sensitivity threshold is particularly promising for short-range applications, such as in RFID tagging, where proximity is sufficient for reliable performance. The adaptive bit rate capability of the resoswitch, as outlined in [17], hinges on its ability to harness the energy stored within its high-Q resonant structure during periods of inactivity, i.e., during '0' bits. The device's high Q allows it to continue vibrating briefly even after the drive signal is removed, preserving some resonant energy until the next '1' bit arrives. When a new '1' bit is received, this pre-existing vibrational energy allows the resoswitch to achieve impact more quickly, effectively enabling faster bit rate adaptation. The efficiency of this stored energy depends on the amplitude of the driving signal during '1' inputs, making signal strength critical.

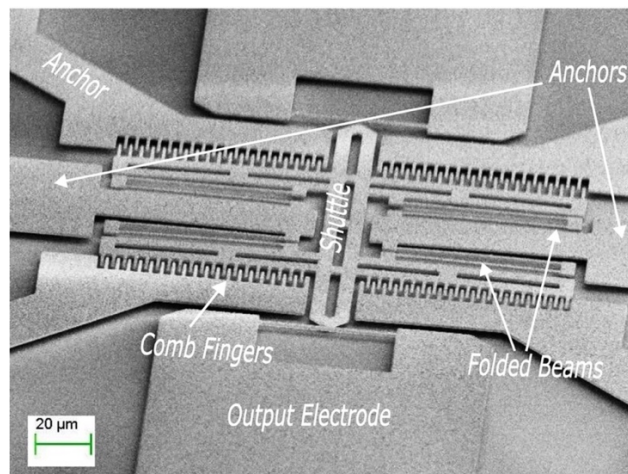


Fig. 4.3: SEM micrograph of the single-mask electroplated-gold resoswitch fabricated for this work.

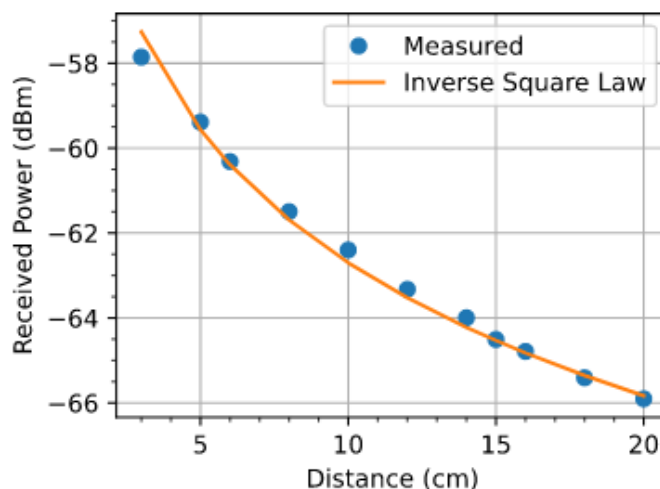


Fig. 4.4: Measured power delivered to the resoswitch vs. antenna separation distance falls off with an inverse square law.

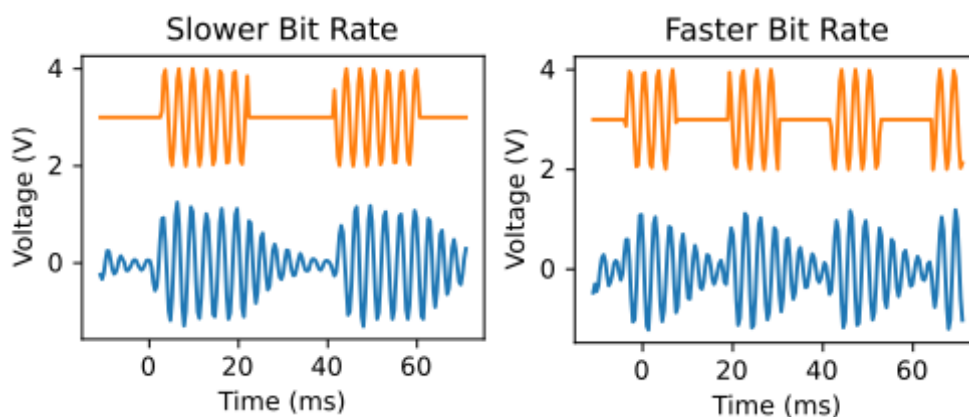


Fig. 4.5: Transmitted (orange) and antenna received (blue) waveforms (decimated to show sinusoid) for the cases of slow and fast bit rates.

The amount of stored energy in a resoswitch depends on the drive efficiency during the pre-energization period, which practically means it depends on the drive amplitude during a '1' input. OOK signals directly fed to a resoswitch input would appear as the orange curves in Fig. 4.5 (measured at the function generator output), where the gated-sinusoid envelopes have sharp edge transitions, indicating the presence of energy at higher harmonic frequencies. On the other hand, if the OOK signals go through a band-limited channel before appearing at the resoswitch receiver input, the loss of high frequency content results in the blue curves measured at the 3-kHz bandwidth receive antenna output, showing reduced amplitude and more gradual up and down transitions. These less efficient waveforms not only hurt the receive sensitivity of the resoswitch but also deliver energy more slowly, so reduce its pre-energization.

This then compromises its ability to adapt to the incoming bit rate, thereby reducing its maximum bit rate. To illustrate this phenomenon, Fig. 4.6 presents measured OOK-modulated waveforms transmitted at 13.6 dBm (green) over 15 cm and received (blue) by the respective antennas, clearly showing waveform distortion caused by finite channel bandwidth. Despite this, the resoswitch still successfully demodulates the waveform, where the output bit stream (orange) matches the input up to 900bit/s. Fig. 4.7 presents similar plots using a 1 kbit/s rate

that ensue when first using a much wider channel bandwidth, then attempting this same bit rate via the antenna-band-limited wireless channel. Without the antennas, the bit rate adapting ability of the resoswitch can keep up with the 1 kbit/s rate and further permits a rate of 8 kbit/s [17], which is 8 times faster than this and the highest yet demonstrated. The addition of the antennas and consequent bandlimited channel results in the last plot (green), where the resoswitch clearly can no longer track the incoming 1 kbit/s data stream, confirming the impact of the 3-kHz channel limit.

Fig. 4.8 finally presents a measured plot of wireless sensitivity (i.e., the minimum detectable power delivered to the resoswitch) vs. the input bit rate, showing a sensitivity of -65 dBm at 100 bit/s that worsens (due to waveform distortion) to -62.2 dBm at the maximum bit rate of 900 bits/s, both sufficient for short range sensor network applications.

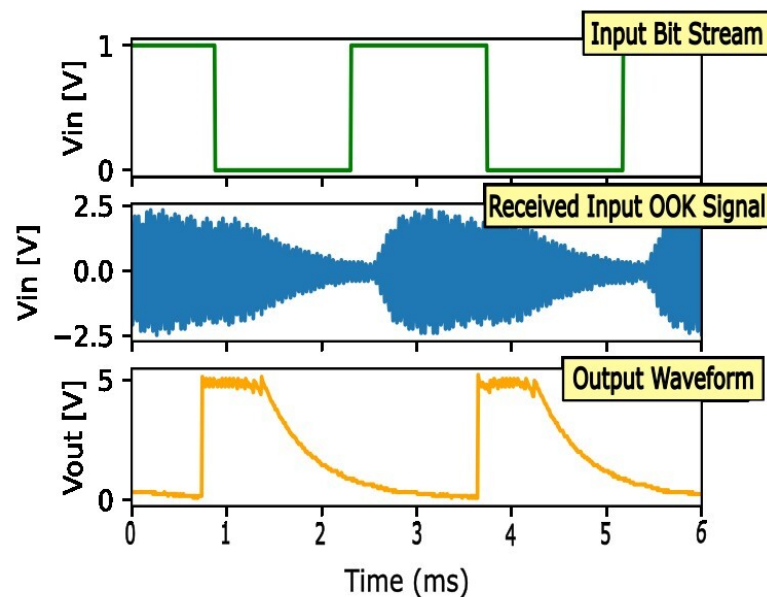
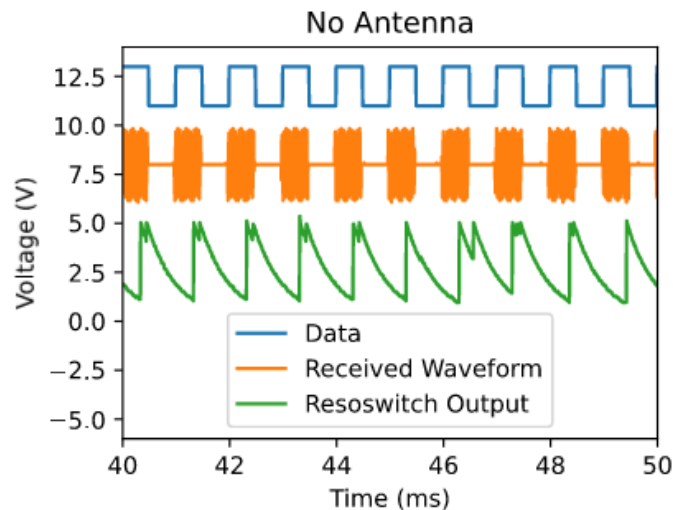


Fig. 4.6: Measured waveforms showing successful wireless demodulation using the antenna-fed resoswitch receiver.



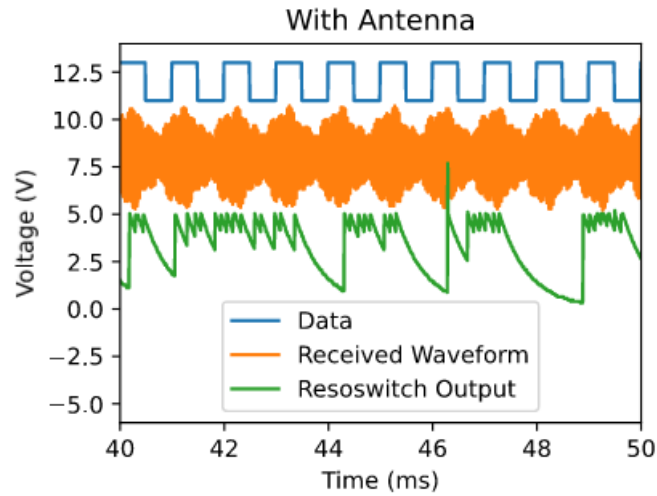


Fig. 4.7: Measured comparison of received waveforms (orange) and resoswitch outputs (green) at 1 kbit/sec connected directly (top) and wirelessly using an antenna (bottom).

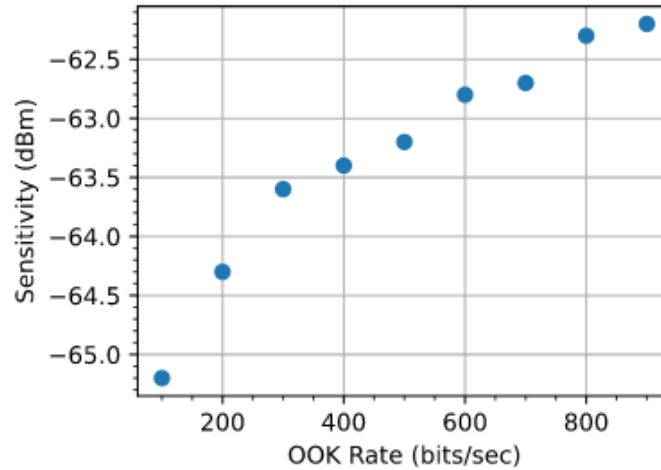


Fig. 4.8: Measured ferrite-rod antenna-driven resoswitch receiver sensitivity vs. transmit bit rate.

4.5 Conclusion

The successful demonstration of a 900 bit/s data rate over a wireless channel using an all-mechanical resoswitch receiver, even in the presence of a significant impedance mismatch, is a promising step forward for mechanical wireless communication systems. This result highlights the viability of using resoswitch technology in low-power, wireless communication applications, showing that a mechanically based receiver can indeed achieve respectable data rates without requiring traditional electronic components.

While the observed bandwidth limitations, imposed by the ferrite-rod antenna, restrict the achievable bit rate in this demonstration. These constraints are largely attributed to the fact that the ferrite-rod antennas used were initially designed for a different frequency range. As such, tuning was necessary to adjust them to the target frequency, which inevitably compromised their bandwidth and, in turn, the achievable bit rate of the resoswitch system. If

antennas were designed specifically for the resoswitch's operational frequency, it is likely that the system could support a wider bandwidth, which allows the receiver to reach its full potential of 8 kbit/s [17]. At this higher data rate, the resoswitch receiver would fit more data-intensive applications, such as voice communications, which would mark a considerable advancement in the capabilities of mechanical wireless systems.

Looking forward, the use of smaller, custom-designed ferrite-rod antennas tuned to the desired frequency range presents a clear path for improvement. These antennas would not only provide better impedance matching but also reduce physical size, making the system more compact and practical for real-world applications. Furthermore, pairing these optimized antennas with a more aggressively dimensioned resoswitch, such as Device 2 in Table IV, which offers better impedance matching and a lower motional resistance, could significantly enhance the receiver's working range and sensitivity. This combination of optimized antenna design and advanced resoswitch technology could ultimately enable longer-range, higher-bit-rate wireless communication, expanding the scope of mechanical receivers to include applications such as short-range voice transmission and other higher data-rate services.

Chapter 5

Push-Pull Resoswitch Communication Receiver

All-mechanical communication and clock receivers based on micromechanical resonant switches, or resoswitches (Fig. 5.1) [39], offer a promising alternative for energy-efficient wireless communication. These devices are uniquely capable of receiving On-Off Keyed (OOK) or Frequency Shift Keyed (FSK) modulated signals and demodulating them; however, prior to this work, they were limited to OOK operation [13][36]. Resoswitches possess a distinctive advantage over conventional static switches: rather than merely closing to transfer charge, they operate by repeatedly impacting two conductors. This dynamic switching approach not only enhances the reliability of the resoswitches by reducing issues related to contact wear but also introduces frequency addressability, which allows each resoswitch to selectively respond to a specific frequency range. This feature enables multiple resoswitches to be embedded within a system and independently tuned to different frequency bands, creating the potential for frequency multiplexing in low-power communication systems.

A critical advantage of resoswitch-based receivers is their ability to monitor for incoming communication signals in a power-free standby mode. When no input is present, these devices consume zero power, unlike CMOS-based receivers that typically require some level of quiescent current for standby operation. This ultra-low-power operation is highly advantageous for battery-powered systems, especially in remote or hard-to-reach locations, where extending device lifespan is essential and frequent battery replacements are impractical. With recent developments, resoswitches have moved beyond merely supporting low data rates; specifically, the introduction of stored resonance energy techniques has enabled bit rates up to 8 kbit/s [17]. This advancement allows resoswitch receivers to tackle more data-intensive applications, expanding their usability from simple, low-bit-rate tasks—like cross-continent label updates or periodic timing synchronization—to higher bit rate applications, potentially including real-time audio communication or wireless firmware updates.

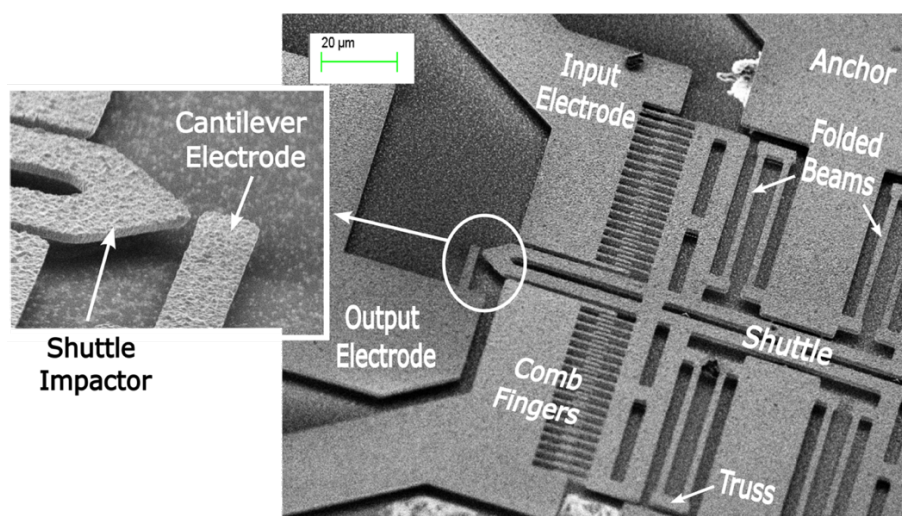


Fig. 5.1: SEM of a gold resoswitch identifying important features. Upon application of a dc-biased sinusoid at the device resonance frequency to the input comb-finger electrode, the movable suspended shuttle vibrates to impact the output electrode, periodically closing the shuttle-to-output switch.

Unfortunately, squegging, a phenomenon where non-ideal impacts cause de-phasing between the input drive and shuttle motion, poses a substantial challenge for resoswitch reliability and stability. This de-phasing can disrupt the efficient transfer of resonance energy to the shuttle, leading to intermittent or missed impacts that ultimately compromise the stability of the output waveform and degrade the overall system performance. As a result, squegging not only undermines the data integrity by increasing bit error rates but also creates frequency instability in the output signal, posing serious issues in applications requiring precise and stable frequency control. The impact of squegging has been especially problematic in earlier resoswitch receivers, which struggled to maintain reliable output frequency without extensive error correction mechanisms [40].

Pursuant to eliminating squegging and enabling full FSK demodulation (with its bit error rate benefits), this work introduces an innovative push-pull configuration using two frequency-spaced resoswitches (cf. Fig. 5.3). This dual-resoswitch setup significantly reduces the phase-related instabilities associated with squegging, allowing the two resoswitches to alternate in responding to their respective frequencies. With this push-pull approach, the system achieves smooth, glitch-free output waveforms with bit rates in the range of 100-1000 bit/s. Notably, the output exhibits near-perfect "brick wall" transitions, resulting in sharp, well-defined bit intervals that offer substantially greater stability and predictability than prior designs. This increased stability is particularly valuable in applications where reliable bit distinction and minimal error rates are critical.

The push-pull resoswitch configuration represents a significant leap forward in mitigating the limitations imposed by squegging. By ensuring stable, error-free output across a wide bit rate range, this design enhances the functional viability of resoswitch technology for data-intensive applications, including those requiring consistent FSK demodulation. This work not only demonstrates a practical solution to one of the most persistent challenges in

resoswitch design but also opens the door for broader adoption of resoswitch-based communication systems in diverse, power-sensitive applications.

5.1 Resoswitch Impact Dynamics – Squegging

In an ideal scenario, a continuous sinusoidal input voltage at the resonance frequency would drive the resoswitch to produce smooth, periodic displacement and output waveforms, as illustrated in Fig. 5.2(a)-(c). In this case, the shuttle displacement waveform reaches its peak at the top of each cycle, impacting the electrode precisely and transferring charge to the load capacitor, C_L , with each contact. This contact is essential as it counteracts the continuous discharge of C_L through R_{bleed} in the circuit shown in Fig. 5.2(a). The resulting waveform across C_L would ideally resemble a steady sawtooth pattern, maintaining the required charge level for consistent output.

However, real-world impacts diverge from this ideal behavior. Due to the nature of the mechanical impact, each collision can introduce slight de-phasing into the shuttle's motion, gradually shifting the phase of the shuttle displacement away from the intended 90° phase shift with respect to the driving force waveform. This shift diminishes the drive efficiency since the shuttle displacement is no longer aligned with the input force sinusoid, causing a decrease in vibration amplitude. As the amplitude reduces, the shuttle may fail to make contact with the output electrodes in subsequent cycles, leading to "missed" impacts where no charge transfer occurs. During this period of reduced contact, the shuttle motion and the driving force waveform gradually realign, restoring the 90° phase difference and allowing energy/charge transfer once again. The result is a cycle of alternating periods of impacting and non-impacting states, producing what is known as "squegging," where impacts occur intermittently rather than in a continuous, predictable pattern, as depicted in the waveform of Fig. 5.2(e).

During squegging, the resoswitch operates at a reduced drive efficiency, limiting the overall bit rate, causing frequency instability and complicating the predictable transfer of charge to C_L . Squegging thus represents an undesired mechanical limitation in resoswitch design, where the balance between force application, phase alignment, and vibration amplitude plays a critical role in maintaining steady performance. This unpredictable impact pattern is a critical challenge in achieving consistent and reliable resoswitch operation and suggests that further design strategies may be necessary to mitigate the phase disturbances introduced by impacts, thereby stabilizing shuttle motion for reliable charge transfer across a range of operating conditions.

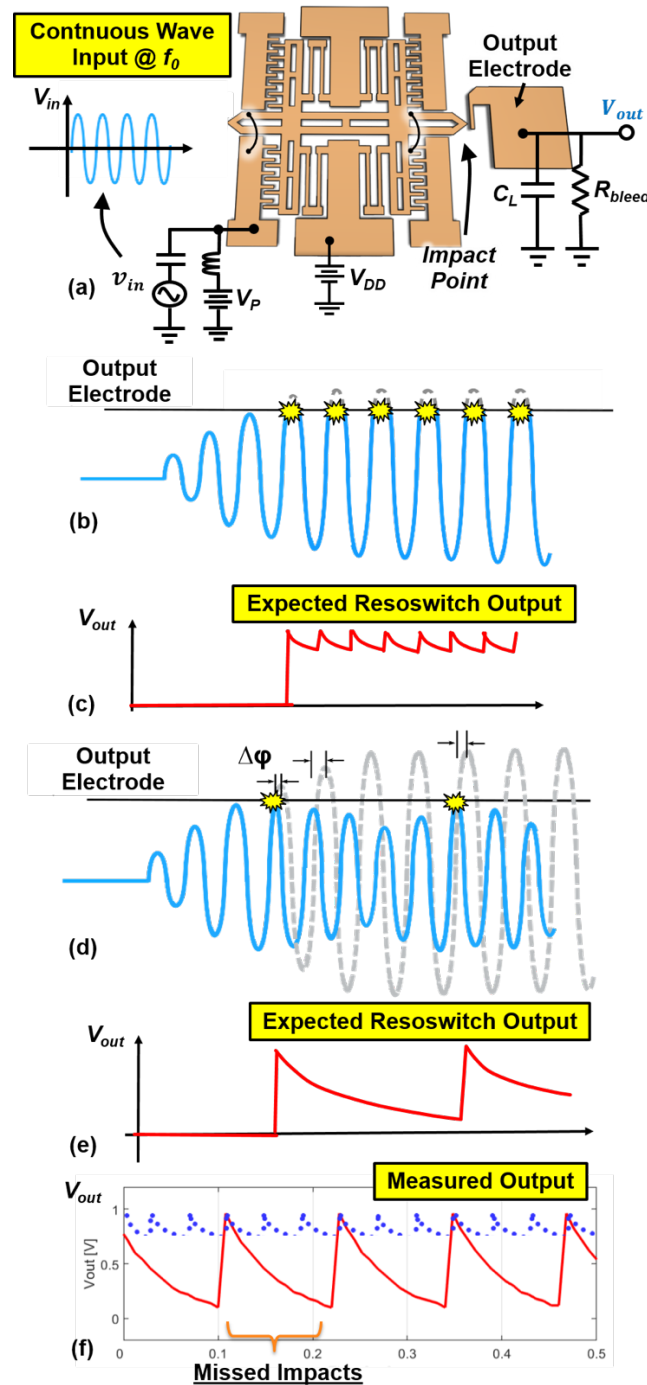


Fig. 5.2: Illustrations depicting one mechanism behind squegging. Here, a continuous wave input at resonance frequency f_0 drives the resoswitch device (a). Ideally, the resoswitch shuttle would impact the output electrode periodically (b) and maintain the 90° phase-shift between displacement and input force needed for efficient drive, generating the output waveform in (c). Unfortunately, impacts introduce phase shifts that pull the displacement and force away from 90° (d), reducing the drive efficiency and causing missed impacts until the phase recovers to restore drive efficiency and induce impacting once again. Less frequent impacts lead to an output waveform with much deeper sawtooths, as depicted in (e) and the measured waveform of (f).

In cases where impacts are missed for only a few cycles, the phenomenon of squegging is relatively benign and does not significantly disrupt the operation of the resoswitch. However, squegging becomes problematic when the phase de-synchronization persists long enough for multiple impacts to be missed, allowing the bleed resistor, R_{bleed} , to steadily discharge the output capacitor, C_L . If this discharge continues for a while, the output voltage will eventually drop below a certain threshold, reaching a level that is interpreted by the output circuit as a logic low. In digital circuits, this unintended low level could trigger an erroneous logic state at the next stage, such as inadvertently switching an inverter output to high. This can lead to errors in data transmission, creating potential vulnerabilities in applications where bit integrity is crucial. In frequency control applications, such as timing and synchronization tasks, prolonged squegging can destabilize the frequency output, leading to errors that disrupts precise timing requirements.

The potential for squegging to undermine the functionality of data and frequency control systems has driven the development of numerous mitigation strategies. These approaches, though varied, aim to suppress squegging at its root, primarily by addressing impact reliability and charge retention. Among the proposed solutions are contact engineering, e.g., soft contacts vs hard contacts, improving long-term performance [21][41][42], as shown in Fig. 5.3. Ensuring device symmetry has also been explored to prevent uneven wear and phase instability [23]. Beyond contact optimization, design refinements such as precise control of the impact gap and careful calibration of input threshold levels have been implemented to improve device robustness across varying operating conditions. However, as demonstrated in Fig. 5.4, even with the integration of contact engineering—where different contact stiffnesses were incorporated in a symmetric comb-drive resoswitch—squegging-induced frequency instability persists. This finding underscores the complexity of squegging and its dependence on multiple interrelated design factors. Despite these advancements, no single solution has proven universally effective in eliminating squegging induced frequency instability across all resoswitch applications.

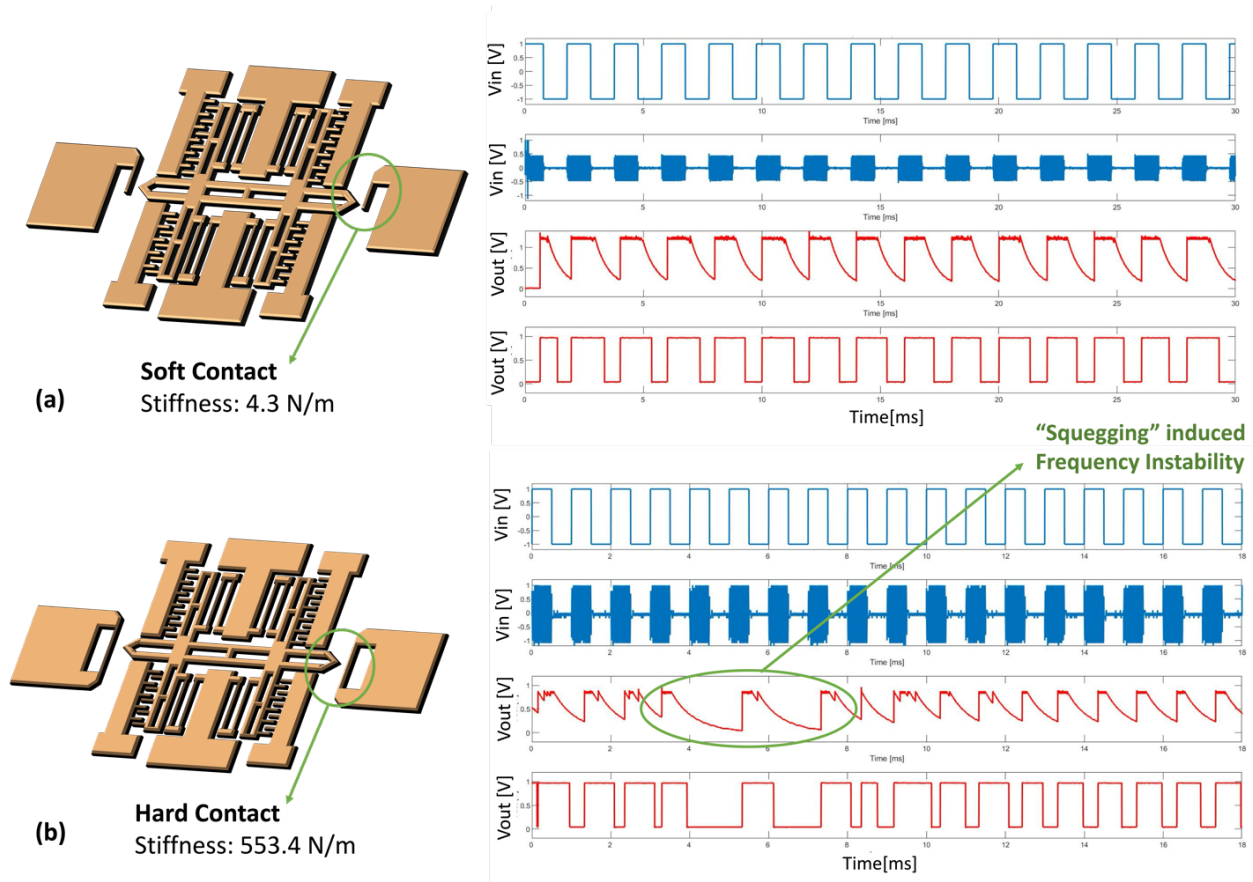


Fig. 5.3: Measured results comparing the performance of resoswitches with soft contact output electrodes (a) and hard contact output electrodes (b). When given an ASK-modulated input signal, the output electrode with higher stiffness exhibits greater frequency instability due to squegging, compared to the soft contact electrode.

An alternative and potentially superior approach recognizes that the core issue in squegging-induced errors is the constant discharge of the output capacitor C_L through the bleed resistor R_{bleed} . In the circuit shown in Fig. 5.2(a), R_{bleed} serves as a continuous sink for charge, pulling the voltage at C_L to ground whenever the shuttle fails to impact the electrode. This setup forces the shuttle to impact regularly to maintain the necessary voltage across C_L , thereby keeping the output signal stable. Consequently, addressing the discharge through R_{bleed} could alleviate squegging by reducing the urgency for consistent impacts, thereby enhancing the resoswitch's operational stability. This insight suggests that eliminating or reducing reliance on the bleed resistor, or implementing alternative charge retention mechanisms, could mitigate the adverse effects of squegging. Further investigation is required to explore how modified circuit designs could balance charge retention with reliable switching performance, potentially opening up new avenues for high-stability, low-error resoswitch applications across diverse fields.

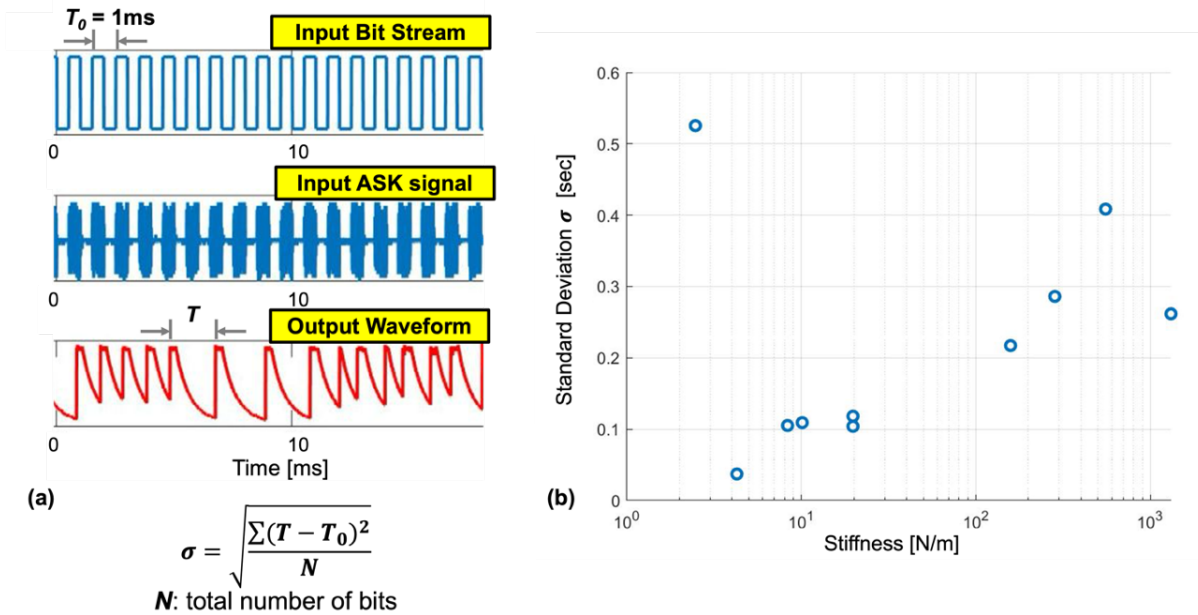


Fig. 5.4: Measurement of frequency instability in resoswitches with varying contact stiffness (*cf.* Fig. 5.3). (a) An input bit stream with ASK-modulated signals at a 1 ms period is applied to the resoswitch, and the corresponding output signal periods are measured. The standard deviation of these periods is then calculated over N input bits. (b) The standard deviation of the output period is plotted as a function of contact stiffness. In the absence of squegging-induced frequency instability, the standard deviation would ideally be zero.

5.2 Push-Pull Receiver Structure and Operation

Fig. 5.5 and 5.6 illustrate the contrasts between the new push-pull FSK receiver topology and the prior single-resoswitch On-Off Keyed (OOK) receiver from [16]. In the push-pull configuration, a key distinction is the use of two separate resoswitches: one functions as the “pull-up” switch with its shuttle tied to the supply voltage, V_{DD} , while the other functions as the “pull-down” switch with its shuttle connected to ground. This dual-resoswitch arrangement enables efficient bidirectional control over the output capacitor, C_L , by alternating which resoswitch impacts the capacitor at a given time. When the pull-up resoswitch engages, it creates a conductive path from V_{DD} to C_L , charging it up in a manner reminiscent of a PMOS transistor in a CMOS inverter. Conversely, when the pull-down resoswitch impacts, it discharges C_L to ground, effectively pulling the output voltage to zero.

The resemblance to a static CMOS inverter is particularly significant because the push-pull resoswitch configuration achieves efficiency by ensuring that the pull-up and pull-down devices do not activate simultaneously. Unlike CMOS circuits, where overlapping conduction periods (both PMOS and NMOS devices turning on briefly during switching) can result in unwanted power loss and reduced efficiency, the resoswitch design sidesteps this issue entirely. This is due to the frequency-selective nature of the resoswitches, where each switch is resonant at a distinct frequency. By carefully tuning these resonance frequencies, the circuit creates a natural “buffer zone” that ensures only one resoswitch is active at any given time, depending

on the input frequency. This frequency-based separation is easier to manage in resoswitches than in conventional CMOS, making the push-pull topology inherently more efficient.

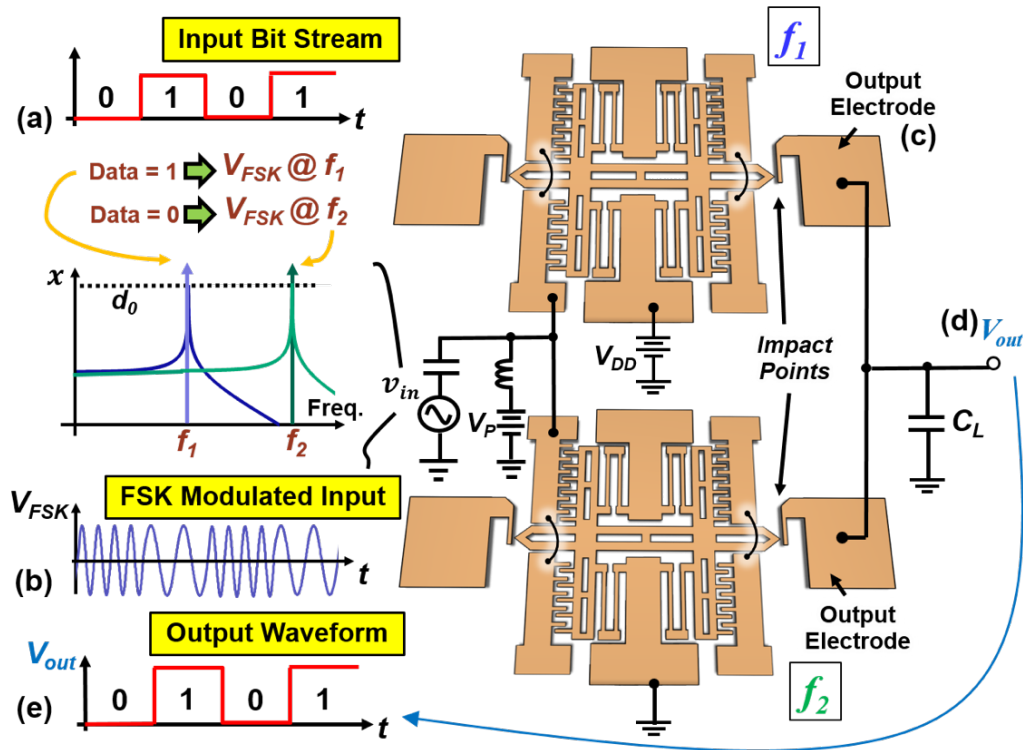


Fig. 5.5: Illustrative summary of a push-pull all-mechanical zero quiescent power FSK receiver. Here, the (a) input bit stream is (b) FSK-modulated into an off-resonance signal to represent a ‘0’ or an on-resonance signal to denote a ‘1’. Reception of a ‘1’ at the input electrode induces resonance vibration of the top structure, in turn instigating impacting of the shuttle to the output electrode at (c). Impacting then periodically transfers charge from V_{DD} to the output load capacitor (d) C_L , eventually charging it to V_{DD} , which corresponds to a ‘1’. Any ‘0’ input received afterwards stops resonant impacting of the top resonator and instigates it in the bottom one, which impacts to connect the output node to ground, allowing C_L to discharge to ground, denoting a ‘0’. In this way, the input bit stream is faithfully reproduced at the output, as shown in (e).

In previous OOK configurations, like that in Fig. 5.6, the single resoswitch was combined with a bleed resistor, R_{bleed} , which was necessary to discharge C_L in the absence of a pull-down resoswitch. However, this design presented challenges: the resoswitch would have to compete with R_{bleed} , which constantly pulls the voltage down and leads to errors and frequency instability due to squegging. In contrast, the push-pull configuration removes R_{bleed} by decoupling the charging and discharging functions into separate devices, allowing each to operate unimpeded. Without R_{bleed} , the new topology achieves “brick wall” transitions on the output signal, meaning that each switching action fully and cleanly transitions C_L from high to low or low to high, without partial discharges or residual charges left on the capacitor.

Perhaps most importantly, since there is no bleed resistor constantly pulling the voltage down, any squegging events (i.e., missed impacts) have no consequence. The circuit is ideally immune to squegging, unlike the circuit of Fig. 5.2, where the measured output in Fig. 5.2 (d)-

(f) shows how a squegging event can introduce an extra output transition, which then shifts the frequency, causing instability.

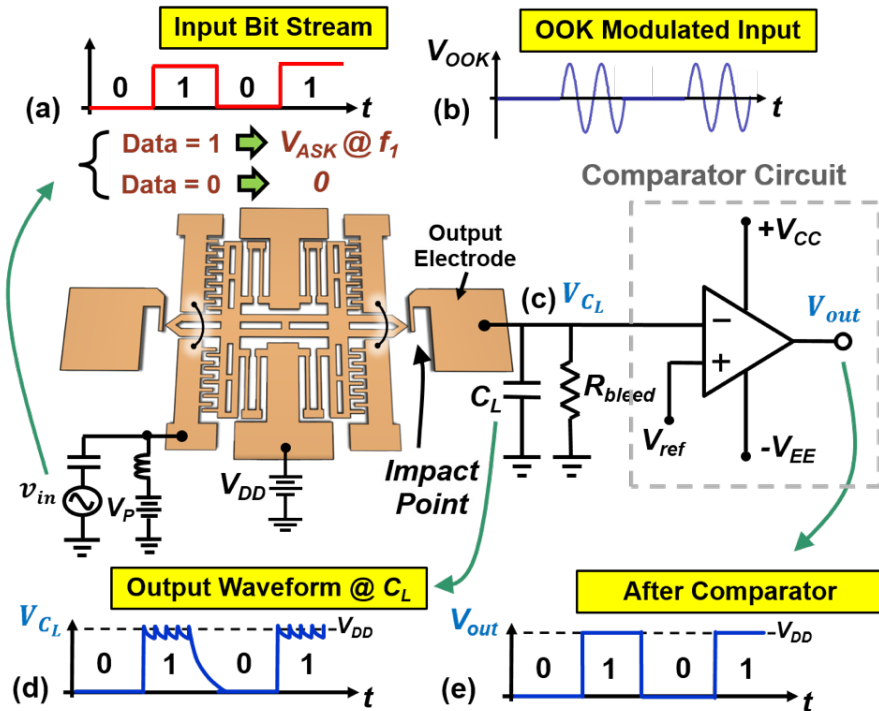


Fig. 5.6: Illustrative summary of a low-frequency all-mechanical zero quiescent power OOK receiver. Here, the (a) input bit stream comprises a (b) OOK-modulated on-resonance carrier signal that drives the device into resonance vibration, instigating shuttle-to-electrode impacts during “on” periods that then charge (c) C_L to deliver a (d) output high. During “off” periods, the resoswitch does not move, so does not impact the output, allowing bleed resistor R_{bleed} to discharge C_L to 0V (i.e., output low). Constant current bleed by R_{bleed} becomes problematic from both stability and processing power consumption perspectives.

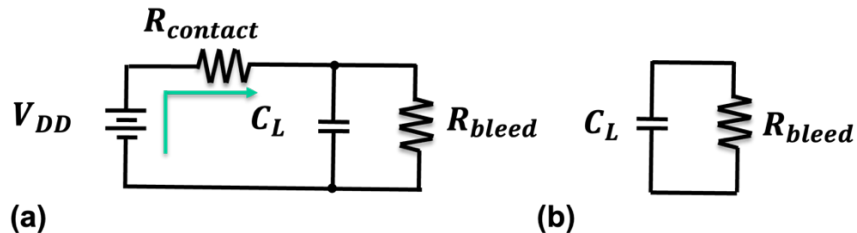


Fig. 5.7: Equivalent circuits of a single resoswitch receiver. (a) When the resoswitch shuttle makes contact with the output electrodes at input “1.” (b) When the resoswitch does not make contact, causing the charge on C_L to dissipate through the bleed resistor.

In terms of power consumption, the energy usage of a single resoswitch receiver during operation is given by the following expression [17]:

$$P = C_L V_{DD}^2 f_{switch} + \frac{V_{DD}^2}{2R_{bleed}} \quad (\text{Eq. 49})$$

where C_L is the load capacitance, V_{DD} is the supply voltage, R_{bleed} is the bleed resistance, and f_{switch} is the desired switching frequency of the receiver, as shown in Fig. 5.7.

For an off-chip load capacitance of 3 pF, a bleed resistance of 100 M Ω , a supply voltage of 1 V, and a switching frequency of 1 kHz, the resulting power consumption is approximately 8 nW.

However, in the case of a push-pull resoswitch receiver, which operates without the need for R_{bleed} , the power consumption simplifies to:

$$P = C_L V_{DD}^2 f_{switch} \quad (\text{Eq. 50})$$

Under the same conditions of C_L , V_{DD} , and f_{switch} , this reduces the power consumption to 3 nW. Additionally, a push-pull receiver has the advantage of potentially utilizing its own output electrode as an on-chip load capacitance, which is significantly smaller than off-chip capacitance. For instance, with an on-chip capacitance of just 2 fF, the power consumption drops dramatically to only 2 pW. This highlights the significant energy efficiency benefits of the push-pull resoswitch receiver architecture.

Moreover, the push-pull arrangement delivers significant advantages in efficiency and output fidelity, ensuring that each transition is sharp and unambiguous—characteristics essential for accurate FSK demodulation. Moreover, because the push-pull topology achieves these transitions without needing a comparator (as used in the OOK configuration), the design complexity is reduced, further enhancing the system’s robustness and reliability. This simplification not only minimizes the number of components but also removes potential points of failure, which is especially valuable in applications where reliability and power efficiency are paramount, such as in IoT networks or other battery-constrained environments.

5.3 Experimental Results

Fig. 5.1 presents the SEM of an all-gold resoswitch used in this work, fabricated using the process summarized in Fig. 5.6 that replaces the oxide mold of [13] with a simpler photoresist mold. Two such devices were inserted into a 10 mTorr Lakeshore FWPX Vacuum Probe Station and hooked into a circuit like that of Fig. 5.5, with ports to an outside function generator and oscilloscope that apply inputs and measure performance, respectively. For comparison, the single-device circuit of Fig. 5.6 was also constructed and measured.

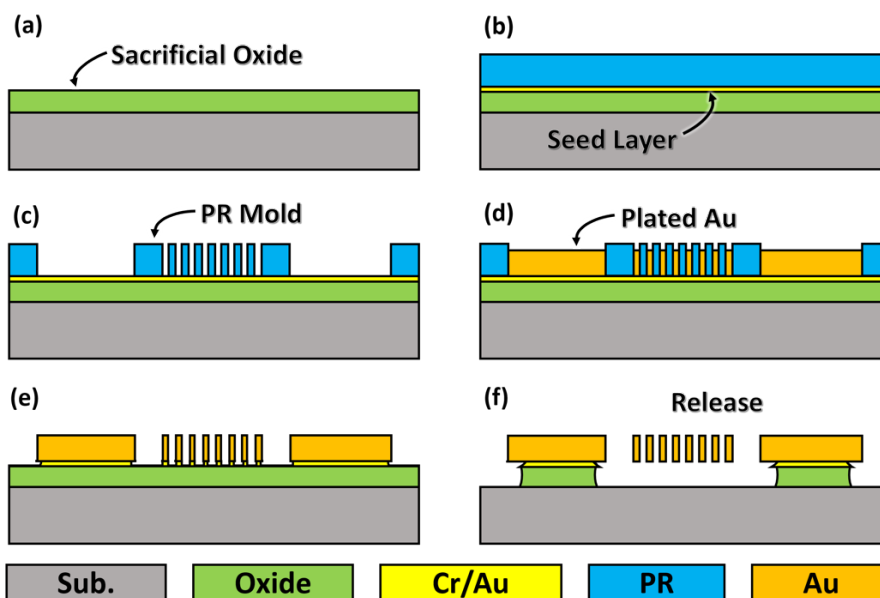


Fig. 5.8: One-mask gold resoswitch fabrication process that starts with (a) deposition of sacrificial oxide onto a blank silicon wafer using LPCVD, then (b) sputter deposition of Cr/Au to promote adhesion between oxide and gold and serve as an electroplating seed layer. A thick layer of photoresist is then deposited and patterned to form a mold with cross-section as in (c), after which gold electroplating through the mold in a cyanide-based solution forms the structure in (d). Removal of the photoresist mold to yield (e) and a release in vapor-phase HF yields the final suspended movable structure cross-section in (f).

Fig. 5.9 and Fig. 5.10 plot measured data for the Fig. 5.6 and Fig. 5.5 circuits, respectively. Here, the resoswitch activating input frequencies are 22.85 kHz and 25.21 kHz for the pull-up and pull-down devices, respectively, which also correspond to the mark and space frequencies of the FSK input. Immediately discernible are the sharp, brick-wall output transitions across C_L (before any comparator, in this case flip-flop, amplification) of the push-pull circuit relative to the Fig. 5.6 single-device circuit before the comparator. The former's C_L voltage V_{CL} waveform is also much smoother than the single-device one, which suffers from continuous current bleed that causes jagged tops, as well as a squegging-induced deep dive leading to an unwanted transition at the flip-flop output that contributes to frequency instability.

Meanwhile, if any squegging were present in the push-pull circuit of Fig. 5.5, it does not manifest in the output signals shown in Fig. 5.10, indicating that the push-pull configuration provides a robust defense against squegging effects. This lack of squegging artifacts in Fig. 5.10 highlights one of the push-pull circuit's primary advantages: its inherent immunity to squegging.

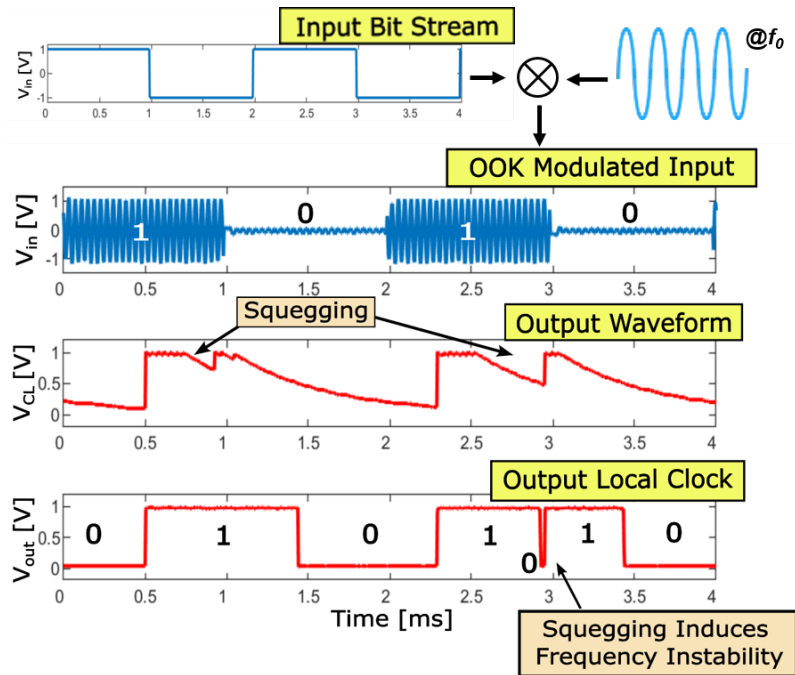


Fig. 5.9: Measured OOK input, C_L output, and comparator output waveforms for the single-device circuit of Fig. 5.6 followed by a comparator (amplifier), as in [39]. (V_{CL} is the voltage across C_L , while V_{CLK} is the output of the comparator.) Here, squegging induces a deep drop in V_{CL} around 3 ms that then causes the comparator output V_{CLK} to switch in error.

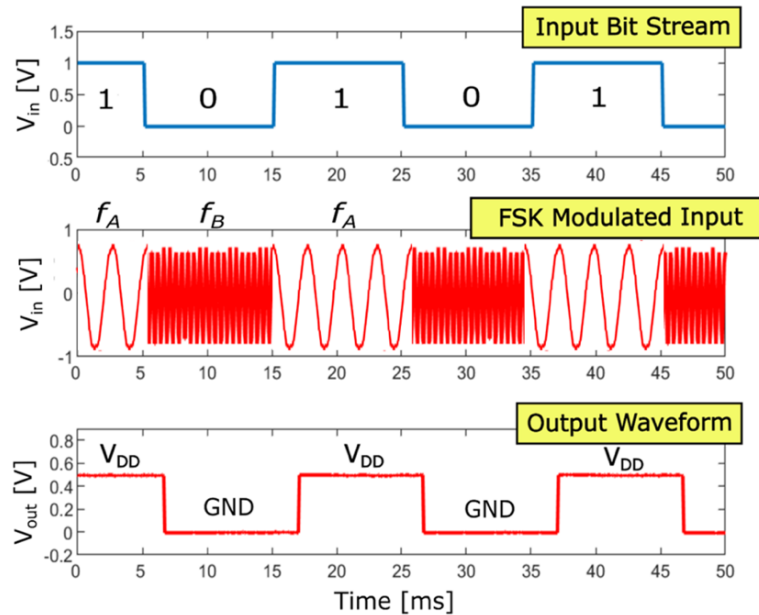


Fig. 5.10: Measured FSK input and practically perfect output (despite possible squegging) of the push-pull reswitch receiver of Fig. 5.5. No comparator is needed here to achieve the “brick wall” output waveform.

5.4 Challenges Encountered During Measurements

During the evaluation of push-pull resoswitch receivers, an unexpected issue was observed: in certain cases, both the top and bottom resoswitches (as illustrated in Fig. 5.5) were simultaneously "ON" for a valid input of either "1" or "0," as shown in Fig. 5.11(b). Ideally, only one resoswitch should be active at a time, impacting the output electrodes accordingly. The simultaneous activation of both devices introduces ambiguity in the output state, making it uncontrollable and leading to potential errors.

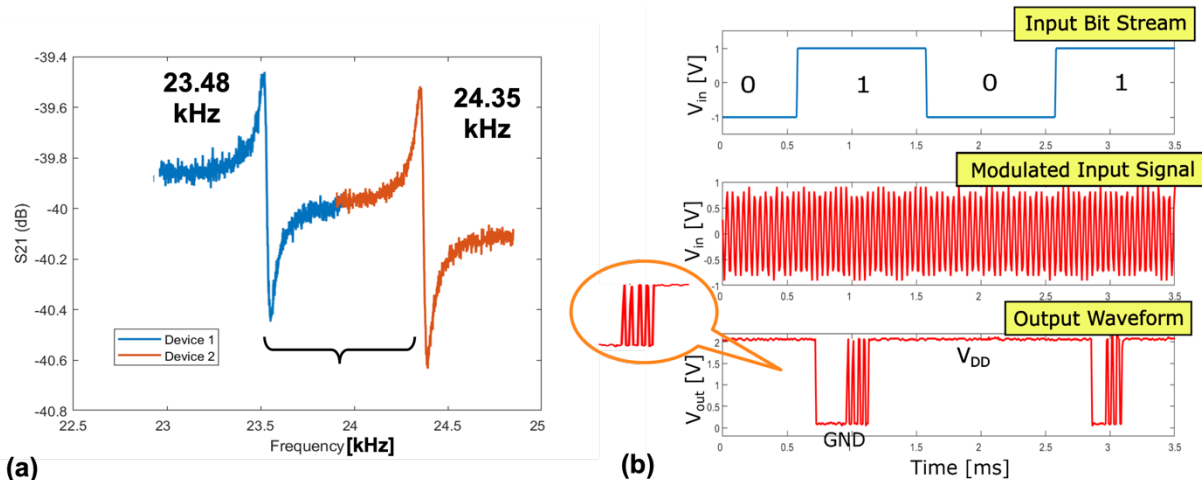


Fig. 5.11: Illustration of the simultaneous activation ("both ON" condition) in a push-pull resoswitch receiver. (a) Resonance frequencies of the top and bottom resoswitches used in the measurements. (b) Measured output waveforms with an FSK-modulated input signal, showing distinct "spikes" in the output. These spikes result from both resoswitches activating simultaneously—where the top resoswitch charges the output electrode to V_{DD} while the bottom resoswitch discharges it within the same cycle.

The primary cause of this issue appears to be the small frequency separation between the resonance modes of the two resoswitches (as shown in Fig. 5.11(a)), combined with their limited quality factor (Q). A lower Q -factor results in a broader 3-dB bandwidth, effectively widening the passband of each resoswitch. If the passbands of the top and bottom resoswitches in the push-pull receiver overlap, any input signal within this overlapping region can activate both devices simultaneously.

To mitigate this issue, two potential solutions can be explored:

1) *Increasing the Frequency Separation:*

Designing the resoswitches with a larger resonance frequency difference can help minimize passband overlap and reduce the likelihood of both devices turning "ON" simultaneously.

2) *Enhancing the Q -Factor:*

Improving the Q -factor through design optimization and material selection can narrow the passband, thereby reducing overlap and ensuring more precise frequency selectivity.

The inherent nonlinearity of resoswitches can contribute to passband widening, increasing the likelihood of overlap between the passbands of individual devices and causing both resoswitches to turn “ON” simultaneously. This nonlinearity, known as the Duffing effect, arises due to the dependence of the restoring force on higher-order displacement terms rather than strictly following Hooke’s Law ($F = kx$) [43]. The Duffing effect is strongly influenced by the input driving power (or driving force) applied to the resoswitches, leading to amplitude-dependent frequency shifts and a widened passband in MEMS resonators.

As illustrated in Fig. 5.12, increasing the input power—effectively increasing the driving force—results in a broader passband for resoswitch receivers. In a push-pull configuration, this passband widening exacerbates the risk of overlap between the top and bottom resoswitches, potentially leading to erroneous output signals. To mitigate this issue, precise control of the Duffing effect is necessary. One possible approach is to regulate the DC bias voltages applied in push-pull receivers, thereby limiting the extent of nonlinearity-induced passband expansion. Further investigation into optimal biasing strategies is required to enhance the stability and reliability of push-pull resoswitch receivers.

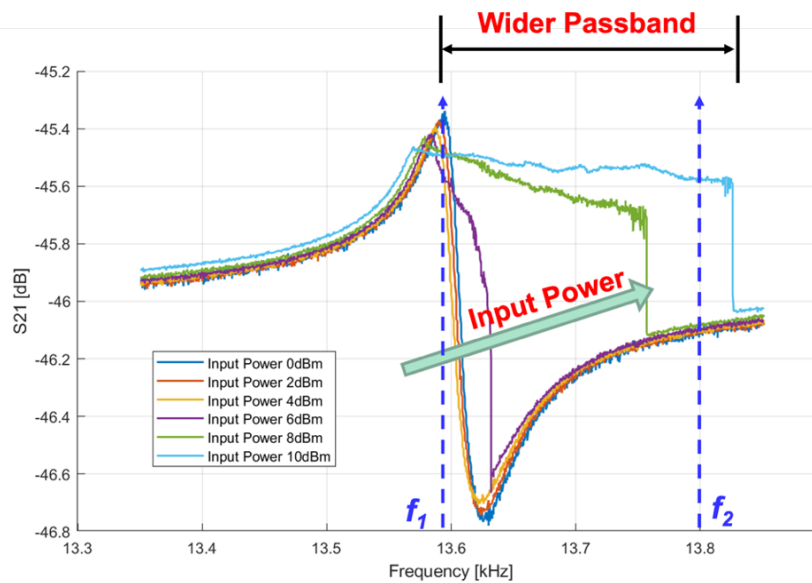


Fig. 5.12: Illustration of the Duffing effect in resoswitch receivers. As the input power increases, the resonance peak broadens, resulting in an expanded passband.

5.5 Conclusion

In addressing the challenge of squegging, the demonstrated push-pull circuit provides a comprehensive solution to one of the most significant limitations in all-mechanical resoswitch receiver technology: the issue of reliability and bit error rate. By effectively mitigating the effects brought by squegging, this circuit design ensures consistent and stable impacts, which in turn significantly reduces frequency instability during signal reception. This stability improvement allows for enhanced communication efficiency and robustness, paving the way for resoswitch receivers to support full Frequency Shift Keying (FSK) operation. Such

operation greatly extends the versatility and performance of these devices in real-world applications, where maintaining data integrity and communication consistency is crucial.

The advances achieved with the push-pull circuit, in combination with recent breakthroughs in bit rate enhancement, represent a major step forward in making all-mechanical resoswitch receivers viable for commercial applications. This progress is particularly relevant for deployment in environments that are unfavorable for traditional CMOS transistors, such as high-temperature or radiation-intensive settings, where mechanical components offer inherent advantages over electronic counterparts.

Furthermore, the resoswitch's inherent ultra-low power characteristics align well with the stringent power requirements of modern sensor networks, especially in remote or inaccessible locations where battery replacement is impractical. By virtually eliminating power consumption in standby modes, these devices dramatically reduce battery drain, offering a sustainable solution that supports long-term deployment without frequent maintenance. This energy efficiency, combined with enhanced reliability, positions resoswitch receivers as promising candidates for the next generation of Internet of Things (IoT) devices, wireless sensor networks, and communication systems where energy constraints and environmental durability are paramount.

In conclusion, the push-pull circuit innovation is a transformative advancement that addresses the core technical challenges facing all-mechanical resoswitch receivers, including bit error rates and squegging-induced instability. As this technology moves closer to commercialization, it opens up new possibilities for durable, low-power, and high-reliability communication systems that can operate in challenging environments while delivering stable, long-lasting performance. Future research and development will further refine these designs, enabling the integration of all-mechanical resoswitch technology into a broader range of applications, ultimately advancing the field of ultra-low-power wireless communication and extending the lifespan and functionality of sensor networks globally.

Chapter 6

Conclusions

This thesis presents a comprehensive development and evaluation of all mechanical communication receiver, resoswitch, as a promising alternative to traditional transistor-based components in wireless communication systems. Unlike conventional receivers, which rely heavily on transistors for signal amplification and switching, resoswitches rely on mechanical resonance to drastically reduce power consumption by consuming zero power when in standby until they detect a valid input at their resonance frequency. This ability to operate in an always-on mode with extremely low power consumption establishes resoswitches as a pioneering solution for some IoT applications. These devices show potential in a variety of energy-sensitive domains, including remote sensing, RFID tagging, environmental monitoring, and other wireless communication applications where minimal energy usage and constant readiness are essential.

The resoswitch receiver, with its unique structure and operating principles, introduces a new paradigm in low-power communication technology, particularly in applications that do not demand high data rate but instead benefit from constant availability. This thesis presents the practical capabilities of micromechanical resoswitches, demonstrates their ability in receiving low-power signals wirelessly and successfully demodulating on-off keyed (OOK) signals. This work also explores the use of ferrite-rod antennas to drive these receivers, illustrating the essential design and implementation challenges encountered with impedance matching, frequency tuning, and bandwidth constraints—critical factors that must be addressed for successful deployment of resoswitch technology in real-world communication systems.

Through careful design, fabrication, and experimental testing, this research has pushed the performance boundaries of micromechanical resonators, offering valuable insights into their application in wireless systems, particularly for low-bit-rate, low-power communication. Notably, the implementation of the push-pull resoswitch receiver architecture in this work presents a significant innovation that enhances both the efficiency and reliability of the resoswitch as a communication receiver. This push-pull configuration enables more stable operation by eliminating frequency instability caused by the "squegging" phenomenon, a condition that can lead to errors and frequency instability in single-ended resoswitch designs. The push-pull receiver not only improves the accuracy and stability of received signals but

also enables full FSK demodulation, further increasing its robustness and adaptability in challenging environments.

The findings underscore both the advantages and the limitations of resoswitch technology in comparison to traditional electronic components. While resoswitches do not yet match electronic devices in terms of data rates or efficiency at large bandwidths, they offer unique benefits in terms of energy efficiency and adaptability, especially for applications where conserving power is critical. Their passive listening capability—enabled by their reliance on mechanical resonance for signal detection—allows for operation with zero standby power, eliminating the need for power-hungry sleep-wake cycles typical in conventional electronics. As a result, resoswitches stand out as compelling solutions for energy-constrained applications, making them ideal candidates for low-power, always-on sensing in fields like remote monitoring, environmental tracking, and RFID.

6.1 Future Research Directions

As mentioned in this thesis, resoswitches face several unresolved challenges that require further research and development:

1) *Improved Device Matching and Design Optimization:*

The impedance mismatch between the resoswitch and the antenna, while partly addressed, remains a bottleneck. Future work could explore new designs and advanced fabrication techniques that make the resoswitch's motional resistance closer to that of practical antennas.

2) *Antenna Co-Design for Broader Bandwidth:*

The antenna setup in this work was constrained by its need for extensive tuning to match the resoswitch frequency. Designing antennas that operate natively at the target frequency would increase bandwidth and, consequently, the achievable data rates of the resoswitch receiver. Such co-design could also open possibilities for resoswitch applications in higher-frequency bands, supporting faster data transmission and new application areas.

3) *New Designs of Ru-based Resoswitch:*

Despite the challenges faced during the fabrication of Ru-based resoswitches, the material's advantages still make it an attractive option for future development. One of the key issues encountered is the limitation in the achievable thickness of Ru deposits, whether through sputtering, evaporation, or electroplating. The maximum thickness achieved so far is under 300 nm, which is significantly below the required thickness for proper operation of the comb-driven resoswitch. To address this limitation, two potential approaches can be explored: optimizing the deposition process to increase the Ru layer thickness or redesigning the resoswitch structure to function effectively with thinner layers. Further investigations into both avenues could lead to viable solutions, paving the way for more reliable and efficient Ru-based resoswitches.

4) *Push for Real-World Deployment:*

Developing resoswitch receivers for commercial and industrial environments requires additional testing in various environmental conditions, such as various temperatures, vibrations, and electromagnetic interferences. Field trials would validate resoswitch durability and robustness, establishing their reliability for practical use.

6.2 Possible New Design: Ru CC Beam Resoswitch

The advantages of Ru resoswitch over gold have been discussed in Section 2.4, but the limited thickness (less than 300nm) we can achieve so far are not enough for comb-driven resoswitch to function correctly. Other than optimizing the deposition recipe to get a thicker structure, we can also explore new designs that could function well with thin structure. Clamped-clamped (CC) beam made with Ru with thickness of 45 nm has been successfully demonstrated [30], so the use of Ru CC-beam as resoswitch becomes possible.

6.2.1 Clamped-Clamped Beam Ru Resoswitch

The design of clamped-clamped (CC) beams as resoswitches integrates the concept of a displacement amplifier [44], which includes the use of coupling beams. The fundamental analysis of CC beams is based on Timoshenko beam theory [45], which provides the relationship for beam length and other parameters as follows:

$$\tan \frac{\beta}{2} + \frac{\beta}{\alpha} \left(\frac{\alpha^2 + g^2 \left(\frac{\kappa G}{E} \right)}{\beta^2 - g^2 \left(\frac{\kappa G}{E} \right)} \right) \tanh \frac{\alpha}{2} = 0, \quad (\text{Eq. 51})$$

where:

$$g^2 = \omega_{nom}^2 L_r^2 \left(\frac{\rho}{E} \right) \quad (\text{Eq. 52})$$

and:

$$\left. \begin{matrix} \alpha^2 \\ \beta^2 \end{matrix} \right\} = \frac{g^2}{2} \left[\mp \left(1 + \frac{E}{\kappa G} \right) + \sqrt{\left(1 - \frac{E}{\kappa G} \right)^2 + \frac{4L_r^2 h W_r}{g^2 I_r}} \right], \quad (\text{Eq. 53})$$

where $I_r = \frac{1}{12} W_r h^3$ is the moment of inertia of the beam.

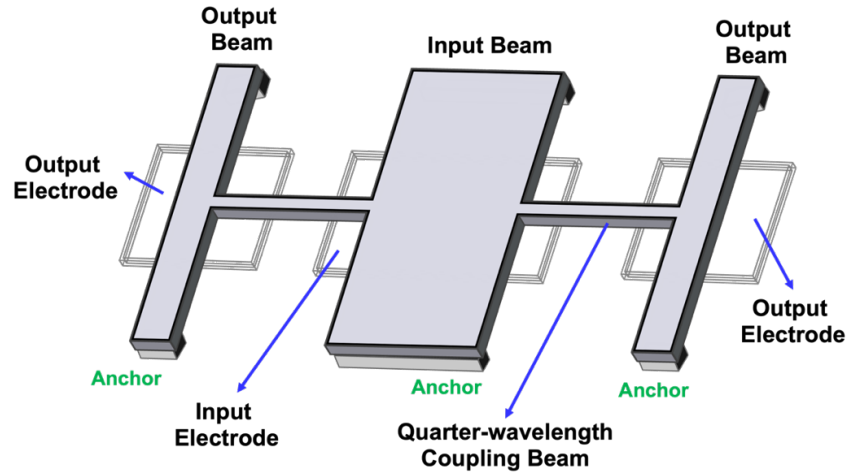


Fig. 6.1: Schematic illustration of the Clamped-Clamped (CC) beam resoswitch, featuring a central input beam and two symmetric output beams positioned on either side. The symmetric design enhances the overall performance of the resoswitch by reducing losses and minimizing the likelihood of squegging.

Given a predetermined width and thickness for the beam, the required CC beam length at the desired resonant frequency ω_{nom} can be calculated using Timoshenko beam theory. It is important to note that the width of the beam does not affect its resonance frequency. Specifically, for beams with the same length and thickness, increasing the width results in a proportional increase in stiffness, as shown in Eq. 54-57 from Table V. This characteristic allows us to maintain the same resonance frequency by adjusting the length or thickness while modifying the width for structural stiffness.

Additionally, symmetry plays a crucial role in enhancing resoswitch performance, reducing losses and minimizing the likelihood of undesirable phenomena such as squegging [21]. Therefore, in this design, we employ a symmetric configuration with two output beams positioned on either side of the central input beam, as shown in Fig. 6.1.

Table V shows parameters and corresponding equations for 10MHz CC beam resoswitches with gain $\sqrt{2}$ and 2, respectively.

In previous displacement amplifier designs, two asymmetric resonator arrays (disk resonators) are coupled by a quarter-wavelength beam, which allows the specification of the gain factor through the ratio of resonators in the input and output arrays [44]. Displacement amplification occurs because the quarter-wavelength coupling beam constrains the mechanical circuit, equalizing the energy on both sides.

For the CC-beam resonator, the energy stored can be expressed as:

$$E = \frac{1}{2}kx^2 \quad (\text{Eq. 58})$$

Where k is the stiffness of the beam, which is defined in Table V, and x is the maximum displacement. The two beams, coupled by the quarter-wavelength beam, must satisfy the energy balance:

$$\frac{1}{2}k_{in}x_{in}^2 = \frac{1}{2}k_{out}x_{out}^2 \quad (\text{Eq. 59})$$

To achieve a displacement gain $G=x_{out}/x_{in}$, the stiffness of the input and output beams must satisfy:

$$k_{in} = k_{out} \cdot G^2 \quad (\text{Eq. 60})$$

Table V: Clamped-Clamped Beam Resoswitch Design Summary with Equations

Parameters	Source	Design 1	Design 2	Unit
Gain	Spec.	$\sqrt{2}$	2	---
Frequency	Spec.	10	10	MHz
Material	Spec.	Ru	Ru	---
Young's Modulus	Spec.	424	424	GPa
Density	Spec.	12300	12300	kg/m ³
Input Beam				
Length	Calculated	5.211	5.211	μm
Width	Spec.	4	4	μm
Thickness	Spec./Process	45	45	nm
Output Beam				
Length	Calculated	5.211	5.211	μm
Width	Spec.	1	0.5	μm
Thickness	Spec./Process	45	45	nm
Coupling Beam				
Length	Calculated	2.61	2.61	μm
Width	Spec.	0.3	0.3	μm
Thickness	Spec./Process	45	45	nm
Coupling Location	Spec.	Center	Center	---
Design Equations				
Beam Displacement	$X_{mode}(y) = \zeta[\cos(ky) - \cosh(ky)] + [\sin(ky) - \sinh(ky)]$ $k = 4.730/L_r, \zeta = -1.01781.$			(Eq. 54)
Equivalent Mass	$m_r(y) = \frac{\rho \cdot W_r \cdot h}{[X_{mode}(y)]^2} \int_0^{L_r} [X_{mode}(y')]^2 dy'$ $= 1.036L_r \frac{\rho \cdot W_r \cdot h}{[X_{mode}(y)]^2}$ $m_{re} = m_r(L_r/2) = 0.3965(\rho \cdot W_r \cdot L_r \cdot h)$			(Eq. 55)
Equivalent Stiffness	$k_{re} = \omega_{nom}^2 \cdot m_{re}$			(Eq. 56)
Equivalent Damping	$c_{re} = \omega_{nom} m_{re} / Q$			(Eq. 57)

Finally, beams vibrating in flexural or torsional modes can be modeled using transmission line theory [46]. The flexural mode is described by the following equation:

$$\begin{bmatrix} f_1 \\ \dot{x}_1 \end{bmatrix} = \begin{bmatrix} \frac{H_6}{H_7} & -\frac{2EI_S\alpha^3 H_1}{j\omega L_S^3 H_7} \\ -\frac{j\omega L_S^3 H_3}{EI_S\alpha^3 H_7} & \frac{H_6}{H_7} \end{bmatrix} \begin{bmatrix} f_2 \\ \dot{x}_2 \end{bmatrix} \quad (\text{Eq. 61})$$

$$\alpha^4 = L_S^4 \left(\frac{\rho W_S h \omega^2}{EI_S} \right) \quad (\text{Eq. 62})$$

$$I_S = \frac{1}{12} W_S h^3 \quad (\text{Eq. 63})$$

where $H_1 = \sinh \alpha \cdot \sin \alpha$, $H_3 = \cosh \alpha \cdot \cos \alpha - 1$, $H_6 = \sinh \alpha \cdot \cos \alpha + \cosh \alpha \cdot \sin \alpha$, and $H_7 = \sinh \alpha + \sin \alpha$. L_S , W_S and h are the length, width and thickness of the coupling beam, respectively. In analogy to electromagnetic transmission lines, the main diagonal elements of the matrix will be zero at the quarter-wavelength equivalent length. This condition requires $H_6 = 0$, and the solutions to this equation correspond to values of α and the coupling length L_S that are equivalent to a quarter-wavelength. Excluding the trivial solution (zero), the first, second, and third non-zero solutions of this equation give the corresponding coupling lengths for $\lambda/4$, $3\lambda/4$, and $5\lambda/4$, respectively.

$$H_6 = \sinh \alpha \cdot \cos \alpha + \cosh \alpha \cdot \sin \alpha = 0 \rightarrow \alpha = 0, 2.365, 5.498, 8.639, \dots \quad (\text{Eq. 64})$$

6.2.2 Simulation

Simulations of Design 1 and Design 2, as shown in Table V, were performed using COMSOL to determine the resonance frequencies and beam displacements, with results presented in Fig. 6.2. The simulation results in Fig. 6.2 illustrate the displacement variations at resonance frequencies. As expected, the output beam exhibits a larger displacement compared to the input beam for both the gain $\sqrt{2}$ and gain 2 designs.

However, the wide input beam required for achieving a large displacement gain may pose challenges during fabrication [47]. Specifically, the etchant might struggle to reach underneath the beam to etch away the sacrificial layer during the release process. To address this issue, we propose dividing the wide input beam into multiple narrower CC beams, each coupled with very short coupling beams (significantly smaller than standard half-wavelength coupling beams), as shown in Fig. 6.3. The separated beams, coupled by short coupling beams, can be treated as a single unit with an equivalent beam width equal to the sum of the individual beam widths. Simulations of this modified design were also performed, with results plotted in Fig. 6.4, showing that similar displacement amplification and the desired gain can be achieved as with the original wide beam design.

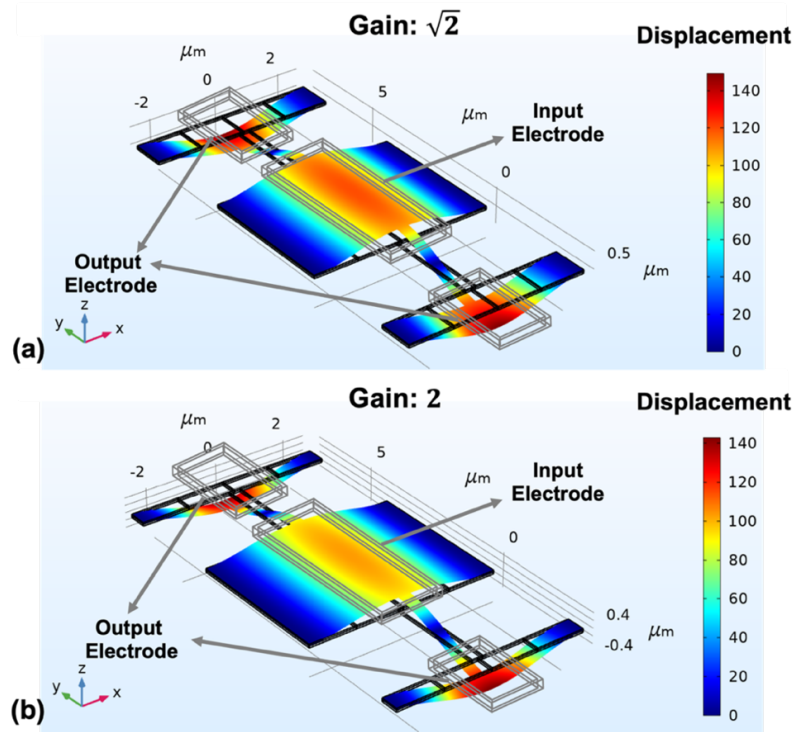


Fig. 6.2: (a) COMSOL simulation of the CC-beam Ru Resoswitch demonstrating a displacement gain of $\sqrt{2}$, where the output beam displacement is $\sqrt{2}$ times greater than that of the input beam. (b) COMSOL simulation of the CC-beam Ru Resoswitch with a displacement gain of 2, showing the output beam displacement to be approximately twice that of the input beam.

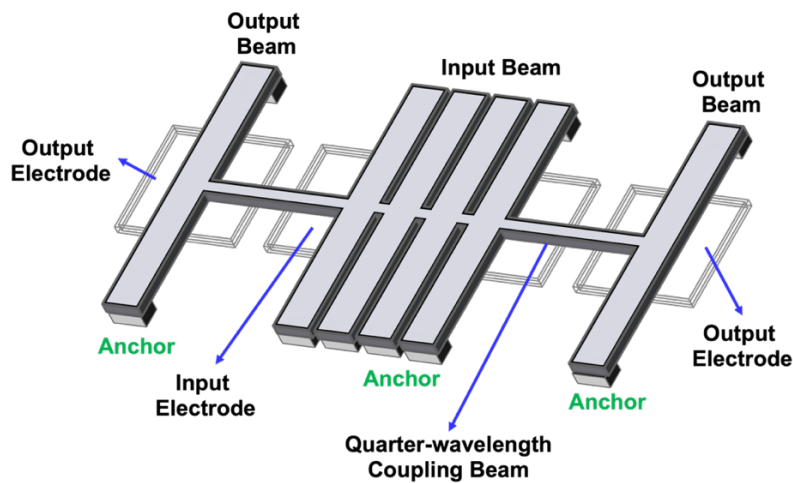


Fig. 6.3: Schematic illustration of the Clamped-Clamped (CC) beam resoswitch design featuring separated input beams connected by very short coupling beams. This design is intended to address potential fabrication challenges associated with wide input beams, such as difficulties in fully etching the sacrificial layer beneath the structure. By dividing the input beam into narrower segments and coupling them, the design maintains equivalent performance to the wide beam configuration while improving manufacturability. The separated input beams are expected to exhibit similar displacement amplification and mechanical behavior as the original wide beam design, making this approach a practical alternative for achieving comparable functionality.

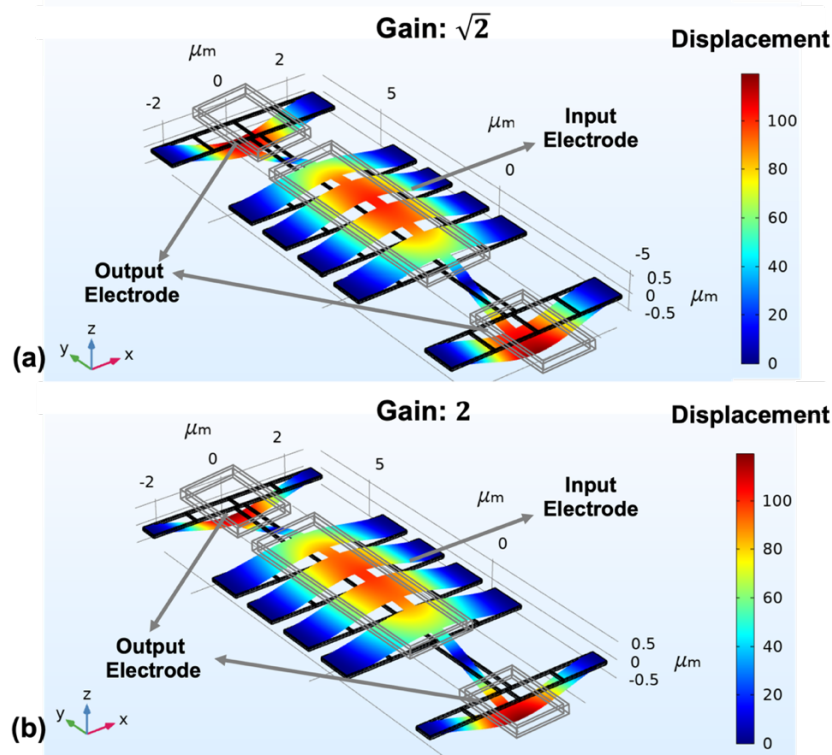


Fig. 6.4: (a) COMSOL simulation of the CC-beam Ru Resoswitch with separated input beams illustrating a displacement gain of $\sqrt{2}$, where the output beam displacement is $\sqrt{2}$ times greater than that of the input beam. (b) COMSOL simulation of the CC-beam Ru Resoswitch with a displacement gain of 2, showing the output beam displacement to be approximately twice that of the input beam. The separated input beams, connected by very short coupling beams, effectively function as a displacement amplifier.

6.3 Concluding Remarks

This thesis explores the innovative potential of resoswitches in the realm of low-power wireless communication. By offering a transistor-free, passive mechanism for signal reception, resoswitches present an attractive solution for ultra-low-power applications. These devices only consume power upon receiving valid signals, making them ideal for energy-constrained environments such as the Internet of Things (IoT), where devices must remain active over extended periods without draining power sources.

As wireless communication and sensing technologies continue to expand, there is an increasing need for energy-efficient systems that can operate autonomously for long durations. In this context, resoswitches stand out as a promising alternative to conventional active devices, paving the way for sustainable, long-lasting communication systems. Despite being in the early stages of development, this work has provided crucial insights into the operational principles and performance characteristics of resoswitches.

Throughout this thesis, significant advancements have been made in understanding the fabrication, design, and performance optimization of resoswitches. The findings here establish a strong foundation for future research, particularly in addressing fabrication challenges and

exploring new design paradigms that leverage the mechanical properties of resoswitches for enhanced performance and scalability.

The work presented lays the groundwork for future innovations in resoswitch technology, positioning it as a key component in the evolution of low-power wireless systems. With continued research and development, resoswitches have the potential to revolutionize wireless communication by offering unprecedented energy efficiency and enabling a new class of passive, sustainable devices in the expanding IoT ecosystem. Ultimately, the integration of resoswitches into future communication networks could contribute to a more energy-efficient, interconnected world, where data exchange and connectivity are seamlessly supported without compromising power efficiency.

Bibliography

- [1] J. Gubbi, R. Buyya, S. Marusic, and M. Palaniswami, "Internet of Things (IoT): A vision, architectural elements, and future directions," *Future Gener. Comput. Syst.*, vol. 29, no. 7, pp. 1645–1650, 2013.
- [2] IoT Analytics, "The number of connected IoT devices growing to 18 billion in 2024," Dec. 23, 2024. [Online]. Available: <https://iot-analytics.com/number-connected-iot-devices>.
- [3] S. S. Afzal, *Battery-Free Subsea Internet-of-Things*. M.S. thesis, Massachusetts Institute of Technology, Cambridge, MA, USA, 2022. [Online]. Available: <https://dspace.mit.edu/handle/1721.1/145054>
- [4] C. M. Costa, R. Gonçalves, and S. Lanceros-Méndez, "Recent advances and future challenges in printed batteries," *Energy Storage Mater.*, vol. 28, pp. 216-234, 2020, doi: 10.1016/j.ensm.2020.03.012.
- [5] T. C. McCarthy, S. O'Neill, and N. S. Brown, "Investigating Pathways to Minimize Sensor Power Usage for the Internet of Remote Things," *Sensors*, vol. 23, no. 21, p. 8871, 2023. [Online]. Available: <https://www.mdpi.com/1424-8220/23/21/8871>
- [6] Razavi, *RF Microelectronics*, 2nd ed. Upper Saddle River, NJ: Prentice Hall, 2012.
- [7] T. H. Lee, *The Design of CMOS Radio-Frequency Integrated Circuits*, 2nd ed. Cambridge: Cambridge University Press, 2004.
- [8] S. Haykin, *Communication Systems*, 5th ed. New York: Wiley, 2009.
- [9] B. Grebene, *Bipolar and MOS Analog Integrated Circuit Design*. New York: Wiley-Interscience, 2002.
- [10] S. K. Lahiri, H. Saha and A. Kundu, "RF MEMS SWITCH: An overview at-a-glance," *2009 4th International Conference on Computers and Devices for Communication (CODEC)*, Kolkata, India, 2009, pp. 1-5.

- [11] T.-C. Nguyen, "MEMS technology for timing and frequency control," *IEEE Trans. Ultrason., Ferroelectr., Freq. Control*, vol. 54, no. 2, pp. 251–270, 2007. [Online]. Available: <https://doi.org/10.1109/TUFFC.2007.232>.
- [12] Yang Lin, Wei-Chang Li, Zeying Ren and C. T. . -C. Nguyen, "A resonance dynamical approach to faster, more reliable micromechanical switches," *2008 IEEE International Frequency Control Symposium*, Honolulu, HI, 2008, pp. 640-645, doi: 10.1109/FREQ.2008.4623078.
- [13] R. Liu, J. Naghsh Nilchi, Y. Lin, T. L. Naing, and C. T.-C. Nguyen, "Zero quiescent power VLF mechanical communication receiver," in *Proc. 2015 Transducers - 18th Int. Conf. Solid-State Sensors, Actuators Microsystems (TRANSDUCERS)*, 2015, pp. 129-132, ISBN: 978-1-4799-8955-3, ISSN: 2164-1641.
- [14] Hyman and M. Mehregany, "Contact physics of gold microcontacts for MEMS switches," *Electrical Contacts - 1998. Proceedings of the Forty-Fourth IEEE Holm Conference on Electrical Contacts (Cat. No.98CB36238)*, Arlington, VA, USA, 1998, pp. 133-140, doi: 10.1109/HOLM.1998.722438.
- [15] Y. Lin, T. Riekkinen, Wei-Chang Li, E. Alon and C. T. . -C. Nguyen, "A metal micromechanical resonant switch for on-chip power applications," *2011 International Electron Devices Meeting*, Washington, DC, 2011, pp. 20.6.1-20.6.4, doi: 10.1109/IEDM.2011.6131593.
- [16] R. Liu, *All-Mechanical Receivers*, Ph.D. dissertation, EECS Dept., University of California, Berkeley, Technical Report No. UCB/EECS-2019-151, Dec. 1, 2019. [Online]. Available: <http://www2.eecs.berkeley.edu/Pubs/TechRpts/2019/EECS-2019-151.pdf>
- [17] Q. Jin, K. Zheng, and C. T. -C. Nguyen, "Bit Rate-Adapting Resoswitch," *2022 International Electron Devices Meeting (IEDM)*, San Francisco, CA, USA, 2022, pp. 16.5.1-16.5.4, doi: 10.1109/IEDM45625.2022.10019383.
- [18] Budd and F. Dux, "Chattering and related behaviour in impact oscillators," *Philosophical Transactions of the Royal Society of London. Series A: Physical And Engineering Sciences*, vol. 347, no. 1683, pp. 365-389, May 1994.
- [19] Z. A. Ye *et al.*, "Body-Biased Multiple-Gate Micro-Electro-Mechanical Relays," in *IEEE Electron Device Letters*, vol. 42, no. 3, pp. 402-405, March 2021, doi: 10.1109/LED.2021.3050981.
- [20] S. Newman, J. L. Ebel, D. Judy and J. Maciel, "Lifetime measurements on a high reliability RF-MEMS contact switch," *Microwave and Wireless Components Letters*, vol. 18, no. 2, pp. 100-102, 2008

- [21] Y. Lin, R. Liu, W. -C. Li and C. T. . -C. Nguyen, "Polycide contact interface to suppress squegging in micromechanical resoswitches," *2014 IEEE 27th International Conference on Micro Electro Mechanical Systems (MEMS)*, San Francisco, CA, USA, 2014, pp. 1273-1276, doi: 10.1109/MEMSYS.2014.6765881.
- [22] W. C. Tang, *Electrostatic Comb Drive for Resonant Sensor and Actuator Applications*, Ph.D. dissertation, Univ. California, Berkeley, CA, USA, 1990. Order No. 9126802.
- [23] Y. Lin, *Micromechanical Resonant Switches ("Resoswitches") and Resonant Power Converters*, Ph.D. dissertation, EECS Dept., University of California, Berkeley, Technical Report No. UCB/EECS-2015-212, Dec. 1, 2015. [Online]. Available: <http://www2.eecs.berkeley.edu/Pubs/TechRpts/2015/EECS-2015-212.pdf>
- [24] Ozgurluk, M. Akgul and C. T. . -C. Nguyen, "RF Channel-Select Micromechanical Disk Filters—Part I: Design," in *IEEE Transactions on Ultrasonics, Ferroelectrics, and Frequency Control*, vol. 66, no. 1, pp. 192-217, Jan. 2019, doi: 10.1109/TUFFC.2018.2881727.
- [25] K. H. Zheng, Q. Jin and C. T. . -C. Nguyen, "Ferrite-Rod Antenna Driven Wireless Resoswitch Receiver," *2023 IEEE 36th International Conference on Micro Electro Mechanical Systems (MEMS)*, Munich, Germany, 2023, pp. 173-176, doi: 10.1109/MEMS49605.2023.10052463.
- [26] Ozgurluk, K. Peleaux and C. T. . -C. Nguyen, "Single-Digit-Nanometer Capacitive-Gap Transduced Micromechanical Disk Resonators," *2020 IEEE 33rd International Conference on Micro Electro Mechanical Systems (MEMS)*, Vancouver, BC, Canada, 2020, pp. 222-225, doi: 10.1109/MEMS46641.2020.9056204.
- [27] S. Majumder, N. McGruer, G. Adams, P. Zavracky, R. Morrison and J. Krim, "Study of contacts in an electrostatically actuated microswitch," *Sensors and Actuators A: Physical*, vol. 93, no. 1, pp. 19-26, 2001.
- [28] Barrow, *Frequency Tunable MEMS-Based Timing Oscillators and Narrowband Filters*, Ph.D. dissertation, EECS Dept., University of California, Berkeley, Technical Report No. UCB/EECS-2015-255, Dec. 18, 2015. [Online]. Available: <http://www2.eecs.berkeley.edu/Pubs/TechRpts/2015/EECS-2015-255.pdf>
- [29] M. Lombardi and G. Nelson, "WWVB: A half century of delivering accurate frequency and time by radio," *J. Res. Natl. Inst. Stand. Technol.*, vol. 119, pp. 25-54, 2014, doi: 10.6028/jres.119.004.
- [30] Ozgurluk, R. Liu and C. T. . -C. Nguyen, "Q-boosting of metal MEMS resonators via localized anneal-induced tensile stress," *2017 Joint Conference of the European*

- Frequency and Time Forum and IEEE International Frequency Control Symposium (EFTF/IFCS)*, Besancon, France, 2017, pp. 10-15, doi: 10.1109/FCS.2017.8088786.
- [31] P. M. Zavracky, S. Majumder and N. McGruer, "Micromechanical switches fabricated using Nickel surface micromachining," *JOURNAL OF MICROELECTROMECHANICAL SYSTEMS*, pp. 3-9, 1997.
- [32] W. C. Tang, T.-C. H. Nguyen, and R. T. Howe, "Laterally driven polysilicon resonant microstructures," *Sens. Actuators*, vol. 20, no. 1-2, pp. 25-32, 1989, doi: 10.1016/0250-6874(89)87098-2.
- [33] P. Lathi, *Modern Digital and Analog Communication Systems*, 4th ed. New York, NY, USA: Oxford University Press, 2009.
- [34] A.-C. Wong and C.-C. Nguyen, "Micromechanical mixer-filters ("mixlers")," *J. Microelectromech. Syst.*, vol. 13, no. Feb., pp. 100-112, 2004.
- [35] -P. Tsai, Y. -Y. Liao and W. -C. Li, "A 125-KHZ CMOS-MEMS Resoswitch Embedded Zero Quiescent Power OOK/FSK Receiver," *2020 IEEE 33rd International Conference on Micro Electro Mechanical Systems (MEMS)*, Vancouver, BC, Canada, 2020, pp. 106-109, doi: 10.1109/MEMS46641.2020.9056120.
- [36] T.-C. Nguyen, R. Liu, and J. N. Nilchi, "[An ultra-low power mechanical trigger detector \(invited\)](#)," *Proceedings*, 2017 Gov. Microcircuit Applications & Critical Technology Conf., Reno, Nevada, March 20-23, 2017, pp. 104-107.
- [37] W. H. Silver, *The ARRL Antenna Book For Radio Communications*, 22nd ed. Newington, CT, USA: ARRL, 2011.
- [38] G. Barrow, T. L. Naing, R. A. Schneider, T. Rocheleau, V. Yeh, Z. Ren, and C. T.-C. Nguyen, "A real-time 32.768-kHz clock oscillator using a 0.0154-mm² micromechanical resonator frequency-setting element," in *Proc. 2012 IEEE Int. Freq. Control Symp.*, 2012, pp. 1-6.
- [39] Y. Lin, W. -C. Li, Z. Ren, and C. T.-C. Nguyen, "The micromechanical resonant switch ("Resoswitch")," in Hilton Head, 2008, pp. 40-43.
- [40] R. Liu, J. N. Nilchi and C. T. . -C. Nguyen, "RF-powered micromechanical clock generator," *2016 IEEE International Frequency Control Symposium (IFCS)*, New Orleans, LA, USA, 2016, pp. 1-6, doi: 10.1109/FCS.2016.7546785.
- [41] R. Liu, J. N. Nilchi and C. T. . -C. Nguyen, "CW-powered squegging micromechanical clock generator," *2017 IEEE 30th International Conference on Micro Electro*

- Mechanical Systems (MEMS)*, Las Vegas, NV, USA, 2017, pp. 905-908, doi: 10.1109/MEMSYS.2017.7863555.
- [42] R. L. Jackson, I. Green, and D. B. Marghitu, "Predicting the coefficient of restitution of impacting elastic-perfectly plastic spheres," *Nonlinear Dyn.*, vol. 60, pp. 217-229, 2010, doi: 10.1007/s11071-009-9591-z.
- [43] Ho, Z.-Q. Lang, and S. A. Billings, "A frequency domain analysis of the effects of nonlinear damping on the Duffing equation," *Mech. Syst. Signal Process.*, vol. 45, no. 1, pp. 49–67, 2014, doi: [10.1016/j.ymssp.2013.10.027](https://doi.org/10.1016/j.ymssp.2013.10.027).
- [44] Y. Lin *et al.*, "Digitally-specified micromechanical displacement amplifiers," *TRANSDUCERS 2009 - 2009 International Solid-State Sensors, Actuators and Microsystems Conference*, Denver, CO, USA, 2009, pp. 781-784, doi: 10.1109/SENSOR.2009.5285651.
- [45] S. Timoshenko and J. N. Goodier, *Theory of Elasticity*, 3rd ed. New York, NY, USA: McGraw-Hill, 1970.
- [46] R. A. Johnson, *Mechanical filters in electronics*, New York: John Wiley & Sons, 1983.
- [47] P. Pattanaik and M. Ojha, "Review on challenges in MEMS technology," *Mater. Today: Proc.*, vol. 81, pt. 2, pp. 224-226, 2023, doi: 10.1016/j.matpr.2021.03.142.

Appendix A: Gold-Electroplated Resoswitch Process Traveler

0. Tools needed in the Nanolab

<i>Deposition</i>	<i>Lithography</i>	<i>Metrology</i>	<i>Release</i>	<i>Cleaning</i>	<i>Misc.</i>
tystar11	picotrack1	alphastep	cpd	msink6	hot plate
tystar3	picotrack2	nanospec	primaxx	msink8	
ebeam1	asml300			msink16	
				msink18	
				msink3	

1. Starting wafers

Doping: p-type

Wafer Class: prime

Wafer Size: 6"

Scribing: On the front, near right side of the major flat.

Cross Section:



Sub.

2. Cleaning: Pre-furnace cleaning

Nanolab Tool: msink8, msink6

Chemical: Piranha

Temperature: 120°C

Time: 00:10:00

3. Test Deposition: Sacrificial oxide (LTO)

Nanolab Tool: tystar11

Options: tystar12, tystar16

Recipe: 11SULTON

Gas Flows: O₂= 135sccm, SiH₄=90sccm

Pressure: 400mTorr

Temperature: 450°C

Deposition Rate: 10.71nm/min

Time: 04:20:00

Process Note: Tystar16 requires a longer stabilization period before initiating deposition compared to Tystar11 or Tystar12. The stabilization time for Tystar16 is approximately 3 hours.

4. Test Metrology: Sacrificial oxide thickness measurement

Nanolab Tool: nanospec

Options: nanoduv

Program: Thin Oxide on Silicon (10x)

Thickness: Center: ___ Top: ___ Bottom: ___ Left: ___ Right: ___ Average: ___

5. Deposition: Sacrificial oxide

Nanolab Tool: tystar11

Options: tystar12, tystar16

Recipe: 11SULTON

Gas Flows: O₂= 135sccm, SiH₄=90sccm

Pressure: 400mTorr

Temperature: 450°C

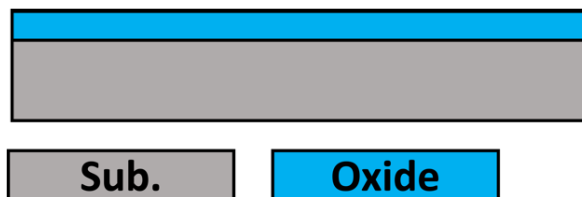
Deposition Rate: 10.71nm/min (adjust if needed)

Time: 04:40:00 (adjust if needed)

Goal: 3μm

Process Note: Tystar16 requires a longer stabilization period before initiating deposition compared to Tystar11 or Tystar12. The stabilization time for Tystar16 is approximately 3 hours.

Cross Section:



6. Annealing: Sacrificial oxide densification

Nanolab Tool: tystar2

Options: tystar3

Recipe: 2HIN2ANA

Temperature: 1000°C

Time: 01:00:00

Process Note: Unannealed low-temperature oxide (LTO) exhibits a faster and less predictable etch rate. Therefore, annealing the oxide immediately after deposition is essential to ensure process stability.

7. Pre-deposition Bake: Seed layer deposition

Nanolab Tool: Hot plate

Temperature: 200°C

Time: 00:10:00

Process Note: A brief bake of the wafers prior to seed layer deposition enhances the adhesion between the sacrificial oxide and the seed layers.

8. Seed Layer Deposition: Chromium adhesion layer

Nanolab Tool: ebeam1

Options: ast-ebeam

Emission Current: 20mA

Thickness: 8nm

Process Note: Perform the deposition of the Au seed layer immediately after the Cr adhesion layer, using the same tool without venting the chamber or unloading the wafers.

9. Seed Layer Deposition: Gold seed layer

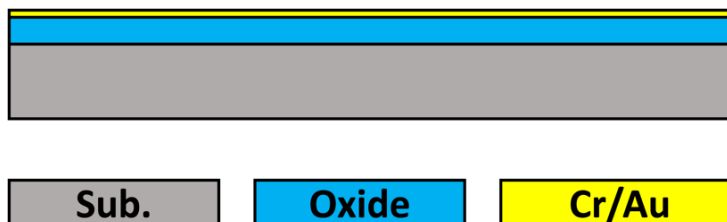
Nanolab Tool: ebeam1

Options: ast-ebeam

Emission Current: 60mA

Thickness: 25nm

Cross Section:

**10. Pre-lithography Cleaning: Metal surface cleaning**

Nanolab Tool: ultrasonicator in msink3

1st Chemical: Acetone

2nd Chemical: IPA

Time: 5mins

Time: 5mins

Process Note: Blow dry using Nitrogen gun.

11. Pre-Lithography Coating: HMDS layer

Nanolab Tool: primeoven

Program: program0

Time: 31.5mins with 1min HMDS coating

Process Note: primeoven coating with HMDS will improve the adhesion between the photoresist and metal seed layers.

12. Photoresist Coating: BARC layer

Nanolab Tool: svgcoat3

Resist Type: BARC

Recipe: BARC, program #3

Spin Speed: 3750rpm

Bake Temperature: 190°C

Bake Time: 60s

Thickness: 60nm

Process Note: A Bottom Anti-Reflective Coating (BARC) layer is used beneath the photoresist to minimize reflections from the substrate during lithography. This reduces standing wave effects and enhances the uniformity and resolution of the photoresist pattern, which is critical for achieving accurate feature dimensions in the electroplating mold.

13. Photoresist Coating: PR mold

Nanolab Tool: picotrack1

Options: svgcoat6

Resist Type: UV26

Recipe: UV26_3.0-2.5um_NoHMDS

Thickness: 2.5um

Process Note: Always run at least one dummy wafer first and visually check the resist uniformity.

14. Photoresist Exposure: PR mold

Nanolab Tool: asml300

Options: None

ASML Job: Silicideswitch

Reticle: SILICIDESWITCH

Field: PR MOLD

Exposure: 38mJ

Focus: 0nm

15. Photoresist Development: PR mold

Nanolab Tool: picotrack2

Options: svgcoat6

Developer: MF26A

Recipe: T2_PROX110C60s_MF26A45s

Dev. Count: Once

Process Note: Develop the wafers immediately after exposure.

16. Photoresist UV-bake: PR mold

Nanolab Tool: Hotplate

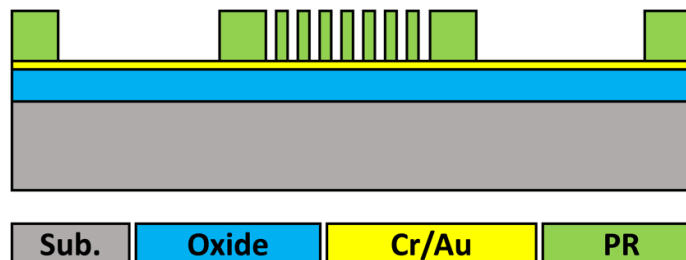
Options: None

Temperature: 120°C

Time: 01:00:00

Process Note: Avoid using axcelis for the photoresist (PR) hard bake, as temperatures exceeding 120°C can cause deformation or shrinkage of the PR mold. Instead, opt for a moderate baking temperature with an extended baking duration to ensure stability and preserve the mold's integrity.

Cross Section:



17. Pre-electroplating Processing: Open BARC contact

Nanolab Tool: technics-c

Options: ptherm, semi

Power: 70W

Time: 00:02:00

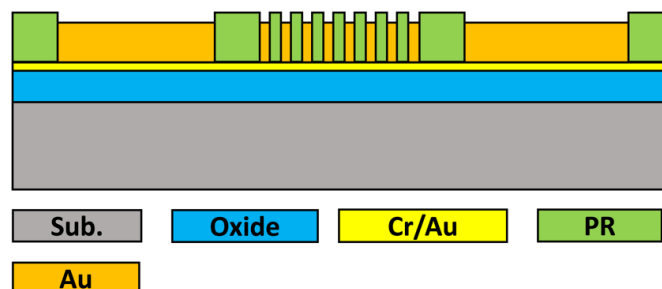
Gas Flow: O₂ 180-190sccm

Process Note: This step is necessary to remove the BARC layer from the areas designated for electroplating. Since the PR development process alone does not eliminate the BARC layer, an O₂ plasma etch is required to expose the gold seed layer, enabling subsequent electroplating.

18. Gold Electroplating: Gold resowitch layer

Electroplating process is carried out in the wet lab according to the steps outlined in section 2.3.2.

Cross Section:



19. Cleaning: PR mold strip

Nanolab Tool: technics-c

Options: ptherm, semi

Power: 300W

Time: 00:10:00

Gas: O₂ 180-190sccm

20. Release: Clean baskets, dishes, tweezers, and glass beakers

Nanolab Tool: msink16 & msink18

Options: None

Chemical: Piranha (Sulfuric Acid: Hydrogen Peroxide = 1:1)

Temperature: Set by the activated chemical

Time: 00:10:00

Process Note: Rinse all equipment with water before and after the piranha clean.

21. Release: Seed layer removal

Nanolab Tool: msink16 & msink18

Options: None

1st Chemical: Au etchant

2nd Chemical: HCl

Temperature: room temperature

Temperature: room temperature

Time: 00:00:15

Time: 00:00:30

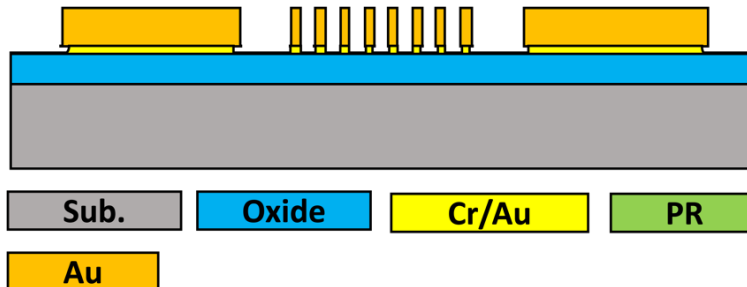
3rd Chemical: Cr-7 etchant

Temperature: room temperature

Time: 00:00:15

Process Note: HCl is employed to remove any Cr oxide that may form during the metal layer deposition process, ensuring a clean surface for subsequent steps.

Cross Section:



22. Release: Sacrificial oxide removal

Nanolab Tool: Primaxx

Options: None

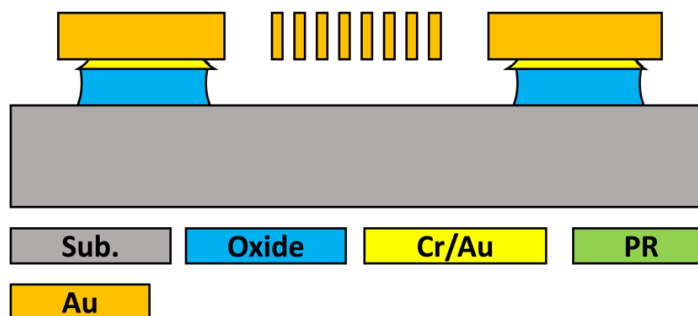
Recipe: recipe 3

Temperature: 45°C

Time: 12 mins/cycle, 3 cycles

Process Note: Before releasing the samples using Primaxx, bake them on a hotplate at 200°C for 2 minutes to remove any off-gassed polymer residue that may have accumulated during storage.

Cross Section:



23. Probe Station Testing

Tool: Lakeshore

Options: MMR, Wirebonding

Temperature: Room temperature

Vacuum: <10 mTorr

Process Note: Make sure the Lakeshore probes are not bent and functional. Also, check the measurement setup, i.e., bias tees, cables etc., with a known working device in advance.

Appendix B: Ruthenium-Electroplated Resoswitch Process Traveler

0. Tools needed in the Nanolab

<i>Deposition</i>	<i>Etcher</i>	<i>Lithography</i>	<i>Metrology</i>	<i>Release</i>	<i>Cleaning</i>	<i>Misc.</i>
tystar11	ptherm	picotrack1	alphastep	cpd	msink6	hot plate
tystar3		picotrack2	nanospec	primaxx	msink8	
ebeam1		asm1300			msink16	
oxford2					msink18	
					msink3	

1. Starting wafers

Doping: p-type

Wafer Class: prime

Wafer Size: 6"

Scribing: On the front, near right side of the major flat.

Cross Section:



Sub.

2. Cleaning: Pre-furnace cleaning

Nanolab Tool: msink8, msink6

Chemical: Piranha

Temperature: 120°C

Time: 00:10:00

3. Test Deposition: Sacrificial oxide (LTO)

Nanolab Tool: tystar11

Options: tystar12, tystar16

Recipe: 11SULTON

Gas Flows: O₂= 135sccm, SiH₄=90sccm

Pressure: 400mTorr

Temperature: 450°C

Deposition Rate: 10.71nm/min

Time: 04:20:00

Process Note: Tystar16 requires a longer stabilization period before initiating deposition compared to Tystar11 or Tystar12. The stabilization time for Tystar16 is approximately 3 hours.

4. Test Metrology: Sacrificial oxide thickness measurement

Nanolab Tool: nanospec

Options: nanoduv

Program: Thin Oxide on Silicon (10x)

Thickness: Center: ___ Top: ___ Bottom: ___ Left: ___ Right: ___ Average: ___

5. Deposition: Sacrificial oxide

Nanolab Tool: tystar11

Options: tystar12, tystar16

Recipe: 11SULTON

Gas Flows: O₂= 135sccm, SiH₄=90sccm

Pressure: 400mTorr

Temperature: 450°C

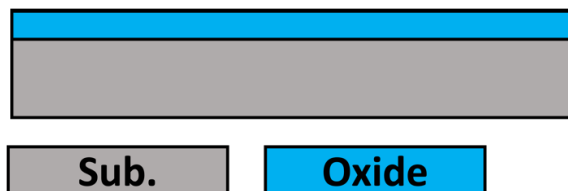
Deposition Rate: 10.71nm/min (adjust if needed)

Time: 04:40:00 (adjust if needed)

Goal: 3µm

Process Note: Tystar16 requires a longer stabilization period before initiating deposition compared to Tystar11 or Tystar12. The stabilization time for Tystar16 is approximately 3 hours.

Cross Section:



6. Annealing: Sacrificial oxide densification

Nanolab Tool: tystar2

Options: tystar3

Recipe: 2HIN2ANA

Temperature: 1000°C

Time: 01:00:00

Process Note: Unannealed low-temperature oxide (LTO) exhibits a faster and less predictable etch rate. Therefore, annealing the oxide immediately after deposition is essential to ensure process stability.

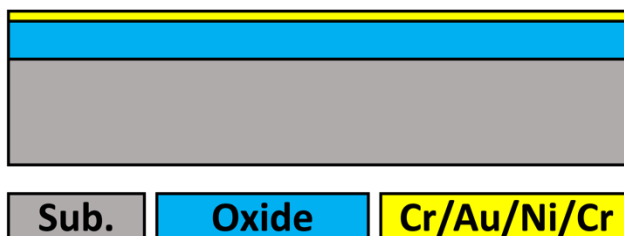
7. Pre-deposition Bake: Seed layer deposition

Nanolab Tool: Hot plate

Temperature: 200°C

Time: 00:10:00

Process Note: A brief bake of the wafers prior to seed layer deposition enhances the adhesion between the sacrificial oxide and the seed layers.

8. Seed Layer Deposition: Chromium adhesion layer*Nanolab Tool:* ebeam1*Options:* ast-ebeam*Emission Current:* 20mA*Thickness:* 7nm*Process Note:* Perform the deposition of subsequential seed layers immediately after the Cr adhesion layer, using the same tool without venting the chamber or unloading the wafers.**9. Seed Layer Deposition: Gold seed layer***Nanolab Tool:* ebeam1*Options:* ast-ebeam*Emission Current:* 75mA*Thickness:* 14nm**10. Seed Layer Deposition: Ni protective layer***Nanolab Tool:* ebeam1*Options:* ast-ebeam*Emission Current:* 45mA*Thickness:* 7nm**11. Seed Layer Deposition: Chromium adhesion layer***Nanolab Tool:* ebeam1*Options:* ast-ebeam*Emission Current:* 20mA*Thickness:* 5.5nm*Process Note:* The adhesion between Ni and silicon dioxide (which will serve as the mold for electroplating) is weak. Therefore, an additional Cr layer is required to enhance the adhesion between these materials.*Cross Section:***12. Test Deposition: Oxide mold***Nanolab Tool:* oxford2*Options:* oxfordpecvd4*Temperature:* 300°C*Recipe:* qjsio2*Deposition Rate:* 73.84 nm/min

Time: 00:08:00

Thickness: Center: ___ Top: ___ Bottom: ___ Left: ___ Right: ___ Average: ___

13. Deposition: Oxide mold

Nanolab Tool: oxford2

Options: oxfordpecvd4

Temperature: 300°C

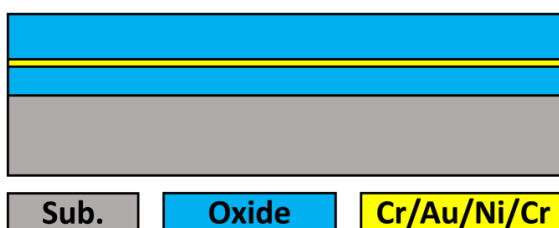
Recipe: qjsio2

Deposition Rate: 73.84 nm/min

Time: 00:08:00 (adjust if needed)

Thickness: 590 nm

Cross Section:



14. Photoresist Coating: BARC layer

Nanolab Tool: svgcoat3

Resist Type: BARC

Recipe: BARC, program #3

Spin Speed: 3750rpm

Bake Temperature: 190°C

Bake Time: 60s

Thickness: 60nm

Process Note: A Bottom Anti-Reflective Coating (BARC) layer is used beneath the photoresist to minimize reflections from the substrate during lithography. This reduces standing wave effects and enhances the uniformity and resolution of the photoresist pattern, which is critical for achieving accurate feature dimensions in the electroplating mold.

15. Photoresist Coating:

Nanolab Tool: picotrack1

Options: svgcoat6

Resist Type: UV210

Recipe: UV210_0.3-0.43um_NoHMDS

Thickness: 0.43um

Process Note: Always run at least one dummy wafer first and visually check the resist uniformity.

16. Photoresist Exposure:

Nanolab Tool: asml300
Options: None
ASML Job: Silicideswitch
Reticle: SILICIDESWITCH
Field: PR MOLD
Exposure: 20mJ
Focus: 0nm

17. Photoresist Development:

Nanolab Tool: picotrack2
Options: svgcoat6
Developer: MF26A
Recipe: T2_PEB130C90s_MF26A45s
Dev. Count: Once
Process Note: Develop the wafers immediately after exposure.

18. Photoresist UV-bake:

Nanolab Tool: axcelis
Options: None
Program: U

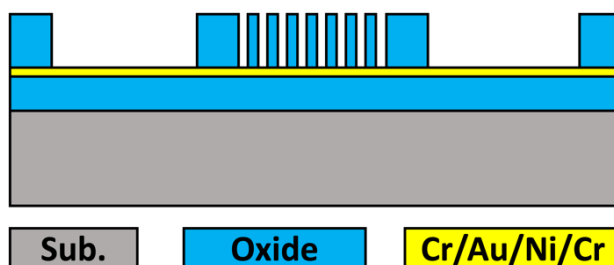
19. Test Etch: Oxide mold

Nanolab Tool: ptherm
Options: None
Power: 250W
Gas Flows: O₂ 4sccm; CHF₃ 60sccm
Etch Rate: 40.01 nm/min
Time: 00:06:00
Thickness:
 Before etch: Center: ___ Top: ___ Bottom: ___ Left: ___ Right: ___
 After etch: Center: ___ Top: ___ Bottom: ___ Left: ___ Right: ___

20. Etch: Oxide mold

Nanolab Tool: ptherm
Options: None
Power: 250W
Gas Flows: O₂ 4sccm; CHF₃ 60sccm
Etch Rate: 40.01 nm/min
Time: 00:16:00 (adjust if needed)

Cross Section:



21. Pre-electroplating Processing: Open contact area

Nanolab Tool: msink16 & msink18

Options: None

1st Chemical: HCl

2nd Chemical: Cr-7 etchant

Temperature: room temperature

Temperature: room temperature

Time: 00:00:30

Time: 00:00:03

3rd Chemical: Ni etchant

Temperature: room temperature

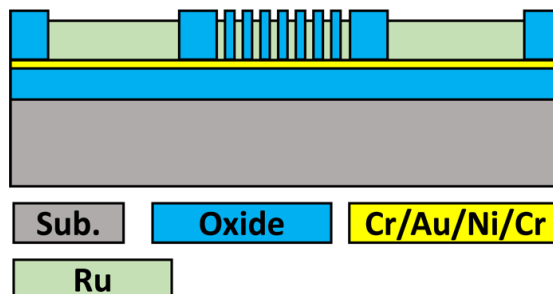
Time: 00:02:00

Process Note: HCl is employed to remove any Cr oxide that may form during the metal layer deposition process, ensuring a clean surface for subsequent steps.

22. Ru Electroplating: Ru resoswitch layer

Electroplating process is carried out in the wet lab according to the steps outlined in section 2.4.1.

Cross Section:



23. Release: Clean baskets, dishes, tweezers, and glass beakers

Nanolab Tool: msink16/msink18

Options: None

Chemical: Piranha (Sulfuric Acid: Hydrogen Peroxide = 1:1)

Temperature: Set by the activated chemical

Time: 00:10:00

Process Note: Rinse all equipment with water before and after the piranha clean.

24. Release: Oxide mold strip

Nanolab Tool: msink16/msink18

Options: None

Chemical: 5:1 HF

Time: 00:02:00

Temperature: room temperature

25. Release: Seed layer removal

Nanolab Tool: msink16/ msink18

Options: None

1st Chemical: HCl

Temperature: room temperature

Time: 00:00:30

3rd Chemical: Ni etchant

Temperature: room temperature

Time: 00:02:00

5th Chemical: HCl

Temperature: room temperature

Time: 00:00:30

2nd Chemical: Cr-7 etchant

Temperature: room temperature

Time: 00:00:03

4th Chemical: Au etchant

Temperature: room temperature

Time: 00:00:10

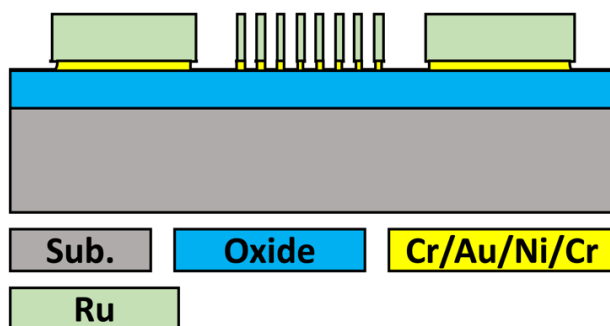
6th Chemical: Cr-7 etchant

Temperature: room temperature

Time: 00:00:05

Process Note: HCl is employed to remove any Cr oxide that may form during the metal layer deposition process, ensuring a clean surface for subsequent steps.

Cross Section:



26. Release: Sacrificial oxide removal

Nanolab Tool: Primaxx

Options: None

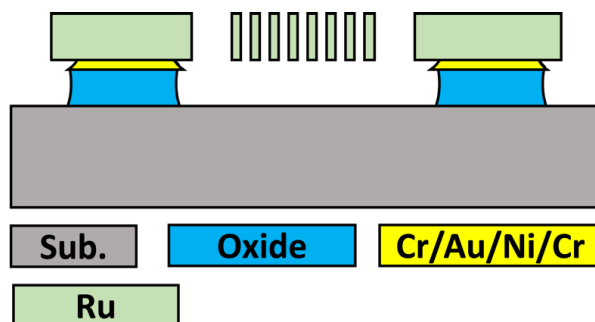
Recipe: recipe 3

Temperature: 45°C

Time: 11 mins/cycle, 3 cycles

Process Note: Before releasing the samples using Primaxx, bake them on a hotplate at 200°C for 2 minutes to remove any off-gassed polymer residue that may have accumulated during storage.

Cross Section:



27. Probe Station Testing

Tool: Lakeshore

Options: MMR, Wirebonding

Temperature: Room temperature

Vacuum: <10 mTorr

Process Note: Make sure the Lakeshore probes are not bent and functional. Also, check the measurement setup, i.e., bias tees, cables etc., with a known working device in advance.